OPTICAL ANTENNAS

ON SUBSTRATES AND WAVEGUIDES

Felipe Bernal Arango

Optical Antennas on Substrates and Waveguides
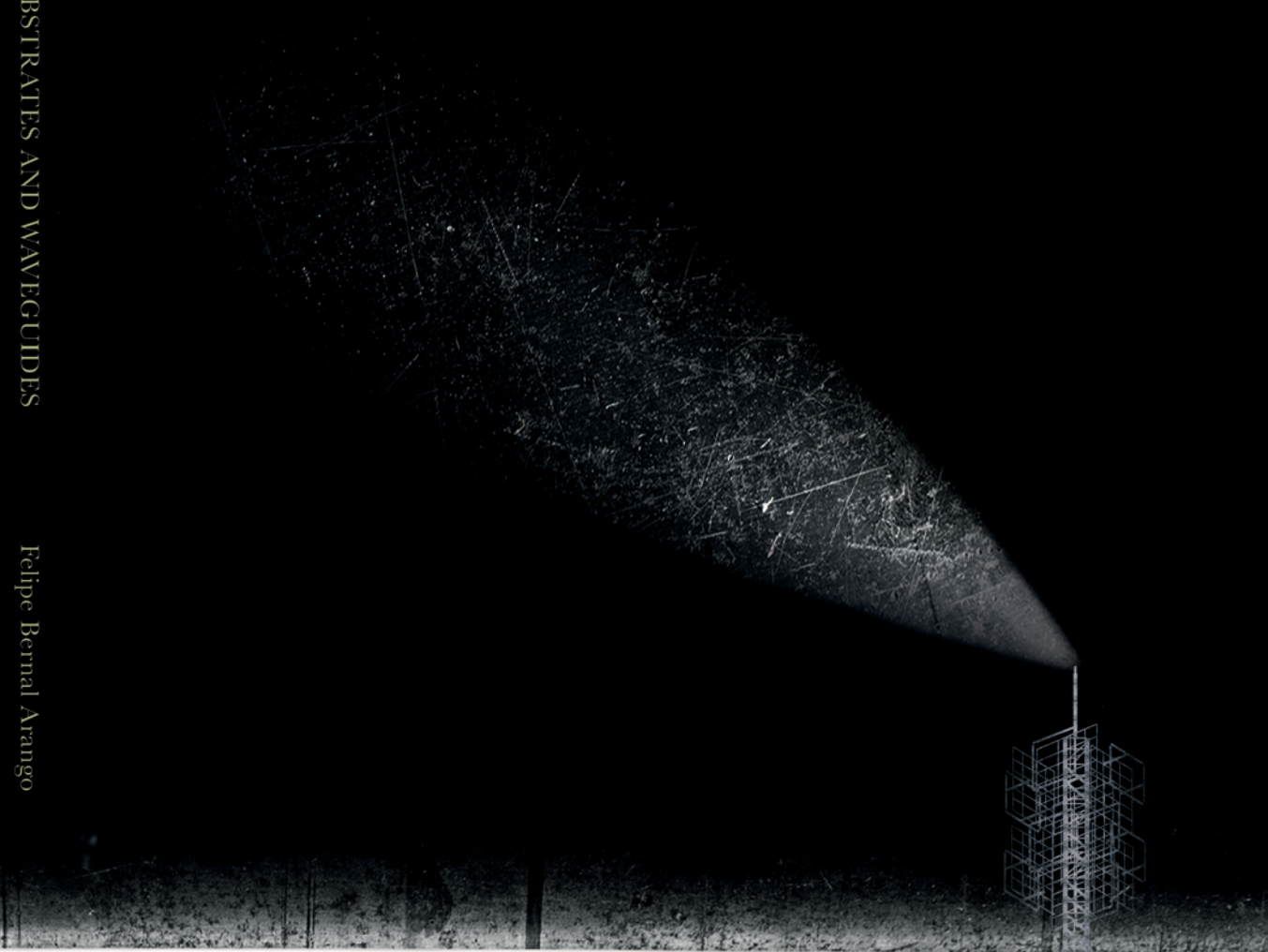
Optical Antennas on Substrates and Waveguides

ACADEMISCH PROEFSCHRIFT

ter verkrijging van de graad van doctor
aan de Universiteit van Amsterdam
op gezag van de Rector Magnificus
prof. dr. D. C. van den Boom
ten overstaan van een door het college voor promoties
ingestelde commissie,
in het openbaar te verdedigen in de Aula der Universiteit
op vrijdag 19 september 2014, te 11:00 uur

door

Felipe Bernal Arango

geboren te Bogotá in Colombia

Promotor: prof. dr. A. F. Koenderink

Overige leden: prof. dr. T. Gregorkiewicz
               prof. dr. N. van Hulst
               dr. D. van Oosten
               prof. dr. A. Polman
               prof. dr. H. Salemink
               prof. dr. F. Schreck

Faculteit der Natuurwetenschappen, Wiskunde en Informatica

Contents

1

Introduction

1.1 Light and nano antennas

Human experience and perception is largely determined by the visual observation of our external universe. This perception has been argued to be a projection of the complex external reality, projection which is itself interpreted and complemented in our mind to fit in, or extend, our own mental model of the universe [1, 2]*. In all cases these visual observations are unequivocally mediated by the transmissions and reflections of light by the objects and persons in our surroundings, which makes light one of the most important mediators for the acquisition of information in our life. The projections and reflections caused by sun light has shaped our understanding of the world, and since the invention of artificial light sources and light detectors, these optical means for gathering information have allowed us to see the intricate relations between the smallest of things with microscopes [3, 4], and with photomultiplier tubes and scintillators in high energy experiments [5–7] as well as the biggest of the objects [8, 9] in the universe with telescopes.

The evident vast importance that light has had in human history becomes even more apparent when we realize that two of the most important challenges that humanity is facing nowadays also have to do in one or another way with light. First, we are currently living in a moment of human history where the effects of global warming are starting to touch everyone's experience and perception, since according to international panels of climate scientist [10] humankind's consumption of energy, and in particular fossil

---

*This idea of perception and mental models has a long standing history. In western culture we can see a clear early example of such reasoning in the text The Republic with the "The allegory of the cave" by Plato (347bc)

fuels, has given rise firstly to a systematic global warming and secondly to depletion of available resources. Through general societal debate about IPCC findings [10], the EU system of CO_2 taxation [11], or the increasing shift of subsidy and research funding to renewable energy sources as consigned in the Europe 2020 plan [12], this challenge is starting to be felt throughout western society. Projections, such as those of the IPCC argue that the entire earth eco-system with human life as a marginal contributor has enjoyed a delicate balance of energy with the continuous input of energy from the sun as well as the earth-internal radiogenic sources [13] over the last millennia. This balance is currently shifting owing to the vast rise by ~365% in human population [14] and per capita energy consumption in the last century. Rather than acquiring the required energy from the finite supply of fossil fuels, which accounted for ~85% of annual energy in the last decade [13, 15], an indefinitely sustainable energy balance would require that energy is harvested directly from the sun, in all different forms in which it can be found in nature, *e.g.* in form of wind energy, in form of harvesting energy stored in the earth's hydrosphere, and through photochemical or photovoltaic conversion of light into chemical reactions or electricity.

As a second challenge, we are living in an information revolution where people all over the globe are connected, can process vast amounts of information and can transmit this information in a matter of seconds from one side of the planet to the other. This revolution has been possible thanks to the conception and development of faster and more efficient computers as well as networks of optical fibers, mobile phone antennas and satellites. Nevertheless electronic chip technology is arriving to a bandwidth and power consumption bottleneck. The recent improvements in bandwidth in electronic interconnects have only been possible at the price of increasing dramatically the circuit power consumption [16]. It is expected that by 2015 interconnections of the billions of transistors in a modern processor just cannot be miniaturized any further, as stated by the International Technology Roadmap for Semiconductors (ITRS) [17]. Even forgetting for a moment the issues that photolithography has to solve below 14 nm feature sizes [17], it is a fact that shrinking the copper wires further will be accompanied by an increase in resistance, power consumption and even breakdown of the functionalities of the circuits themselves due to electro migration and material limits which will impose strong limits to this miniaturization [17].

For both challenges possible solutions are sought in the efficient manipulation and control of light. The energy problem *could* be solved by increasing the absorption of photons by thin and cheap solar cells [18]. On the other hand the transmission and manipulation of information in our computers could be solved by using chips with dielectric waveguides [19] and optical devices, which transmit the information in and in between chips, as well as optically manipulate, switch, direct and control the information carried by the light in waveguide modes.

Both for harvesting photons in a solar cell, and for manipulating the emission, detection and propagation of light on a photonic chip, a major fundamental challenge is that the interaction of light with matter is weak. For instance the strong interaction of electrons and matter ensures that for an electron with an energy of 1 eV the average attenuation length through which this electron can travel in air before getting absorbed

by a molecule is about 6 μm[†] while for a photon in the visible range this attenuation length is 30 to 190 km for violet (410 nm) and red (650 nm) photons respectively [21]. Nevertheless, since around 10 years ago the currently big field of nano-photonics and plasmonics has shown a possible path to overcome this weak interaction by using optical nano-antennas [22].

Optical nano-antennas are antennas for light. These antennas work in the optical to infrared frequency spectrum and their sizes are on the order of hundreds of nanometers [23–25]. They are capable of converting localized energy into propagating radiation in free space [23, 25] as well as in waveguides as will be seen later in this thesis. Also, these antennas can do the opposite which is converting incident radiation into sub-diffraction-limit localized foci of high energy density [23]. Fig. 1.1 shows a sketch of the operation of these sort of antennas. The materials used for optical
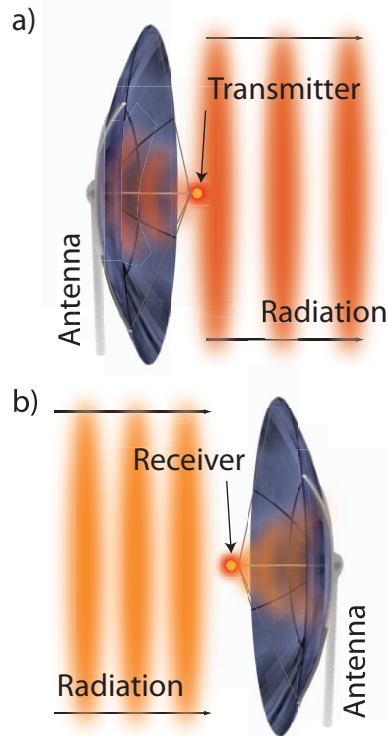
Figure 1.1: Examples of the modes of operation of nano antennas. Image modified from Lukas Novotny and Niek van Hulst, Nature Photonics 5, 83−90 (2011) doi:10.1038 nphoton.2010.237, see Reference [23].

[†]This distance is an approximation found by using the electron range function in (g cm^{-2}) $log(Rp) = -5.1 + 1.358x + 0.215x^2 - 0.043x^3$ where $x = log(E(keV))$ and using a density for air ρ =0.00129 g cm^{-3} (see Ref. [20])

antennas are varied. Part of the field of optical antennas specializes in using dielectric antennas. With these dielectric materials light matter interaction can be enhanced by increasing the residence time of photons in resonant structures. Another part of the field uses metallic antennas, in a subfield called plasmonics, for which light matter interaction is increased by confining strong electromagnetic fields to volumes smaller than the diffraction limit. The light matter interaction enhancements achieved for dielectric as well as for plasmonic nanoantennas can be explained starting from the properties of the dielectric function (ϵ) for these two class of materials.

Dielectric materials present a positive permittivity [21] ($\mathrm{Re}\{\epsilon\} > 0$, usually in fact $\epsilon > 1$) and a $\mathrm{Im}\{\epsilon\} \approx 0$. In case of a homogeneous ϵ, the solutions to Maxwell's equations are plane waves (e.g. $\mathbf{E}(\mathbf{r}) = \mathbf{E}_0 e^{i\mathbf{k}\cdot\mathbf{r}}$) of wave number $k = |\mathbf{k}| = k_0\sqrt{\epsilon\mu}$, where $k_0 = 2\pi/\lambda$ is the free space wave number and λ is the wavelength in free space. From the expression for the field of a plane wave and the expression for k, it is immediately evident that $\mathrm{Im}\{\epsilon\}$ introduces an exponential decay, which is associated with material absorption [21, 25]. Due to the small values of $\mathrm{Im}\{\epsilon\}$ for dielectric materials the dissipative losses are fairly small. Because of the small losses of dielectrics they have been used to fabricate wavelength-sized objects with strong resonances, as well as ensembles of scatterers like powders and sponges that multiply scatter light [26]. A single scatterer can strongly scatter light when it supports a geometric resonance, for instance when a wave fits an integer number of times across the perimeter, or in the bulk of the particle. Archetypical examples are dielectric spheres, array of spheres and cylinders, nanowires and ring resonators [27–31]. [‡]

For the case of nano antennas made of noble metals, like gold or silver, when electric fields of light drive these plasmonic antennas, the charges in the metal are accelerated in such a way that the movement of charges will create an induced field which prevents the driving field to penetrate the metal. Indeed, evaluating the wave number for a purely real, but negative, ϵ, shows an exponential decay length $\delta = 1/(2k_0\sqrt{\epsilon})$ [§]. This decay does not point at absorption, but points at the fact that in metals, electrons tend to rearrange to screen any incident field from penetrating further than the skin depth into the material. This effect can be included in the dielectric function of the metal. The simplest model of a metal dielectric function which only takes into account the movement of free charges is the Drude-Sommerfeld model [21], which supposes the following equation of motion for any free charge in the metal:

$$m_e\frac{\partial^2 \mathbf{r}}{\partial t^2} + m_e\Gamma\frac{\partial \mathbf{r}}{\partial t} = -e\mathbf{E}_0 e^{i\omega t}. \tag{1.1}$$

where e is the charge of the electron, m_e is the mass of the electron, $\mathbf{r}$ is the position of the electron, t is time, Γ is the damping rate for the movement of the electrons

---

[‡]Somewhat arbitrarily the field has used exclusively the term Mie resonances only for the resonances supported by dielectric scatterers like the ones just discussed, even though resonances found in Mie solutions are solutions of the electromagnetic equations for sphere and cylindrical scatterers regardless of its material, and thus any resonance in such a scatterer despite its material could be called a Mie resonance.

[§]The decay length or skin depth is easily found by using the intensity of a plane wave in the direction of propagation in the metal $\mathbf{E}\cdot\mathbf{E}^*$ when k is purely imaginary from $k = k_0\sqrt{\epsilon}$ due to the real negative ϵ

(specifically $\Gamma = v_F/\ell$, where v_F is the Fermi velocity, i.e. the fastest velocity of an electron in the metal, and ℓ is the electron mean free path) and $\mathbf{E}_0$ is the driving harmonic field with frequency ω. The effect of the movement of the driven free charges on the permittivity is included through the volume polarization density of the material $\mathbf{P} = \epsilon_0 \chi \mathbf{E} = -ne\mathbf{r}$ where n is the electron charge density of the material and χ is the susceptibility of the material [32] which can also be defined as $\chi = \epsilon - 1$. Using these equations and solving Eq. (1.1) we find that for the Drude-Somerfeld model the permittivity as a function of the driving frequency ω reads:

$$\epsilon(\omega) = 1 - \frac{\omega_p^2}{\omega^2 + i\Gamma\omega} \tag{1.2}$$

where ω_p is the plasma frequency of the metal defined as $\sqrt{ne^2/m_e\epsilon_0}$. For $\omega < \omega_p$ the real part of ϵ is negative. For common metals ω_p is in the UV. For instance, for gold the plasma frequency is equivalent to the frequency of UV light with a wavelength of λ_p =145 nm, for silver λ_p =129 nm, for platinum λ_p =241 nm and finally for aluminium λ_p =81 nm. Any wave with a wavelength longer than these plasma frequencies will encounter a medium with a negative permittivity, while light with shorter wavelengths would encounter a dielectric material.

As it was already commented, a negative real part of epsilon impedes penetration of fields inside the material, but at the same time a negative epsilon allows for electric fields with high wave numbers $k > k_0$ to be bound to interfaces between a metal (Re$\{\epsilon\} < 0$) and a dielectric (Re$\{\epsilon\} > 0$). As example, we discuss the response of a
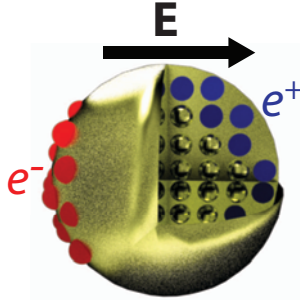
Figure 1.2: Sketch of a metallic sphere being driven by an electric field. The sphere is shown with a cut that aids viewing the reaction of the charges inside the sphere. Due to the electric field the free electrons in the metal, depicted in red, oscillate and accumulate on the edges of the particle. Neutral atoms are depicted in gold color and positive ions, shown on the right edge of the particle, are depicted in blue.

small metal sphere driven by an incident oscillatory electric field as shown in Fig. 1.2. The electron sea easily follows the electric field, as described by Eq. (1.1) to give rise to an excess negative charge on one side of the sphere, while there is net positive charge on the other side, attributable to the ionic backbone that remains stationary. This positive charge pulls back the electrons giving rise to a resonance. Indeed, this intuition

that charge separation sets up a resonant dipole moment is evident from the so called Rayleigh polarizability,

$$\alpha(\omega) = 4\pi\epsilon_0 a^3 \frac{\epsilon(\omega) - \epsilon_{\text{env}}}{\epsilon(\omega) + 2\epsilon_{\text{env}}}. \tag{1.3}$$

Where we see that in the scenario when the negative ϵ, stemming from the movement of free charges, reaches values close or equal to $-2\epsilon_{\text{env}}$ this creates a strongly polarizable object. There is one very important effect that stems from the strongly bound electromagnetic mode at the interface between a metal and a dielectric, which is that the mode can be confined to very small volumes, well below the size in free space of the wavelength used [32, 33]. Because of this strong confinement the electric field per photon can be enhanced up to about 2 orders of magnitude as shown in Ref. [34]. This strong interaction of electromagnetic fields with matter thanks to plasmonic nanoantennas has been used to study surface infrared absorption enhancement SEIRA [35–39], Raman enhanced spectroscopy [38, 40–42], fluorescence enhancement [43, 44], fluorescence correlation spectroscopy [45–47], enhanced transduction in optomechanical systems [48], enhanced solar cell efficiencies [49, 50], enhanced decay rates of single quantum emitters [51], enhanced non linear frequency generation [52]. Finally many different sensing strategies have been proposed for plasmonic antennas, using the strong refractive index sensitivity due to the enhanced light matter interaction in plasmonics [53, 54].

1.2   Nano antennas as multipolar scatterers

Although the difference in ϵ between metallic and dielectric materials creates interesting almost mutually exclusive phenomena, like strong field confinement for metallic antennas [34] or lossless creation of magnetic scatterers for dielectric ones [27], the differences in the research fields of dielectric nano antennas and plasmonic nanoantennas are arguably *semantic* since the equations and theory behind them are the same. A general theory, with a long standing history [21, 55, 56], used to explain the scattering of any of these dielectric or metallic nanoantennas is exposed next.

An approach that is followed throughout this thesis to explain experiments and build theory, is the notion that one can decompose the response of a complex nano antenna in a handful of terms, ordered in importance according to the concept of a multipole expansion. This is easily understood starting from the general problem of scattering [57]. The solutions of Maxwell equations in free space give us all the possible modes in which electromagnetic radiation can exist in the open universe. Some solutions for these equations are readily known, as are the ubiquitous plane waves, spherical and cylindrical waves. When light in a plane wave in free space meets a very small piece of dust¶ this plane wave will in general undergo a change of direction and even possibly color. In this thesis we will focus *only* on the first type of scattering process, i.e. linear optics, where only the direction and polarization is changed but not the color. The scattering process redistributes the light over all directions, a process

---

¶Size on the order of 0.1 μm for typical aerosols.

mathematically abstracted as a spherical wave centered at the dust particle, with a superimposed angle-dependent amplitude and phase function, which determines the so-called "differential scattering cross section". To simplify this problem we start from Maxwell's equations for homogeneous space, cast in the wave equation with $k = k_0\sqrt{\epsilon\mu}$

$$(\nabla \times \nabla \times + k^2)\mathbf{E} = 0 \tag{1.4}$$

$$(\nabla \times \nabla \times + k^2)\mathbf{H} = 0. \tag{1.5}$$

Simultaneously we take into account the divergence condition,

$$\nabla \cdot \mathbf{E} = 0 \tag{1.6}$$

$$\nabla \cdot \mathbf{H} = 0. \tag{1.7}$$

As shown in the book of Jackson [21] these sets of equations can be combined in one single set by using the path suggested by Bouwkamp and Casimir [58] which is based on using $\mathbf{r}.\mathbf{E}$ and $\mathbf{r}.\mathbf{H}$ in the Helmholtz equation, as in:

$$(\nabla^2 + k^2)\mathbf{r} \cdot \mathbf{E} = 0 \tag{1.8}$$

$$(\nabla^2 + k^2)\mathbf{r} \cdot \mathbf{H} = 0, \tag{1.9}$$

It is of course very well known that Eq. (1.4) in free space gives rise to plane wave solutions of transverse electromagnetic waves. A different basis spanning all solutions to Maxwell's equations in a homogeneous medium based on spherical waves can be derived from Eq. (1.8). When these equations are solved we obtain a general solution to the Maxwell's equations with the form:

$$\mathbf{E}(r,\theta,\phi) = \sum_{n=1}^{\infty} \sum_{m=-n}^{n} [a_{nm}\mathbf{N}_{nm}(r,\theta,\phi) + b_{nm}\mathbf{M}_{nm}(r,\theta,\phi)], \tag{1.10}$$

where $\mathbf{N}_{nm}$ and $\mathbf{M}_{nm}$ are so-called "vector spherical harmonics". The "vector spherical harmonics" form a complete set of orthonormal basis functions and represent spherical waves: they have a radial part expressed in spherical Bessel and Hankel functions that contain asymptotic e^{ikR}/R dependence. As a function of polar and azimuthal dependence they are much like the spherical harmonics known from quantum mechanics, though as expected, intricacies arise from the vector nature of light and the polarization conditions coming from Eq. (1.6) and Eq. (1.7). Each order n corresponds to a multipole order, starting with the electric/magnetic dipole and quadrupole for n=1,2 for the basis functions $\mathbf{N}_{nm}$ and $\mathbf{M}_{nm}$, respectively. Quantifying the physics of a single scatterer hence equates to calculating all the multipolar expansion coefficients a_{nm} and b_{nm} induced in response to some driving. In plasmonics and metamaterials, one often argues that only leading terms (n=1, maybe n=2) are important for scattering plane waves, while higher order multipoles become important specially as one considers the effect antennas have on emitters placed in their immediate vicinity.

While Eq. (1.10) provides the full field radiated by a scatterer, it is often insightful to think in terms of equivalent current distributions of the first few terms. Indeed

many works in literature are related to identifying such currents in full-wave near-field distributions [59]. By abstracting scatterers in this way we can represent small optical antennas by the most predominant type of currents driven in them. That is, if we have a linear antenna as in Fig. 1.3a where we can mostly excite linear oscillatory currents we could replace it in our problem by an electrical dipole and also for instance the split ring in Fig. 1.3b by a circular oscillatory current and a negative linear oscillatory current.
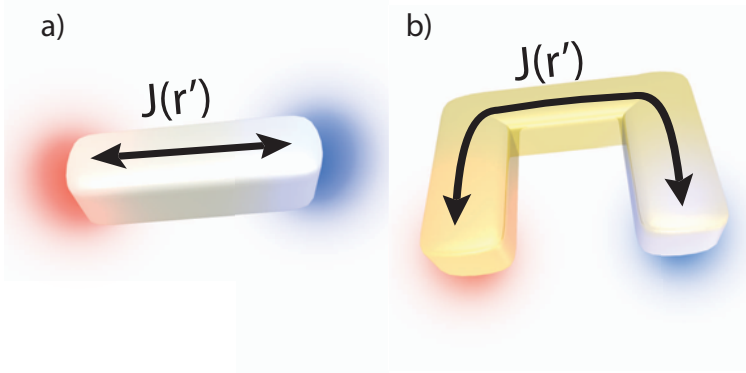
Figure 1.3: Sketch of: a) a silver rod and the linear currents driven in it and b) a gold split ring with the circular currents driven in it.

In order to be able to find what are the fields that the induced currents in our antennas radiate we need the expression

$$\mathbf{E}(\mathbf{r}) = i\omega\mu_0\mu \int_\Omega \overline{\mathbf{G}}(\mathbf{r},\mathbf{r}')\mathbf{J}(\mathbf{r}')d\mathbf{r}' = i\omega\mu_0\mu \int_\Omega \left(\mathbf{J}(\mathbf{r}')^\top \overline{\mathbf{G}}(\mathbf{r},\mathbf{r}')^\top\right)^\top d\mathbf{r}' \tag{1.11}$$

where $\mathbf{G}$ is the dyadic Green's function of free space and $\mathbf{J}(\mathbf{r}')$ is the current distribution created in our antennas. Generally the dyadic Green's function $\mathbf{G}$ satisfies

$$\nabla \times \nabla \times \overline{\mathbf{G}} - k^2\overline{\mathbf{G}} = \overline{\mathbf{I}}\delta(\mathbf{r}-\mathbf{r}'), \tag{1.12}$$

where $k = k_0\sqrt{\epsilon\mu}$ is the wave number and $\delta(\mathbf{r}-\mathbf{r}')$ is the distribution delta function. In practice $\mathbf{G}$ is only known for a few cases, including free space, homogeneous environments, multilayered infinite systems, sphere and ellipsoidal cylinders. The Green's function is extremely useful and it has been used for integral equation methods such as the method of moments and boundary element methods [60, 61]. For free space and homogeneous environments in its closed form $\mathbf{G}$ is:

$$\overline{\mathbf{G}}(\mathbf{r},\mathbf{r}') = \left[\overline{\mathbf{I}} + \frac{1}{k^2}\nabla\nabla\right]G_0(\mathbf{r},\mathbf{r}') \tag{1.13}$$

$$G_0(\mathbf{r},\mathbf{r}') = \frac{e^{\pm ik|\mathbf{r}-\mathbf{r}'|}}{4\pi|\mathbf{r}-\mathbf{r}'|}. \tag{1.14}$$

The Green's function for homogenous space as well as for a half infinite layer and a waveguiding layer will be commonly used throughout this thesis. For a deeper introduction in how to find it and use it we refer to the book of Novotny [32] as well as the book of Tai [60].

Having the expression in Eq. (1.11) we can calculate the field created by a given antenna whose most predominant currents have been determined. For this purpose we need an expression for the current of the different multipolar currents. Specifically the currents $\mathbf{J}(\mathbf{r}')$ for the first three multipoles are [62]:

$$\mathbf{J}_{\text{Electric Dipole}}(r) = -(i\omega)\delta(\mathbf{r} - \mathbf{r}')\mathbf{p} \tag{1.15}$$

$$\mathbf{J}_{\text{Magnetic Dipole}}(r) = (1/\mu_0\mu)\delta(\mathbf{r} - \mathbf{r}')\mathbf{m} \times \nabla \tag{1.16}$$

$$\mathbf{J}_{\text{Quadrupole}}(r) = -(i\omega/3!)\delta(\mathbf{r} - \mathbf{r}')\overline{\mathbf{Q}} \cdot \nabla \tag{1.17}$$

where $\mathbf{p}$ is a vector that defines the electric dipolar strength, $\mathbf{m}$ is the magnetic dipolar strength vector and $\overline{\mathbf{Q}}$ is the electric quadrupolar strength tensor. The symbol $\delta(\mathbf{r} - \mathbf{r}')$ is the distribution delta function that implies that the distribution of these currents is localized in a point located at $\mathbf{r}'$.

1.3 Polarizability tensor

In section 1.2 we have described how an antenna in which a certain current distribution has been induced can be described as a combination of basis current distributions called multipoles. We have also shown how these current distributions would radiate their power away from the antenna. We have not discussed here yet how such current distributions are created in the material of the optical antennas in the first place, which is embodied in how a_{nm} and b_{nm} obtain their values. The ease with which a certain charge distribution is created on a given antenna is quantified to first order by the polarizability $\overline{\alpha}$ of the object (see also Eq. (1.3) for the polarizability of a small scatterer). Thus for a given antenna the electric dipolar moment $\mathbf{p}$ (equivalent to a linear oscillatory current) created by an electric field $\mathbf{E}$ can be described as:

$$\mathbf{p} = \overline{\alpha}\mathbf{E}. \tag{1.18}$$

In general electric fields applied along different orientations will drive currents in the antennas with different strengths and directions. Since the electric field is a vector and the current distribution is also a vector, the most general form to describe the polarizability is by a 3 by 3 second rank tensor. We will show in this thesis that this tensor may also be extended to contain the information related to the magnetic dipolar currents and their driving as well as to electric quadrupolar currents. The former can be found in Ref. [63] while the latter is part of the original work of this thesis.

## 1.4   Nano antennas on substrates and waveguides

In section 1.2 and 1.3 we very briefly reviewed the general approach of induced multipole moments to discuss the induced currents and radiated fields of subwavelength antennas. Indeed, if one would solely study subwavelength antennas in free space, one could envision experiments to directly measure radiation patterns, i.e., far field distributions of radiated fields, and thus map multipole expansions directly. In this thesis, we are concerned primarily with the idea that in future applications, antennas are likely not in free space. For instance, using an antenna to improve LEDs or solar cells, means that it must sit in a layered, generally high index semiconductor structure, likely close to an interface. When thinking of sensors, an antenna would likely sit on a glass substrate, or be integrated with a dielectric waveguide.

Once an antenna is integrated in a nonhomogeneous environment, such as when it is placed on a planar substrate two distinct effects become important. First, a given current distribution will have a strongly modified radiation pattern. A second, and more intricate effect, is that for a given object the ease with which an applied external field sets up a material polarization changes. We will now discuss these two facts in turn for the case of a simple electric dipole. Starting with a given current distribution of an electric dipole we may find its radiation pattern by using Eq. (1.11). If we place this current distribution in free space we obtain a radiation pattern as the one shown in Fig. 1.4a. If we change the environment of this current distribution, the reflections and scattering produced by the environment, will drastically transform the total radiation pattern as shown in Fig. 1.4b where the same dipolar current was positioned 10 nm away from a glass substrate. This figure shows how most of the radiation is directed into the substrate in a narrow angular distribution. Fig 1.4a and b thus form a clear example that for the radiation pattern the presence of the environment is as important as the current distribution in the antenna itself (this can also be seen in Eq. (1.11)).

To illustrate the second effect, i.e. how the environment changes the ease with which an applied external field sets up a material polarization, we consider the case where an electric field drives an electrically polarizable object creating a dipole moment,

$$\mathbf{p} = \overline{\alpha} \cdot \mathbf{E}_{\text{total}}(\mathbf{r}') \tag{1.19}$$

where $\mathbf{p}$ is the dipole moment, $\overline{\alpha}$ is the polarizability of the object and $\mathbf{E}_{\text{total}}$ is the total electric field at the center position of the object which is mathematically considered as a point-like dipolar current distribution centered at $\mathbf{r}'$. If the object is not in free space but in some more complex environment, the total electric field at the scatterer is composed not only of the externally incident field $\mathbf{E}_{\text{in}}$, but also contains any field that the scatterer itself has radiated into the environment and which subsequently returns to the scatterer, labeled here as $\mathbf{E}_{\text{scatt}}$, that is $\mathbf{E}_{\text{total}} = \mathbf{E}_{\text{in}} + \mathbf{E}_{\text{scatt}}$. This scattered light is exactly accounted for by the so-called "Scattered part of the Green function" where we separate $\overline{\mathbf{G}} = \overline{\mathbf{G}}_0 + \overline{\mathbf{G}}_{\text{scatt}}$ into a free space part, and a scattered part that quantifies the multiple scattering caused by the complex environment. For instance, if we consider a scatterer that is brought to a mirror, the scattered part of the Greens function contains the reflected field, and is proportional to the mirror reflection coefficients. Therefore

a) Free Space

$\mathbf{p}_z$

b) On Glass Substrate

$\mathbf{p}_z$ | 10 nm
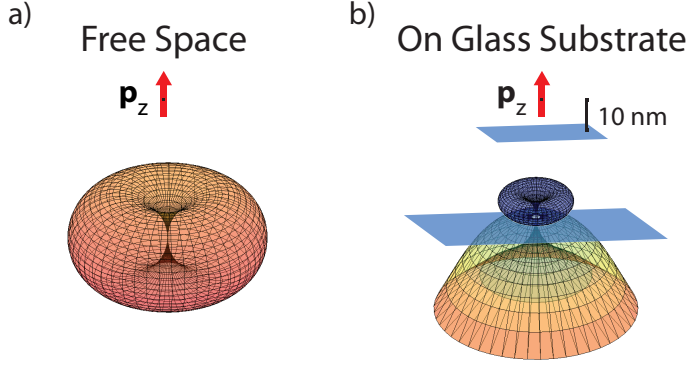
Figure 1.4: Radiation patterns of a z oriented electrical dipole in a) free space and b) 10 nm away from the top of a glass substrate. These graphs are polar diagrams of radiated intensity. That means that for a given viewing direction, θ and ϕ, the distance to the origin is proportional to how much power is radiated.

we find that our induced current equals,

$$\mathbf{p} = \overline{\alpha}\mathbf{E}_{\text{in}} + \overline{\alpha} \cdot \omega^2 \mu_0 \mu \overline{\mathbf{G}}_{\text{scatt}}(\mathbf{r}',\mathbf{r}') \cdot \mathbf{p}. \tag{1.20}$$

By using a little bit of algebra we can turn this expression into

$$\mathbf{p} = \overline{\alpha}_{\text{corr}}\mathbf{E}_{\text{in}} \tag{1.21}$$

where,

$$\overline{\alpha}_{\text{corr}}^{-1} = \overline{\alpha}^{-1} - \omega^2 \mu_0 \mu \overline{\mathbf{G}}_{\text{scatt}}(\mathbf{r}',\mathbf{r}') \tag{1.22}$$

This last expression shows a 'corrected' polarizability. With this corrected polarizability we can deal with the response of the scatterer in a complex system while taking into account self consistently all the multiple scattering between the scatterer and its environment. In general, $\overline{\mathbf{G}}_{\text{scatt}}(\mathbf{r},\mathbf{r}')$ can contribute both a real and an imaginary correction to alpha. If α is a Lorentzian response function, as for a simple model for a plasmon sphere, this constitutes a change in resonance frequency (Re$\left\{\overline{\mathbf{G}}\right\}$) and a change in radiation damping (Im$\left\{\overline{\mathbf{G}}\right\}$). Returning to the mirror example, these can be easily understood. Suppose we place a dipole in front of a perfect mirror, so that $\overline{\mathbf{G}}_{\text{scatt}}$ can be approximated using image charge theory. Qualitatively, the induced dipole in the scatterer will hybridize with its mirror image. Depending on the relative alignment of the mirror image and the original dipole, this will give rise either to a blue- or red shift in energy (as evident from an electrostatic energy consideration), as well as to a net increase or decrease of net radiative damping, i.e., radiated power per unit of induced dipole moment. This correction is identical to the radiative line width and resonance frequency changes experienced by spontaneous emitters, like atoms and molecules, held

in front of an interface [64], due to backaction of the radiated source field on the source itself. In fact, in order to obtain a scattering theory that satisfies energy conservation, an equation of the form of Eq. (1.22) is required to correctly define the polarizability of an object in vacuum. In such a case, one requires that the entries for Eq. (1.22) contain the electrostatic polarizability of the object α, defined as $\alpha = 3V(\epsilon - \epsilon_{\mathrm{env}})/(\epsilon + 2\epsilon_{\mathrm{env}})$ (for a sphere) and $\overline{\mathbf{G}}_{\mathrm{scatt}}$ replaced by $\mathrm{Im}\left\{\overline{\mathbf{G}}_0\right\} = \omega\sqrt{\epsilon\mu}/(c6\pi)$. Here the factor $\mathrm{Im}\left\{\overline{\mathbf{G}}_0\right\}$ quantifies the backaction a dipole experiences in a homogeneous environment, and is equivalent to the local density of states. This correction to the polarizability is also known as a Sipe-Kranendonk correction [65], or dynamic correction. With the corrected polarizability tensor we are able to handle the inclusion of any substrate for which we have its Green's function as long as we know what is the polarizability tensor of one such an optical antenna.

The point dipole and multipole picture is often used in the field of plasmonics to guide qualitative understanding of experimental results and full wave calculations. The main proposition of this thesis is that, when applied with care, this picture can also be pushed to give quantitative predictions of antenna physics. While it is not a replacement for all problems solved with full wave calculations, this type of simplification could mean a considerable economization of time in design and simulation tasks, and it helps to build an intuitive picture of the scattering processes. This saving of time would allow for numerical optimizations of designs of multielement scatterers for improvement of LED illumination, increased solar cell efficiencies, or also higher field confinements for waveguide integrated single molecule read out and control. In this thesis we will expose examples of how to use an extended point dipole theory corrected for the presence of non trivial environments like substrates and waveguides. We will show how this method is able to explain experimental results and how it is suitable for designs of novel antennas.

1.5   Outline of this thesis

We begin this thesis by reporting scattering experiments on single rod plasmonic nano antennas fabricated on top of a Si_3N_4 ridge waveguide (chapter 2). This study was done to asses how strongly light propagating in guided modes interact with plasmon antennas, with the ultimate goal to provide an on-chip plasmon building block for interconversion between guided modes and strongly localized fields that could, for instance, interact with active materials. For this study we use point dipole theory to unravel the performed measurements. We continue showing how by using point dipole theory we can design a multi element Yagi-Uda antenna that maximizes the incoupling of light from a single emitter, in the proximity of the antenna, into the guided mode of a waveguide (chapter 3). In this chapter we show how the system of a plasmonic antenna plus dielectric waveguide represents a very interesting technology for controlling and detecting the emission of quantum light sources, e.g. atoms, molecules or quantum dots.

To complement the experiments done in chapter 3 we used a cathodoluminescence

measurement setup to generate nanometric position controlled point sources on Yagi-Uda antennas. By using point dipole theory and a statistical analysis we explain the features appearing in the acquired spatial excitability maps. Also, we show how random changes in the size of antenna elements result in a high variability of near field high and low excitability positions which contrast with the rather robust directionality and directivity found for these antennas (chapter 4).

In (chapter 5) of this thesis we present a numerical tool with which the polarizability tensor of any optical antenna with an arbitrary geometry can be retrieved. This retrieval is done in order to be able to use point dipole theory in more general problems, involving optical antennas with virtually any shape, while not needing microscopic analytical expressions for the polarizability tensor of the antennas. We use the retrieval tool to explain the behaviour of one of the most iconic optical antennas, the split ring resonator. Besides explaining its scattering properties and exotic pseudochirality we use the multipolar expansion of this antenna to design a novel split ring based multi-element antenna with very interesting characteristics as a directive radiation source of elliptically polarized light from a localized point source (chapter 6).

Having set the stage for retrieving the polarizability tensor of an arbitrary antenna, we expand the point dipole model to include electric quadrupolar moments. We use this extended theory to analyze the behavior of two types of antennas. The first of these is the so-called "dolmen" antenna that consists of a nanorod that is a strongly dipolar scatterer coupled to a dimer of nanorods that was reported in literature to support a very strongly quadrupolar mode. In particular, we quantify the claim made in earlier reports that narrow features in the dolmen extinction spectrum known as "Fano interference" or "plasmon-induced transparency" are attributable to a quadrupolar response. The second of these antennas concerns nanopyramids made out of aluminium. Through optimization of their simultaneous electric dipole, magnetic dipole, and electric quadrupole response these allow strongly directional scattering, as well as strongly directed enhancement of emission of nearby emitters. These nano pyramids are shown to be suitable for vertical asymmetric field confinement that could be used for enhancing LED illumination and solar cells (chapter 7).

Finally we show how to use the extended point quadrupole-dipole theory in the presence of a substrate. We explain measurements of nano cylinders with strong quadrupolar moments, measured in a cathodoluminescence setup, which are capable of strongly directing light by the interference of its different multipolar moments. These "nano lighthouses" have the characteristic that they are capable of strongly directing scattered light although the antenna is composed of one single element (chapter 8).

References

[1] K. Friston, *The free-energy principle: a unified brain theory?*, Nat Rev Neurosci **11**, 127 (2010).

[2] J. G. Purbuchok, *Explanation of the Presentation of Objects and Object-Possessors as well as Awarenesses and Knowers*, FPMT, 2003.

[3] S. Bradbury and B. Bracegirdle, *Introduction to Light Microscopy*, BIOS Scientific, 1998.

[4] E. Betzig, G. H. Patterson, R. Sougrat, O. W. Lindwasser, S. Olenych, J. S. Bonifacino, M. W. Davidson, J. Lippincott-Schwartz, and H. F. Hess, *Imaging intracellular fluorescent proteins at nanometer resolution*, Science **313**, 1642 (2006).

[5] B. Lubsandorzhiev, *On the history of photomultiplier tube invention*, Nuclear Instruments and Methods in Physics Research Section A: Accelerators, Spectrometers, Detectors and Associated Equipment **567**, 236 (2006), Proceedings of the 4th International Conference on New Developments in Photodetection {BEAUNE} 2005 Fourth International Conference on New Developments in Photodetection.

[6] D. Carter, *Photomultiplier handbook: Theory, design, application*, Lancaster,(PA): Burle Industries, Inc (1980).

[7] R. Abbasi and et. al., *Calibration and characterization of the icecube photomultiplier tube*, Nuclear Instruments and Methods in Physics Research Section A: Accelerators, Spectrometers, Detectors and Associated Equipment **618**, 139 (2010).

[8] J. M. Pasachoff, *Contemporary Astronomy*, Saunders College Publishing, 2nd edition, 1981.

[9] J. H. István Horváth and Z. Bagoly, *Possible structure in the grb sky distribution at redshift two*, Astronomy and Astrophysics **561**, L12 (2014).

[10] T. Stocker, D. Qin, G.-K. Plattner, M. Tignor, S. Allen, J. Boschung, A. Nauels, Y. Xia, V. Bex, and P. Midgley, editors, *Climate Change 2013: The physical science basis. contribution of working group I to the fifth assessment report of the intergovernmental panel on climate change*, Cambridge University Press, 2013.

[11] http://ec.europa.eu/clima/policies/ets/index_en.htm.

[12] http://ec.europa.eu/europe2020/index_en.htm.

[13] D. J. MacKay, *Sustainable Energy-without the hot air*, UIT Cambridge, 2008, Available free online from www.withouthotair.com.

[14] http://esa.un.org/wpp/.

[15] http://www.eia.gov/cfapps/ipdbproject/IEDIndex3.cfm.

[16] D. J. Miller, P. M. Watts, and A. W. Moore, *Motivating future interconnects: A differential measurement analysis of pci latency*, in *Proceedings of the 5th ACM/IEEE Symposium*

on Architectures for Networking and Communications Systems, ANCS '09, pages 94–103, New York, NY, USA, 2009, ACM.

[17] http://public.itrs.net/.

[18] H. A. Atwater and A. Polman, *Plasmonics for improved photovoltaic devices*, Nat Mater **9**, 205 (2010).

[19] Y. Vlasov, *Silicon cmos-integrated nano-photonics for computer and data communications beyond 100g*, Communications Magazine, IEEE **50**, s67 (2012).

[20] J. A. Gledhillt, *The range-energy relation for 0.1-600 kev electrons*, J. Phys. A: Math., Nucl. Gen., **6** (1973).

[21] J. D. Jackson, *Classical Electrodynamics*, Wiley, New York, third edition, 1999.

[22] W. L. Barnes, A. Dereux, and T. W. Ebbesen, *Surface plasmon subwavelength optics*, Nature **424**, 824 (2003).

[23] L. Novotny and N. van Hulst, *Antennas for light*, Nat. Photon. **5**, 83 (2011).

[24] V. Giannini, A. I. Fernáandez-Domínguez, S. C. Heck, and S. A. Maier, *Plasmonic nanoantennas: Fundamentals and their use in controlling the radiative properties of nanoemitters*, Chem. Rev. **111**, 3888 (2011).

[25] A. E. Krasnok, I. S. Maksymov, A. I. Denisyuk, P. A. Belov, A. E. Miroshnichenko, C. R. Simovski, and Y. S. Kivshar, *Optical nanoantennas*, Physics-Uspekhi **56**, 539 (2013).

[26] M. P. van Albada, B. A. van Tiggelen, A. Lagendijk, and A. Tip, *Speed of propagation of classical waves in strongly scattering media*, Phys. Rev. Lett. **66**, 3132 (1991).

[27] B. Rolly, B. Stout, and N. Bonod, *Boosting the directivity of optical antennas with magnetic and electric dipolar resonant particles*, Opt. Express **20**, 20376 (2012).

[28] A. Ahmadi and H. Mosallaei, *Physical configuration and performance modeling of all-dielectric metamaterials*, Phys. Rev. B **77**, 045104 (2008).

[29] A. Krasnok, D. Filonov, A. Slobozhanyuk, C. Simovski, P. Belov, and Y. Kivshar, *Superdirective dielectric nanoantennas with effect of light steering*, arXiv:1307.4601v1 , 8 (2013).

[30] E. Verhagen, S. Deleglise, S. Weis, A. Schliesser, and T. J. Kippenberg, *Quantum-coherent coupling of a mechanical oscillator to an optical cavity mode*, Nature **482**, 63 (2012).

[31] M.-S. Hu, H.-L. Chen, C.-H. Shen, L.-S. Hong, B.-R. Huang, K.-H. Chen, and L.-C. Chen, *Photosensitive gold-nanoparticle-embedded dielectric nanowires*, Nat Mater **5**, 102 (2006).

[32] L. Novotny and B. Hecht, *Principles of Nano-optics*, Cambridge University Press, Cambridge, 2006.

[33] T. Feichtner, O. Selig, M. Kiunke, and B. Hecht, *Evolutionary optimization of optical antennas*, Phys. Rev. Lett. **109**, 127701 (2012).

[34] H. Cang, A. Labno, C. Lu, X. Yin, M. Liu, C. Gladden, Y. Liu, and X. Zhang, *Probing the electromagnetic field of a 15-nanometre hotspot by single molecule imaging*, Nature **469**, 385 (2011).

[35] T. R. Jensen, R. P. V. Duyne, S. A. Johnson, and V. A. Maroni, *Surface-enhanced infrared spectroscopy: A comparison of metal island films with discrete and nondiscrete surface plasmons*, Appl. Spectrosc. **54**, 371 (2000).

[36] J. Kundu, F. Le, P. Nordlander, and N. J. Halas, *Surface enhanced infrared absorption (seira) spectroscopy on nanoshell aggregate substrates*, Chem. Phys. Lett. **452**, 115 (2008).

[37] K. Nakata, Y. Kayama, K. Shimazu, A. Yamakata, S. Ye, and M. Osawa, *Surface-enhanced infrared absorption spectroscopic studies of adsorbed nitrate, nitric oxide, and related compounds 2: Nitrate ion adsorption at a platinum electrode*, Langmuir **24**, 4358 (2008).

[38] F. Le, D. W. Brandl, Y. A. Urzhumov, H. Wang, J. Kundu, N. J. Halas, J. Aizpurua, and P. Nordlander, *Metallic nanoparticle arrays: A common substrate for both surface-*

enhanced raman scattering and surface-enhanced infrared absorption, ACS Nano **2**, 707 (2008).

[39] N. Liu, M. Mesch, T. Weiss, M. Hentschel, and H. Giessen, *Infrared perfect absorber and its application as plasmonic sensor*, Nano Lett. **10**, 2342 (2010).

[40] L. Billot, M. L. de la Chapelle, A.-S. Grimault, A. Vial, D. Barchiesi, J.-L. Bijeon, P.-M. Adam, and P. Royer, *Surface enhanced raman scattering on gold nanowire arrays: Evidence of strong multipolar surface plasmon resonance enhancement*, Chem. Phys. Lett. **422**, 303 (2006).

[41] C. E. Talley, J. B. Jackson, C. Oubre, N. K. Grady, C. W. Hollars, S. M. Lane, T. R. Huser, P. Nordlander, and N. J. Halas, *Surface-enhanced raman scattering from individual au nanoparticles and nanoparticle dimer substrates*, Nano Lett. **5**, 1569 (2005).

[42] J. Ye, L. Lagae, G. Maes, G. Borghs, and P. V. Dorpe, *Symmetry breaking induced optical properties of gold open shell nanostructures*, Opt. Express **17**, 23765 (2009).

[43] A. Kinkhabwala, Z. Yu, S. Fan, Y. Avlasevich, K. Mullen, and M. E., *Large single-molecule fluorescence enhancements produced by a bowtie nanoantenna*, Nat Photon **3**, 654 (2009).

[44] A. G. Curto, G. Volpe, T. H. Taminiau, M. P. Kreuzer, R. Quidant, and N. F. van Hulst, *Unidirectional emission of a quantum dot coupled to a nanoantenna*, Science **329**, 930 (2010).

[45] H. Aouani, O. Mahboub, N. Bonod, E. Devaux, E. Popov, H. Rigneault, T. W. Ebbesen, and J. Wenger, *Bright unidirectional fluorescence emission of molecules in a nanoaperture with plasmonic corrugations*, Nano Lett. **11**, 637 (2011).

[46] M. J. Levene, J. Korlach, S. W. Turner, M. Foquet, H. G. Craighead, and W. W. Webb, *Zero-mode waveguides for single-molecule analysis at high concentrations*, Science **299**, 682 (2003).

[47] H. Rigneault, J. Capoulade, J. Dintinger, J. Wenger, N. Bonod, E. Popov, T. W. Ebbesen, and P.-F. m. c. Lenne, *Enhancement of single-molecule fluorescence detection in subwavelength apertures*, Phys. Rev. Lett. **95**, 117401 (2005).

[48] R. Thijssen, E. Verhagen, T. J. Kippenberg, and A. Polman, *Plasmon nanomechanical coupling for nanoscale transduction*, Nano Lett. **13**, 3293 (2013).

[49] P. Spinelli, V. E. Ferry, J. van de Groep, M. van Lare, M. A. Verschuuren, R. E. I. Schropp, H. A. Atwater, and A. Polman, *Plasmonic light trapping in thin-film si solar cells*, Journal of Optics **14**, 024002 (2012).

[50] R. A. Pala, J. White, E. Barnard, J. Liu, and M. L. Brongersma, *Design of plasmonic thin-film solar cells with broadband absorption enhancements*, Advanced Materials **21**, 3504 (2009).

[51] M. Frimmer and A. F. Koenderink, *Superemitters in hybrid photonic systems: A simple lumping rule for the local density of optical states and its breakdown at the unitary limit*, Phys. Rev. B **86**, 235428 (2012).

[52] M. Wulf, D. M. Beggs, N. Rotenberg, and L. Kuipers, *Unravelling nonlinear spectral evolution using nanoscale photonic near-field point-to-point measurements*, Nano Lett. **13**, 5858 (2013).

[53] N. Liu, T. Weiss, M. Mesch, L. Langguth, U. Eigenthaler, M. Hirscher, C. Sonnichsen, and H. Giessen, *Planar metamaterial analogue of electromagnetically induced transparency for plasmonic sensing*, Nano Lett. **10**, 1103 (2010).

[54] A. V. Kabashin, P. Evans, S. Pastkovsky, W. Hendren, G. A. Wurtz, R. Atkinson, R. Pollard, V. A. Podolskiy, and A. V. Zayats, *Plasmonic nanorod metamaterials for biosensing*, Nat Mater **8**, 867 (2009).

[55] E. M. Purcell and C. R. Pennypacker, *Scattering and absorption of light by nonspherical*

dielectric grains, Astrophysical Journal **186**, 705 (1973).

[56] S. B. Singham and C. F. Bohren, *Light scattering by an arbitrary particle: a physical reformulation of the coupled dipole method*, Opt. Lett. **12**, 10 (1987).

[57] A. Lagendijk and B. A. van Tiggelen, *Resonant multiple scattering of light*, Physics Reports **270**, 143 (1996).

[58] C. Bouwkamp and H. Casimir, *On multipole expansions in the theory of electromagnetic radiation*, Physica **20**, 539 (1954).

[59] B. Gallinet and O. J. F. Martin, *Relation between near–field and far–field properties of plasmonic fano resonances*, Opt. Express **19**, 22167 (2011).

[60] C. T. Tai, *Dyadic Green's Functions in Electromagnetic Theory*, IEEE Press, New York, second edition, 1993.

[61] F. J. Garcìa de Abajo and A. Howie, *Retarded field calculation of electron energy loss in inhomogeneous dielectrics*, Phys. Rev. B **65**, 115418 (2002).

[62] M. Ribaric and L. Sustersic, *Expansion in terms of moments of time-dependent, moving charges and currents*, SIAM J. Appl. Math. **55**, 593 (1995).

[63] I. Sersic, C. Tuambilangana, T. Kampfrath, and A. F. Koenderink, *Magnetoelectric point scattering theory for metamaterial scatterers*, Phys. Rev. B **83**, 245102 (2011).

[64] K. Drexhage, *Influence of a dielectric interface on fluorescence decay time*, Journal of Luminescence **1-2**, 693 (1970).

[65] J. E. Sipe and J. V. Kranendonk, *Macroscopic electromagnetic theory of resonant dielectrics*, Phys. Rev. A **9**, 1806 (1974).

2

Single Rod Antenna on a Dielectric Waveguide

For the purpose of using plasmonics in an integrated scheme where single emitters can be probed efficiently, we experimentally and theoretically study the scattering properties of single nano-rod gold antennas placed on one-dimensional dielectric silicon nitride waveguides. Using real space and Fourier microscopy correlated with waveguide transmission measurements, we quantify the spectral properties, strength and directivity of scattering. The scattering processes can be well understood in the framework of the physics of dipolar objects placed on a planar layered environment with a waveguiding layer.

2.1 Introduction

A highly promising development in nanophotonics is the use of plasmonic antennas to interface near fields and far fields [1–4]. As opposed to conventional dielectric optics that are bound by the diffraction limit, plasmonic structures can confine electromagnetic fields to very small volumes, essentially by packing energy in a joint resonance of the photon field and the free electrons in the metal. As a consequence, plasmonic structures are currently viewed as ideal structures to interface single emitters and single photons [5–16], as well as to realize many types of field-enhanced spectroscopies, such as Raman spectroscopy [17–20], SEIRA [19, 21–24], and fluorescence correlation spectroscopy [25]. Currently, most workers in the field of nano-antennas target the basic understanding and use of antennas in essentially index-matched surroundings. We propose that all the exciting properties of plasmonic nano-antennas can be used in even more versatile ways, if it would be possible to excite and interrogate the antennas efficiently in integrated photonic circuits. Dielectric waveguides, such as high index

ridges on low index substrates, represent a common and mature photonic integration technology. [26, 27] We envision local integration of plasmonic antennas as a promising route to enhance conventional dielectric photonic circuits, and to achieve excitation and detection of plasmonic antenna resonances in an integrated fashion. In order to ultimately apply this combination of structures it is important to understand exactly how antennas interact with waveguides, *i.e.*, how the antenna scatters the waveguide modes, and conversely how the waveguide affects the antenna resonance frequencies, resonance profiles, and directivity. In view of these exciting possibilities, it is highly desirable to comprehensively quantify first how strongly single plasmon building blocks couple to waveguide modes, and how strongly waveguide modes couple to radiation channels outside the waveguide. Such a comprehensive experimental study can then in a second step be used as input to a toolbox for designing phased array antennas. In this chapter we focus on the first part, i.e. the comprehensive quantification of the scattering by single rod antennas on dielectric waveguides. This study will be used in chapter 3 for the design of phased array antennas.

2.2   Experimental setup and methods

In order to study antennas coupled to dielectric waveguides, we employ a setup that combines a fiber-coupled end-fire setup with a confocal microscope as seen in figures 2.1a and 2.1b. The setup can be used in two configurations, as further highlighted in the sketches presented on the left side of the figures. In the first configuration of the setup shown in Fig. 2.1a light is coupled from one end facet into the waveguide using a cleaved fiber (Nufern S630_HP) that carries excitation light from a Fianium supercontinuum light source (SC-450-PP, with the spectrum after the fiber ranging from 650 to 900 nm, max. power at 725 nm of 0.680 mW when measured through bandpass filter 700 nm FWHM 50 nm). Light is coupled into the waveguide and transmitted into a second fiber for spectral analysis on an Avantes peltier cooled Si CCD array spectrometer (AvaSpec-2048TEC-USB2-2). To quantify the scattered light spectrally, spatially and in terms of wave vector content, a home built microscopy system is placed with its optical axis perpendicular to the sample substrate. We use an Olympus 100x, NA 0.95 M Plan IR objective to collect the scattered light, which is then directed through a tube lens to a CCD camera (The Imaging Source DMK21AU04) for imaging, or to a Thorlabs galvo scanner system. This galvo system scans the scattered light collected from the sample plane over a 50 μm core multimode fiber which acts as a confocal pinhole (sample-to-fiber magnification 228 times). This fiber brings out-of-plane scattered light onto a second channel of the same Avantes spectrometer. This confocal scanning configuration for out-of-plane scattering allows us to retrieve images of the sample as well as the spectral content of light scattered from different parts of the antenna. As further functionality, we can flip in a so-called Fourier or Bertrand lens that allows conoscopic imaging. In other words, when flipping in the Fourier lens we retrieve the intensity distribution of scattered light over all wave vectors in the objective NA, essentially through imaging the back focal plane (BFP) of the
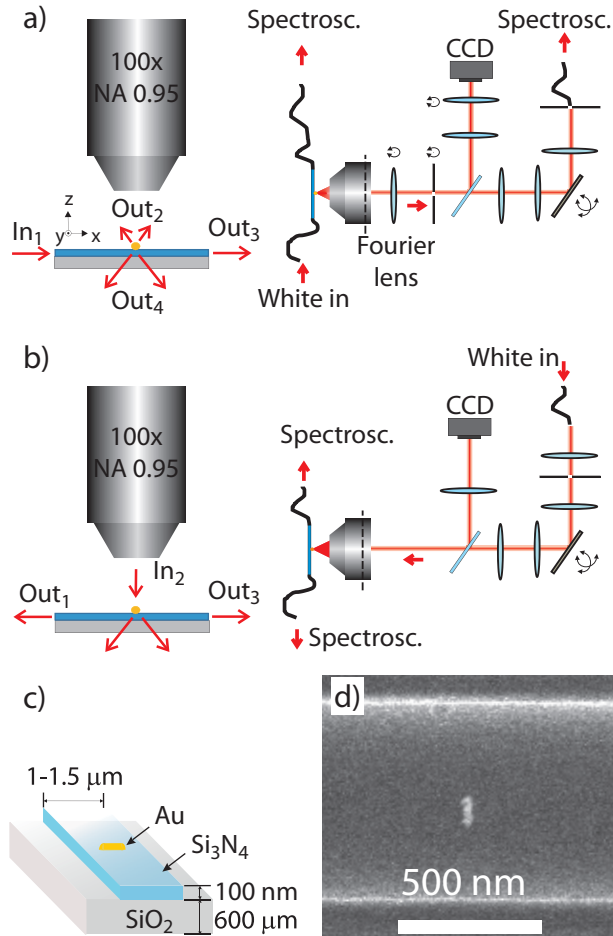
Figure 2.1: Schematic overview of the experimental setup [a) and b)] together with the representation of the two main working modes. In panels c) and d) the pictures present a schematic view of the sample used together with a scanning electron micrograph of a typical result of a fabricated Si_3N_4 waveguide with a deposited Au antenna.

imaging objective [25, 28–35]. By using a pinhole system at a distance equal to the focal distance $f_{Fourier}$ from the Fourier lens we spatially filter the scattered light prior to wave vector imaging, so that we collect radiation patterns only from those parts of the sample that we are interested in, namely the antennas. The Fourier image can again be collected panchromatically on the CCD, or through the galvo scanning mirrors by the fiber, which allows us to spectrally resolve the differential scattering cross section. To conclude, with this configuration of the setup we can study the effect of the antenna on the waveguide transmission (channel 3 in Fig. 2.1a) and scattering of the antenna into the air side (channel 2 in Fig. 2.1a). Given the thickness of the quartz substrate

used for the samples (∼ 600 μm), a home made solid immersion lens system (SIL) was required in order to also access scattering into the substrate side (depicted as channel 4 in Fig. 2.1a), as the Olympus objective lacks the required working distance. This SIL system that employs a BK7 glass hemisphere of diameter 2 mm, allowed us also to collect light that was scattered by the antennas into angles that exceed the total internal reflection angle of the substrate, however, only with spherical and chromatic imaging aberrations too large to allow diffraction limited and Fourier imaging.

The second configuration of the microscope in Fig. 2.1b is designed to study the converse interaction, *i.e.*, rather than coupling in through the waveguide and collecting scattered light, we study how light coming from free space (channel 2 in Fig. 2.1b) is coupled into the waveguide mode. This configuration is achieved by swapping the spectrometer-coupled detection fiber that is placed after the galvo system with the combination of a pinhole system and free space collimated supercontinuum light from the Fianium source. The light scattered into the waveguide and detected through the fibers at the end facets is sent to the spectrometer to quantify the "forward" and "backward" waveguide in-coupling spectra. In absence of the Bertrand lens, we couple in light locally using real space focusing at the diffraction limit. When we flip the Bertrand lens in so that the incident beam is focused in the objective back aperture, we couple light in over a large area, yet at a well-defined incident angle that can be freely varied over the entire objective NA.

Normalization of the scattering excited via the waveguide

A particularly difficult problem is how to quantitatively normalize the spectrum of light scattered by the antennas to the spectrum that is offered through the waveguide to the antenna. The only possible references we have access to are the spectra measured in transmission through nominally identical blank waveguides (*i.e.*, without antennas) as a measure for the incident spectrum, and spectra obtained from scattering centers that appear comparatively close to the antenna, due to roughness of the waveguide. In the first case, artifacts may occur due to the fact that the spectrum may vary between alignments and between waveguides, due to chromatic effects in coupling to the waveguide, and for the 1 cm long waveguides due to the integrated effect of unexpected small defects and impurities that change the spectrum along the length of the waveguide. In the second approach, the advantage is that spectra are taken from a region very close to the structure. However, one here relies on the assumption that the scattering centers have no strong frequency dependence, and one does not obtain a quantitative signal strength comparison, as opposed to when using waveguide transmission. In practice no large difference between the two approaches is found when spectrally locating the resonance. Here we present data using the second method (normalization to nearby scattering centers), preferring spectral fidelity over an absolute scale.

Sample fabrication

The samples used for the experiments are composed of gold antennas fabricated on top of silicon nitride waveguides by aligned electron beam lithography. A sketch of the structures used is shown in Fig. 2.1c. As we ultimately target visible light spectroscopy applications, we consider silicon nitride waveguides. Fused silica wafers (n=1.45) of 100 mm diameter were covered with 100 nm thick Si_3N_4 using a LPCVD process. This process [Lionix BV, The Netherlands] ensures low loss Si_3N_4 at manageable stress levels for postprocessing. In order to define 1D waveguide ridges, we perform e-beam lithography using a Raith e-line machine. The waveguides together with positioning markers that are used at a later stage were defined in MaN2403 negative resist (200 nm thickness) with an electron beam lithographic step [dose 235 $\mu C/cm^2$, 35 nm spot size, current 0.14 nA and a fixed beam movable stage (FBMS) step size of 0.01 μm]. The pattern was then transferred into the Si_3N_4 by dry etching (Oxford Plasmalab, 50 sccm CHF_3 and 5 sccm O_2, 100 W forward RF power, 5 min etching time). In a second electron beam lithography step the antennas were defined on top of the waveguides, using alignment markers fabricated in the Si_3N_4 for precise positioning. In this step ZEP-520A positive resist (125 nm thick, exposed with a line dose of 200 pA s/cm, 29 nm spot size, current 0.03 nA) was used to define a liftoff mask for thermal vapor deposition of gold. To mitigate the very poor adhesion of gold on Si_3N_4, in the evaporation step we first deposited a thin chromium adhesion layer of ~3 nm, prior to the deposition of ~30 nm of gold. A typical final result is shown in Fig. 2.1d.

In this chapter we discuss only one type of antenna namely the single rod 100 nm long antennas. This antenna is composed of 1 element with a length of 100 nm and a height of 30 nm as controlled by the gold evaporation. While we have studied antennas on various waveguide widths, all the data presented here are for waveguide widths of 1000 nm and 1500 nm. The strip height is 100 nm. We estimate the electron beam alignment accuracy of antennas to waveguides to be ~40 nm, *i.e.*, far below any typical feature of the waveguide mode structure as shown in the insets of Fig. 2.2 a and b. The dispersion relations of these waveguides as well as their mode profiles at different wavelengths are shown in Fig. 2.2. In this figure we present the dispersion relation for both type of waveguides as calculated using a finite element mode solver. Figures 2.2a and b show the profile of the waveguide modes at 750 nm and 850 nm, which, as we will see later in chapter 2 and 3, are the center wavelength of the resonances of the antennas discussed in both chapters. At these two wavelengths the waveguides present single transverse electric (TE) mode behaviour. Due to the polarization of the in-coupled light we excite only the TE modes of the waveguides. For the widest of the two waveguides shown (1500 nm width) , the second TE waveguide mode has its cutoff wavelength at around 600 nm. Choosing even wider waveguides than 1500 nm would hence imply multimode behavior in the spectral window of the plasmon resonance.
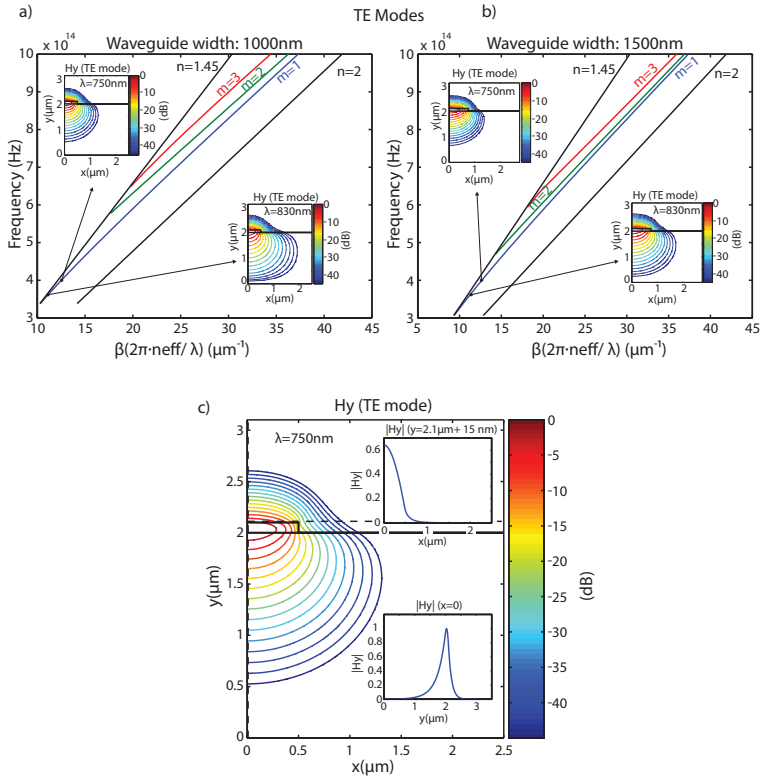
Figure 2.2: a) and b) show the dispersion relations of silicon nitride ridge waveguides on top of a fused silica substrate. The dispersion relations are calculated for waveguides of 1000 nm (a) and 1500 nm (b) width and a guiding layer thickness of 100 nm. The light lines for the silica substrate and the Si_3N_4 are the plotted black lines while the first three modes m=1, 2 and 3 are plotted with color lines. In c) we plot the mode profile for a 1000 nm wide waveguide at 750 nm wavelength. The inset of this graph shows two cuts of the profile, one through the y axis and the other along the x-axis at 15 nm from the top surface of the waveguide. This is the expected position of the center of the antennas deposited over the waveguides.

2.3 Scattering of guided modes by single element antennas

We first discuss measurements on single rod antennas excited through the 1000 nm width waveguides. These measurements are intended to obtain the resonance frequency of the single rod antennas. In order to obtain this information, TE polarized light is sent in through the waveguide (channel 1 in Fig. 2.1a), and light scattered by the antenna into the air-half space is collected and resolved on the spectrometer (channel 2). Fig. 2.3b (continuous black line) shows the spectrum of light scattered into the air side

of the sample by a 100 nm rod antenna normalized to the input intensity with which it is excited through the waveguide according to the normalization method presented in section 2.2. The antenna spectrum shows a clear peak centered around 750 nm, with a bandwidth of around 55 nm (FWHM). The resonance frequency is comparable to resonance frequencies previously found for rods on simple glass substrates [36–39]. When collecting light scattered by the antenna into the substrate underlying the waveguides using the (SIL) solid immersion lens system, we find that the resonance frequency is almost identical (Fig. 2.3b (dashed red line)). However, when comparing the intensity of the light emitted into the different media for quantitative reference, we find that a signal approximately 2 times stronger is found into the quartz substrate than into air, consistent with the fact that a higher scattering intensity towards the high index medium is expected from the radiation of dipoles on top of a high index layered system [40]. We conclude from our measurements that waveguide-addressing of plasmon antennas allows for high signal-to-noise ratio dark-field spectroscopy of single plasmon antennas both using collection of light from the air side, and from the substrate side. This conclusion is promising for integrated applications of plasmonic antennas in sensing using integrated optics. Even more promising is that detection in such a sensing scheme could also occur *via* the waveguide itself. We estimate that a single nanorod antenna removes approximately 20% of the intensity in the waveguide mode out of the transmission channel (as can be seen in Fig. 2.4) and redistributes it over waveguide reflection, absorption in the metal, and out-of-plane scattering. This estimate results from transmission spectra normalized to nominally identical blank waveguides shown in Fig. 2.4.

To obtain a more comprehensive understanding of how plasmon antennas scatter waveguide modes, we analyze the scattered light further in terms of polarization and directionality. In the remainder of this chapter we focus on collection of light on the air side of the sample, as the quality of our imaging system is far superior in this configuration. Polarization analysis shows that more than 90% of the light is scattered in the polarization direction parallel to the direction of the antenna (y direction in the reference frame depicted in Fig. 2.1a). We have also studied 100 nm rod antennas fabricated at various rotation angles relative to the waveguide axis. As the antenna is rotated from 90°, 45° to 0° angle relative to the waveguide axis, we consistently find strong polarization of scattered light collected on the air side of the sample along the antennas axis.

We have access to the directionality of scattering by the single rod antennas using Fourier microscopy, *i.e.*, by insertion of a Bertrand lens into our imaging system. While the 100 nm line rod antennas appear as diffraction limited points in spatial imaging, interesting information is obtained when looking at the scattered light by imaging the back focal plane of the objective in this manner. At the air side (channel 2 in Fig. 2.1a), the radiated pattern appears to be distributed over a wide range of angles (up to $\sin\theta = 0.7$) relative to the sample normal (Fig. 2.3c and 2.3d). Upon polarization analysis with a linear polarizer in detection we find a large contrast in integrated intensity. In addition, the weak cross-polarized radiation pattern is clearly distinct from the co-polarized pattern in that it consists of four separate lobes. Similar results were
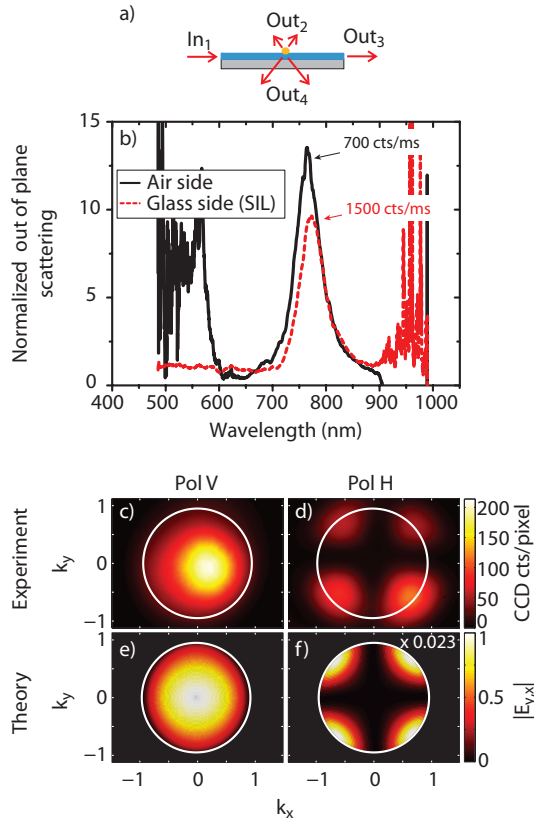
Figure 2.3: Sketch of the experimental geometry relevant for panels (b-f), in which we collect out-of plane scattering due to the antenna that is excited through the waveguide. b) Spectrum of the scattered intensity for a 100 nm long rod antenna on a 1000 nm width waveguide (continuous black line) taken from the air side of the sample. (dashed red line) taken from the glass side of the sample with a SIL. The spectrum is normalized to the light offered to the antenna, measured by integrating light scattered from roughness of the waveguide adjacent to the antenna. Both peaks show that the scattering of guided modes happens through a resonant process. c) and d) Graphs of the measured radiation pattern for the 100 nm rod antenna, analyzed through a vertical c) and horizontal d) linear polarizer. The white circle indicates the NA of the Olympus objective (N.A=0.95). The integration time for the vertical polarization is 1.45 s and 30 s for the horizontal polarization. e) and f) Graphs of the simulated radiation pattern analyzed through a vertical e) and horizontal f) linear polarizer. Field values are calculated at the position of the microscope objective, *i.e.*, 1.8 mm from the sample plane. The fields are normalized to $\mathbf{E}_y = 1.7 \times 10^{-9}$ V/m, given a guided mode strength of 1 V/m. Graphs c) to f) demonstrate that a 100 nm rod antenna located over a multi-layer substrate behaves as an electric dipolar scatterer.

reported in [28] for antennas excited using total internal reflection (TIR) on a prism. Clearly, waveguide excitation is an efficient alternative to TIR for dark-field Fourier
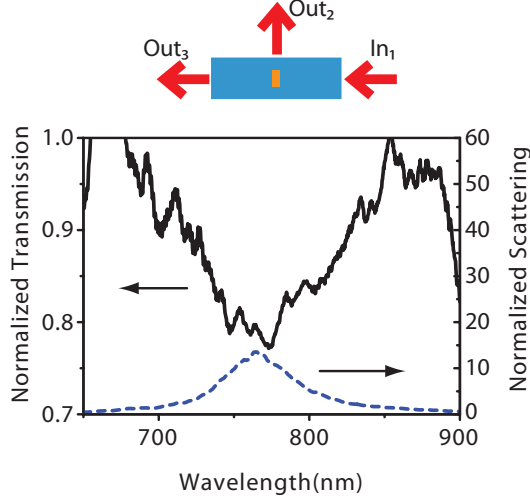
Figure 2.4: Normalized transmission spectra of a 100 nm single rod gold antenna and normalized scattering spectra of the same antenna (see section 2.2).

microscopy. We note that the fact that the radiation pattern extends somewhat *outside* the NA of our objective indicates that diffraction by the spatial selection pinhole blurs the measured radiation pattern. The radiation pattern found in the two polarization channels for the 100 nm rod antenna in Fig. 2.3c and 2.3d bears the clear signature of an in-plane y-oriented dipole placed on top of a Si_3N_4-SiO_2 substrate. In high-NA imaging, such a y-oriented dipole generates cross polarized fields at very large angles due to the huge refraction angles in the aplanatic imaging system. The measured radiation pattern for the 100 nm rod antenna, as shown in Fig. 2.3c and 2.3d is in excellent agreement with the theoretical radiation pattern that is expected for a dipolar scatterer positioned 30 nm above a 2D layer system consisting of quartz and silicon nitride as shown in Fig. 2.3e and 2.3f. These theoretical radiation patterns are calculated by using the analytically known far-field expansion of the Green's function of a multilayered system, as explained in Ref. [40]. In this type of calculation the substrate is an infinitely extended multilayered system composed of Air-Si_3N_4-SiO_2, thereby ignoring the finite width of the 1D waveguide on SiO_2. In this 2D waveguide geometry, we can perform quantitative scattering calculations of antenna particles excited by waveguide modes that we obtain by solving for the propagation constants and mode fields of guided modes that are bound to the Si_3N_4 waveguide. In this approach, the polarizability of scatterers is taken as the electrodynamically corrected quasi-static polarizability of a prolate spheroid [41]. The dynamical correction used in the calculations for the polarizability is [42]

$$\overline{\alpha}^{-1} = \frac{1}{\overline{\alpha}_{\text{static}}} \overline{I} - Im[\overline{\mathbf{G}}_{\text{interface}}(\mathbf{r}_0, \mathbf{r}_0)].\qquad(2.1)$$

35

Here α_{static} is the static polarizability of a prolate spheroid and $\overline{\mathbf{G}}_{\text{interface}}(\mathbf{r}_0, \mathbf{r}_0)$ is the Green's function of the layered system as found in [43] evaluated at the position of the scatterer $\mathbf{r}_0$. The satisfactory correspondence between the measured radiation patterns for antennas on 1D guides, and the theoretical figures for 2D guides implies that the finite width of 1 μm of the waveguide used does not strongly alter the angular distribution of light scattered out-of-plane. Arguably, close inspection of the data shows that angular emission is narrowed in k_y by the 1D waveguide compared to the 2D system.

2.4 In-coupling by a single dipole antenna

As a complementary experiment on the antenna-waveguide system, we have also performed the reverse, *i.e.*, excitation from the far field and detection through the waveguide (see Fig. 2.1b). In this experiment a diffraction limited focused spot is scanned over the antenna and the light in-coupled into the 1500 nm wide waveguide is acquired through the aligned optical fibers at the waveguide end facets. The inset of Fig. 2.5 shows a plot of the maximum in-coupled intensity for different positions of the scanned beam. The 2D grayscale plot, which could be viewed as a confocal raster scanning graph, barring the fact that collection is through the waveguide, and not through any objective, indicates that the light is being coupled into the waveguide from a point that is approximately equal in size, or less, than the diffraction limit. By calibration of the spot to a white light image of the fabrication markers, we ensured that the center of the maximum in-coupled intensity coincides strictly with the antenna position. At each position we furthermore collect spectral information, as the incident beam has a broad spectrum and the detected light is coupled into the spectrometer. Fig. 2.5 shows the spectrum at the location of maximum in-coupling determined from the 2D spatial raster scan. We find a maximum coupling from free space into the waveguide at a wavelength around 750 nm across a bandwidth of 65 nm (FWHM). The excellent correspondence of the in-coupling resonance frequency with the scattering resonance we observe when illuminating through the waveguide, indicates that resonant in-coupling into the waveguide occurs at the same wavelength as scattering of the waveguide mode by the antenna out of the waveguide. Also, the bandwidth agrees reasonably well with the measured bandwidth in the out-coupling experiment. However, the spectrum in the in-coupling experiment has a tail towards the near infrared wavelengths due to the red shifted cutoff frequency of the 1500 nm wide waveguides compared to the 1000 nm wide waveguides used to obtain Fig. 2.3.

We now attempt to estimate the in-coupling efficiency of light into the waveguide from the data measured in Fig. 2.5. In this experiment coupling from the waveguide to the spectrometer used a metallized tapered fiber tip at the waveguide end facets, in order to reduce stray light contributions such as grazing light coupled to the SiO_2 substrate. Unfortunately, the use of this metallic tip makes it difficult to find a quantitative coupling efficiency of antenna to waveguide, as the waveguide-to-fiber efficiency is imprecisely known. On basis of in-coupling intensity data of 10 kcts/s at 750 nm, knowing that
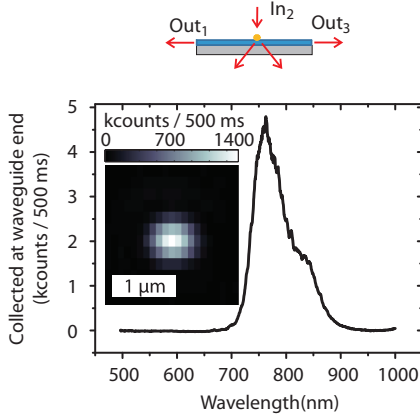
Figure 2.5: Top: sketch of the experimental geometry. We excite the antenna from the air side and measure how much light is coupled into the waveguide. Bottom: spectrum of the light collected at the waveguide end facets, *i.e.*, of the light coupled into the waveguide upon excitation of the scatterer. A clear plasmon resonance is observed. In the inset we show a confocal raster scanning graph of in-coupled intensity for different positions of the focused spot.

the irradiance factor for our spectrometer is 12.86 (kcts/s)/(μW/cm^2/ nm) at 750 nm, we can calculate an in-coupled irradiance of 0.77 μW/(cm^2·nm) in the spectrometer; when using a free space focused beam with an irradiance of $1.56 \times 10^8 \mu$W/(cm^2·nm), an estimated fiber collection efficiency of 10^{-4}, an efficiency in the single mode to multi mode fiber coupling of 10%, and a loss in the waveguide of 10^{-2}. With this data we estimate in-coupling efficiencies on the order of 1%, for diffraction limited in-coupling beams. Unfortunately, the experimental uncertainties especially regarding the in-coupling of the signal into the detection fibers, imply that our experimental estimate is not more accurate than approximately one order of magnitude. To obtain an independent, and possibly more precise estimate, we turn to theory.

We use the model of a dipolar scatterer on top of a 2D waveguide as explained before. We find the efficiency with which such a scatterer couples light into the waveguide in two steps. First, we find the extinct power, *i.e.*, the power that is removed from a plane wave incident from the air due to the presence of the scatterer. The extinct power is defined as

$$P_{ext} = \frac{\omega}{2} Im(\mathbf{p} \cdot \mathbf{E}_o^*). \tag{2.2}$$

Furthermore, the power that the induced dipole moment radiates into the far field *barring* the waveguide mode can be calculated from the dyadic Green's function far field expansion that can be found in Ref. [40]. The difference in extinct power and far field radiated power equals the power coupled into the waveguide, plus the power absorbed by the particle due to losses. We find (assuming a plane wave excitation) that the coupling efficiency strongly depends on the height of the single rod antenna with respect to the waveguide as shown in Fig. 2.6 (green curve). This dependence reflects

the strong spatial dependence of both the guided mode contribution, and radiative mode contribution to the local density of states of stratified waveguide systems. We predict a maximum incoupling+absorption of ~48% for particle heights 30 nm from the waveguide. This in-coupling decays exponentially with distance from the waveguide and stabilizes at 30% at distances around 2 μm from the waveguide. Since significant in-coupling is not expected for such large distances we estimate that those 30% correspond to absorption in the particle. Taking that as a measure for absorption, we conclude that a particle just above the waveguide will couple approximately 20% of the light that it harvests from the input beam into the waveguide. The remaining 80% is split between far field (50% of extinct power) and absorption (30% of extinct power). It is important to notice that these numbers indicate the efficiencies with which the power is distributed in the different radiation channels relative to the total power that couples to the dipolar scatterer. To convert these relative efficiencies to actual cross sections, one needs to determine what the absolute extinction cross section of the particle is. The overall extinction cross section is anticipated to be at most 0.16 μm^2, *i.e.*, 1.2 times smaller than the diffraction limit, as calculated from full wave simulations. To conclude, a single particle illuminated by a diffraction limited beam can couple approximately 20% of the incident energy into the waveguide, in accord with the crude measured estimate.
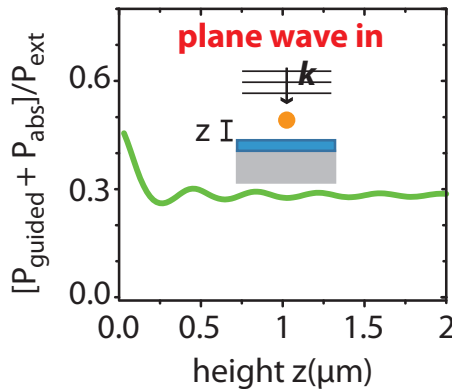
Figure 2.6: Results of a calculation where a plane wave is sent towards the antenna from the air side and the efficiency of absorption plus scattering into the waveguide mode is reported. The axis show the ratio between guided plus absorbed power to extinction power for plane wave excitation of the antenna found for a single rod antenna element at different 'z' distances from the waveguide at 755 nm.

The constraint of fairly large absorption (30%), which in our system is due both to the gold and to the underlying Cr adhesive layer, can be mitigated by shifting the operation range further to the NIR using larger particles, or by swapping Au for silver. In this case a protective dielectric could be required to avoid particle degradation. Such capping is expected to also be beneficial optically, as it would pull the waveguide mode up towards the particle, thereby likely enhancing the coupling efficiency.

2.5   Conclusions

To conclude, we have fabricated plasmonic antennas precisely aligned to dielectric waveguides, and quantified their properties for applications in waveguide-integrated plasmonics. We found that single rod antennas scatter light as electric dipoles on top of a multi-layer system. As a first step, we have quantified how single plasmonic antennas couple to waveguide modes, in particular quantifying how strongly, and into which directions, antennas out-couple waveguide modes. Conversely, we have argued that a single plasmon antenna can already couple up to 20% of a diffraction limited input beam into the waveguide mode. These electric dipolar scatterers coupled to dielectric waveguides can therefore be used as couplers of light from localized sources to waveguide modes, or as phase controlled scatterers that can be addressed through individual waveguides. Finally the understanding of these antennas and how we can treat them analytically as electric dipole scatterers opens a way to design multielement antennas in an analytical fashion without resorting to full wave simulations.

References

[1] W. L. Barnes, A. Dereux, and T. W. Ebbesen, *Surface plasmon subwavelength optics*, Nature **424**, 824 (2003).

[2] L. Novotny and N. van Hulst, *Antennas for light*, Nat. Photon. **5**, 83 (2011).

[3] A. Aubry, D. Y. Lei, A. I. Fernandez-Domínguez, Y. Sonnefraud, S. A. Maier, and J. B. Pendry, *Plasmonic light-harvesting devices over the whole visible spectrum*, Nano Lett. **10**, 2574 (2010).

[4] J. A. Schuller, E. S. Barnard, W. Cai, Y. C. Jun, J. S. White, and M. L. Brongersma, *Plasmonics for extreme light concentration and manipulation*, Nat. Mater. **9**, 193 (2010).

[5] A. V. Akimov, A. Mukherjee, C. L. Yu, D. E. Chang, A. S. Zibrov, P. R. Hemmer, H. Park, and M. D. Lukin, *Generation of single optical plasmons in metallic nanowires coupled to quantum dots*, Nature **450**, 402 (2007).

[6] A. G. Curto, G. Volpe, T. H. Taminiau, M. P. Kreuzer, R. Quidant, and N. F. van Hulst, *Unidirectional emission of a quantum dot coupled to a nanoantenna*, Science **329**, 930 (2010).

[7] T. H. Taminiau, F. D. Stefani, F. B. Segerink, and N. F. van Hulst, *Optical antennas direct single-molecule emission*, Nat. Photonics **2**, 234 (2008).

[8] S. Schietinger, M. Barth, T. Aichele, and O. Benson, *Plasmon-enhanced single photon emission from a nanoassembled metal-diamond hybrid structure at room temperature*, Nano Lett. **9**, 1694 (2009).

[9] A. L. Falk, F. H. L. Koppens, C. L. Yu, K. Kang, N. de Leon Snapp, A. V. Akimov, M.-H. Jo, M. D. Lukin, and H. Park, *Near-field electrical detection of optical plasmons and single-plasmon sources*, Nat. Phys. **5**, 475 (2009).

[10] R. Carminati, J.-J. Greffet, C. Henkel, and J. Vigoureux, *Radiative and non-radiative decay of a single molecule close to a metallic nanoparticle*, Opt. Commun. **261**, 368 (2006).

[11] R. M. Bakker, H.-K. Yuan, Z. Liu, V. P. Drachev, A. V. Kildishev, V. M. Shalaev, R. H. Pedersen, S. Gresillon, and A. Boltasseva, *Enhanced localized fluorescence in plasmonic nanoantennae*, Appl. Phys. Lett. **92**, 043101 (2008).

[12] P. Bolger, W. Dickson, A. Krasavin, L. Liebscher, S. Hickey, D. Skryabin, and A. Zayats, *Amplified spontaneous emission of surface plasmon polaritons and limitations on the increase of their propagation length*, Opt. Lett. **35**, 1197 (2010).

[13] L. Rogobete, F. Kaminski, M. Agio, and V. Sandoghdar, *Design of plasmonic nanoantennae for enhancing spontaneous emission*, Opt. Lett. **32**, 1623 (2007).

[14] X.-W. Chen, V. Sandoghdar, and M. Agio, *Highly efficient interfacing of guided plasmons and photons in nanowires*, Nano Lett. **9**, 3756 (2009).

[15] A. F. Koenderink, *Plasmon nanoparticle array waveguides for single photon and single plasmon sources*, Nano Lett. **9**, 4228 (2009).

[16] M. Pfeiffer, K. Lindfors, C. Wolpert, P. Atkinson, M. Benyoucef, A. Rastelli, O. G. Schmidt, H. Giessen, and M. Lippitz, *Enhancing the optical excitation efficiency of a single self-assembled quantum dot with a plasmonic nanoantenna*, Nano Lett. **10**, 4555 (2010).

[17] L. Billot, M. L. de la Chapelle, A.-S. Grimault, A. Vial, D. Barchiesi, J.-L. Bijeon, P.-M. Adam, and P. Royer, *Surface enhanced raman scattering on gold nanowire arrays: Evidence of strong multipolar surface plasmon resonance enhancement*, Chem. Phys. Lett. **422**, 303 (2006).

[18] C. E. Talley, J. B. Jackson, C. Oubre, N. K. Grady, C. W. Hollars, S. M. Lane, T. R. Huser, P. Nordlander, and N. J. Halas, *Surface-enhanced raman scattering from individual au nanoparticles and nanoparticle dimer substrates*, Nano Lett. **5**, 1569 (2005).

[19] F. Le, D. W. Brandl, Y. A. Urzhumov, H. Wang, J. Kundu, N. J. Halas, J. Aizpurua, and P. Nordlander, *Metallic nanoparticle arrays: A common substrate for both surface-enhanced raman scattering and surface-enhanced infrared absorption*, ACS Nano **2**, 707 (2008).

[20] J. Ye, L. Lagae, G. Maes, G. Borghs, and P. V. Dorpe, *Symmetry breaking induced optical properties of gold open shell nanostructures*, Opt. Express **17**, 23765 (2009).

[21] T. R. Jensen, R. P. V. Duyne, S. A. Johnson, and V. A. Maroni, *Surface-enhanced infrared spectroscopy: A comparison of metal island films with discrete and nondiscrete surface plasmons*, Appl. Spectrosc. **54**, 371 (2000).

[22] J. Kundu, F. Le, P. Nordlander, and N. J. Halas, *Surface enhanced infrared absorption (seira) spectroscopy on nanoshell aggregate substrates*, Chem. Phys. Lett. **452**, 115 (2008).

[23] K. Nakata, Y. Kayama, K. Shimazu, A. Yamakata, S. Ye, and M. Osawa, *Surface-enhanced infrared absorption spectroscopic studies of adsorbed nitrate, nitric oxide, and related compounds 2: Nitrate ion adsorption at a platinum electrode*, Langmuir **24**, 4358 (2008).

[24] N. Liu, M. Mesch, T. Weiss, M. Hentschel, and H. Giessen, *Infrared perfect absorber and its application as plasmonic sensor*, Nano Lett. **10**, 2342 (2010).

[25] H. Aouani, O. Mahboub, N. Bonod, E. Devaux, E. Popov, H. Rigneault, T. W. Ebbesen, and J. Wenger, *Bright unidirectional fluorescence emission of molecules in a nanoaperture with plasmonic corrugations*, Nano Lett. **11**, 637 (2011).

[26] D. Marcuse, *Theory of Dielectric Optical Waveguides*, Academic Press,Inc., 1974.

[27] M. T. Hill, H. J. S. Dorren, T. de Vries, X. J. M. Leijtens, J. H. den Besten, B. Smalbrugge, Y.-S. Oei, H. Binsma, G.-D. Khoe, and M. K. Smit, *A fast low-power optical memory based on coupled micro-ring lasers*, Nature **432**, 206 (2004).

[28] I. Sersic, C. Tuambilangana, and A. F. Koenderink, *Fourier microscopy of single plasmonic scatterers*, New J. Phys. **13**, 083019 (2011).

[29] N. L. Thomas, R. Houdré, M. V. Kotlyar, D. O'Brien, and T. F. Krauss, *Exploring light propagating in photonic crystals with fourier optics*, J. Opt. Soc. Am. B **24**, 2964 (2007).

[30] A. Drezet, A. Hohenau, D. Koller, A. Stepanov, H. Ditlbacher, B. Steinberger, F. Aussenegg, A. Leitner, and J. Krenn, *Leakage radiation microscopy of surface plasmon polaritons*, Mater. Sci. Eng. B **149**, 220 (2008).

[31] S. Randhawa, M. U. González, J. Renger, S. Enoch, and R. Quidant, *Design and properties of dielectric surface plasmon bragg mirrors*, Opt. Express **18**, 14496 (2010).

[32] Y. Alaverdyan, E.-M. Hempe, A. N. Vamivakas, E. Haibo, S. A. Maier, and M. Atature, *Spectral and angular distribution of rayleigh scattering from plasmon-coupled nanohole chains*, Appl. Phys. Lett. **94**, 021112 (2009).

[33] C. Huang, A. Bouhelier, G. Colas des Francs, A. Bruyant, A. Guenot, E. Finot, J.-C.

Weeber, and A. Dereux, *Gain, detuning, and radiation patterns of nanoparticle optical antennas*, Phys. Rev. B **78**, 155407 (2008).

[34] M. A. Lieb, J. M. Zavislan, and L. Novotny, *Single-molecule orientations determined by direct emission pattern imaging*, J. Opt. Soc. Am. B **21**, 1210 (2004).

[35] D. Patra, I. Gregor, J. Enderlein, and M. Sauer, *Defocused imaging of quantum-dot angular distribution of radiation*, Appl. Phys. Lett. **87**, 101103 (2005).

[36] M. N'Gom, J. Ringnalda, J. F. Mansfield, A. Agarwal, N. Kotov, N. J. Zaluzec, and T. B. Norris, *Single particle plasmon spectroscopy of silver nanowires and gold nanorods*, Nano Lett. **8**, 3200 (2008).

[37] L. S. Slaughter, W.-S. Chang, P. Swanglap, A. Tcherniak, B. P. Khanal, E. R. Zubarev, and S. Link, *Single-particle spectroscopy of gold nanorods beyond the quasi-static limit: Varying the width at constant aspect ratio*, J. Phys. Chem. C **114**, 4934 (2010).

[38] T. Kalkbrenner, U. Håkanson, and V. Sandoghdar, *Tomographic plasmon spectroscopy of a single gold nanoparticle*, Nano Lett. **4**, 2309 (2004).

[39] K. Lindfors, T. Kalkbrenner, P. Stoller, and V. Sandoghdar, *Detection and spectroscopy of gold nanoparticles using supercontinuum white light confocal microscopy*, Phys. Rev. Lett. **93**, 037401 (2004).

[40] L. Novotny and B. Hecht, *Principles of Nano-optics*, Cambridge University Press, Cambridge, 2006.

[41] C. F. Bohren and D. R. Huffmann, *absorption and scattering of light by small particles*, Wiley, New York, 1983.

[42] T. Coenen, E. J. R. Vesseur, A. Polman, and A. F. Koenderink, *Directional emission from plasmonic yagi-uda antennas probed by angle-resolved cathodoluminescence spectroscopy*, Nano Lett. **11**, 3779 (2011).

[43] L. Novotny, *Allowed and forbidden light in near-field optics. I. A single dipolar light source*, J. Opt. Soc. Am. A **14**, 91 (1997).

3

Phased Array Antennas on a Dielectric Waveguide

We use the single plasmonic structures on top of waveguides as pursued in chapter 2 as dipolar building blocks for new types of antennas where the waveguide enhances the coupling between antenna elements. We report on waveguide hybridized Yagi-Uda antennas which show directionality in out-coupling of guided modes. These antennas also show directionality for in-coupling into the waveguide, of localized excitations positioned at the feed element. These measurements together with simulations demonstrate that this system might be useful as a platform for plasmon quantum optics schemes as well as for fluorescence lab-on-chip applications.

3.1   Introduction

In chapter 2 we showed that single rod antennas interact strongly with dielectric waveguides and we showed that this interaction can be modeled as the interaction of electric dipolar scatterers on top of a multilayered waveguiding system. We now turn to the study of phased arrays antennas. These antennas are of particular recent interest, since they are array antennas that consist of well understood individual objects, such as metal nanorods [1] with a strong anisotropic polarizability, which are placed in arrays of carefully engineered geometry [2–5] in order to obtain specific responses depending on driving conditions. For instance, one could think of engineering an array of rod antennas to obtain a system which would create regions with a very strong electric field intensity (hot spots) in the vicinity of the antenna when driven by a plane wave, or antennas that when driven by a localized source could direct the light in one or

more chosen desired directions. The physics of these phased array systems is that electrodynamically retarded interactions set the strength and phase of coupling between elements, such that desired functionality ensues from interference. For instance, Yagi-Uda antennas [3, 4, 6–9] are phased array antennas that provide directionality to locally embedded fluorophores, due to constructive interference of the waves scattered by each antenna element in the forward direction. While all the control variables in terms of building block size and shape, as well as the geometries that optimize interaction have been investigated by many researchers [2–4, 7–11], it is imperative to note that a strongly structured embedding dielectric environment will not only change the single building block response, but also the retarded interactions. Therefore, it is important to first study how single objects scatter when placed on waveguides, and subsequently to explore how array antennas function when placed on waveguides which is the main topic of this chapter. The interaction of sources and scatterers with 2D stratified media and waveguides is a subject that has attracted large interest for many applications in optoelectronics, with as main application area photovoltaics and light-extraction from LEDs. The seminal work by Soller and Hall [12] aimed at quantifying the coupling efficiency of scatterers to layered media now acquires new significance for plasmon enhanced solar cells [13, 14]. In the framework of integrated optics, many groups have studied the interaction of 1D and 2D periodic lattices of plasmon strips [15], single plasmon strips and particles [16, 17] with 1D and 2D waveguide modes. In this work we are particularly interested in 1D waveguides coupled to antennas that are subwavelength phased array antennas, as opposed to extended diffractive structures. A recent experimental study of plasmon particle arrays coupled to 1D waveguides was reported by Février et al. [18], who employed near field measurements to show that the modes of arrays of gold scatterers coupled to silicon waveguides may indeed hybridize with the waveguide mode.
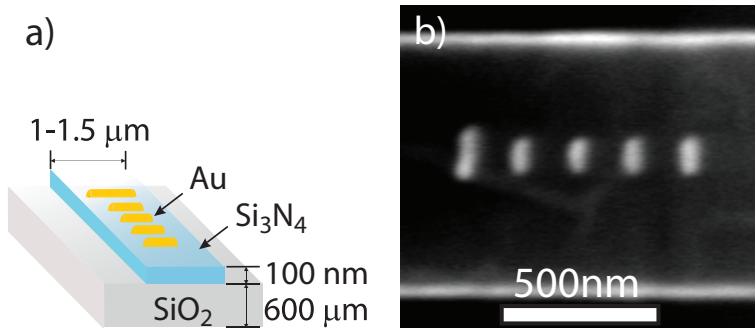
Figure 3.1: In a) and b) we present a schematic view of the sample and substrate used together with a scanning electron micrograph of a typical result of a fabricated Si_3N_4 waveguide with a deposited Yagi-Uda Au antenna.

In this chapter we perform calculations on phased array Yagi-Uda antennas positioned over a 1D Si_3N_4 ridge waveguide on a fused silica substrate, as shown in Fig. 3.1 a. These calculations allow us to determine what is the geometry that best

fits the requirements for strong coupling of light into the waveguide structure. We continue the chapter with measurements on the designed antennas (Fig. 3.1b). These measurements show that we can achieve high contrast efficient unidirectional coupling of localized excitations to the waveguide, which can be controlled by wavelength. These results are highly promising for designing and realizing antennas to control the emission of single emitters.

3.2 Multi-element antennas

For multi-element antennas, we can apply our understanding of the operation of single-element antennas (chapter 2) to improve the absolute in-coupling cross section, albedo, and directivity, similar to the functionality of free space Yagi-Uda antennas [2, 4, 7, 9]. To begin, we start by using the approach of considering small rod antennas as electric dipolar scatterers, so that induced dipole moments $\mathbf{p}$ can be found by using the expression

$$\mathbf{p} = \alpha \mathbf{E}_{\text{total}}(\mathbf{r}'), \tag{3.1}$$

where α is the polarizability tensor that describes the response of the rod antenna (in this case a dynamically corrected prolate spheroid polarizability [19]) and where $\mathbf{E}_{\text{total}}(\mathbf{r}')$ is the total electric field present at position $\mathbf{r}'$. In our problem we need to consider a set of N dipoles positioned on a layered system. An important realization is that if we have a dielectric system that consists of planar waveguides or 1D waveguides, understanding coupled systems is a two step process. Firstly, similar to Eq. (1.20), the induced dipole moments in N particles located at $(\mathbf{r}_1...\mathbf{r}_N)$ will be set by [20]

$$\mathbf{p}_n = \alpha [\mathbf{E}_{\text{in}}(\mathbf{r}_n) + \omega^2 \mu_0 \mu \sum_{m \neq n} \overline{\mathbf{G}}(\mathbf{r}_n, \mathbf{r}_m) \mathbf{p}_m], \tag{3.2}$$

where the driving field $\mathbf{E}_{\text{in}}(\mathbf{r}_n)$ is a solution to the antenna-free problem, such as a waveguide mode, or far field illumination. The Green's function $\overline{\mathbf{G}}(\mathbf{r}_m, \mathbf{r}_n)$ of the waveguide system quantifies the particle interactions as they are mediated through waveguide, substrate, and air cladding layer. Based on chapter 2, we can use the Green's function of a 2D waveguide system as an approximation for the near-field interactions present in 1D waveguide systems, like our ridge waveguide. Therefore in this chapter it is the 2D infinite multi-layer Green's function that we employ to calculate the scattering properties of phased array antennas. The second step in understanding the physics of multi-element antennas is that the near fields, far fields, etcetera, are found by coherent superposition of the single-element properties as [20]

$$\mathbf{E}(\mathbf{r}) = \omega^2 \mu_0 \mu \sum_n \overline{\mathbf{G}}(\mathbf{r}, \mathbf{r}_n) \mathbf{p}_n. \tag{3.3}$$

It is this second step, for which we have quantified properties in chapter 2, that ensures that multi-element antennas can control directivity, albedo, *etc.*, just as for antennas in free space [2, 4, 7, 9]. The linear superposition principle will, for instance, imply that the radiation pattern into free space and waveguide of a multi-element antenna equals

that of a single-element antenna (form factor) *multiplied* with a structure factor that depends on where the different elements are placed. As a consequence, light can never be redirected into directions into which the single elements do not radiate, but light can be significantly redistributed through interference between the different channels into which the single elements do radiate. Thus, one can for instance seek to obtain enhanced radiation into the waveguide and suppression of radiation into substrate and air, through destructive interference.

Given that plasmon particles couple strongly to each other both directly and through coupling mediated by the waveguide one can design multi-element antennas with different final purposes. One design goal is to achieve antennas that maximize the coupling of incident plane waves into the waveguide. Another design goal is to achieve an antenna which maximally couples energy from a single dipolar emitter into the guided mode. The latter would essentially constitute a waveguide-coupled plasmon Yagi-Uda antenna. Here we consider both design goals. First we focus on optimum structures for coupling plane wave excitation incident from the air side into the waveguide using the dipolar antenna building block at fixed height. The point of this example is not to design a structure that replaces conventional end-fire in-coupling, as mode matching to waveguide end facets evidently always has the best potential for in-coupling. Rather, we aim to show how our toolbox can be used to design antennas with an ultra-small footprint (below 1 μm length) that harvest light from out-of-plane directions very well. Such a scenario could be relevant for, *e.g.*, detectors, or future applications in which vertical optical interconnects are desired on multi-layer optoelectronic devices [21]. As optimization parameter, we scan the distance between elements and evaluate the coupling, as shown in Fig. 3.2c. On the x-axis we plot the distance between elements in units of the guided mode wavelength $\lambda_{\text{waveguide}}$ at 755 nm. We find maximum in-coupling at distances which are n times $\lambda_{\text{waveguide}}$ (with n an integer) and minimum when the distance is $(n + 1/2)$ times $\lambda_{\text{waveguide}}$. Since the scatterers are driven in-phase, the arrangement essentially reflects that just a few particles already result in the well-known effect of a grating coupler, that can boost in-coupling by a factor ~2 to 3 compared to a single rod antenna positioned 30 nm from the substrate (see Fig. 2.6).

As a second example, more appropriate for extending plasmon quantum optics to waveguide integrated systems, we consider the scenario of a waveguide coupled Yagi-Uda antenna. An example of this type of antenna is presented in Fig. 3.1a and b where we see that a Yagi Uda antenna is commonly an array antenna with a feed element, a reflector element and director elements that provide directional emission of the field applied to the feed element. Here, the design goal is to couple the radiation of a single dipolar emitter, such as a localized molecule, quantum dot or diamond NV center selectively and unidirectionally to a single waveguide mode using an array of scatterers. The design goal is hence for the radiation of antenna elements and dipole to add up destructively everywhere, except in the waveguide. In this case, a dipolar emitter is located 30 nm above the first element of the antenna. This emitter generates the driving field $\mathbf{E}_{\text{in}}(\mathbf{r}_n)$ over the n elements of the antenna. With this field we calculate the induced dipolar moments of the antenna elements which subsequently are used to find
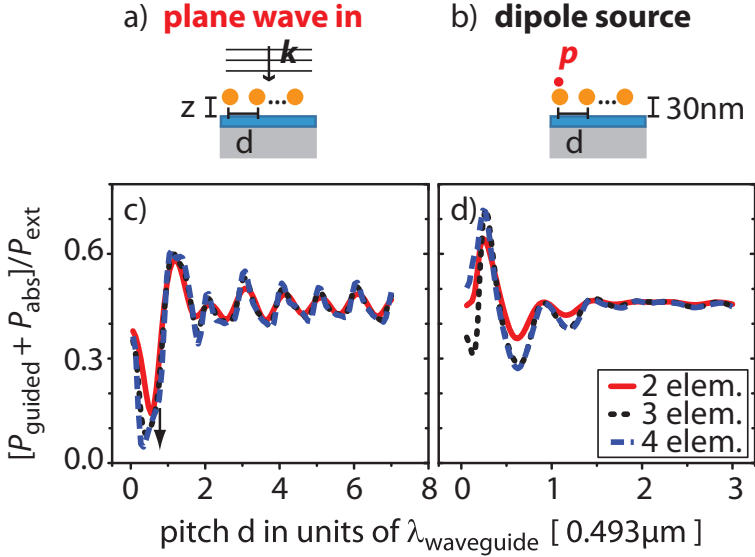
Figure 3.2: a) Presents a sketch of the calculations shown in panel c). In these calculations a plane wave is sent towards the antenna from the air side and the efficiency of absorption plus scattering into the waveguide mode is calculated. c) ratio between guided plus absorbed power to extinction power for plane wave excitation of the antenna. Using a height of 30 nm multi-element antennas (2, 3 and 4 elements) are investigated for different distances 'd' between elements composed of 100 nm Au rod antennas. b) Presents a sketch of the calculations shown in panel d) where an emitter is positioned 30 nm above the first element of an antenna to calculate the absorption efficiency plus emission efficiency of the antenna into the guided mode. This ratio of in-coupled and absorbed light to extinct power is presented for multi-element antennas (2, 3 and 4 elements) as a function of the distance between the elements when the antenna is being excited with the dipolar emitter located above the first element of the array. Horizontal axes are in units of $2\pi/\beta = 0.493$ μm which is the wavelength of the guided mode at 755 nm.

the scattered field, as explained earlier. In Fig. 3.2d we plot the incoupling+absorption rate, as a function of the distance between the directors in the antenna array. As in Fig. 3.2c we plot distance in units of the waveguide mode propagation wavelength. A maximum in-coupling is found for a range of separation distances centered around $\sim \lambda_{\mathrm{waveguide}}/4$ at 755 nm and ranging from $\sim$0.1 to $\sim$0.45 $\lambda_{\mathrm{waveguide}}$. This range is commensurate with the standard rule of thumb for free space Yagi-Uda antennas, that the spacing needs to be around $\lambda/3$, and below $\lambda/2$ to avoid multiple lobes. However, in this case the criterion uses the wavelength of the waveguide mode. The optimum design hence depends on the dispersion of the waveguide. As regards in-coupling efficiencies, this calculation predicts that less than 20% of the emission is directed out-of-plane into either air or substrate. At the same time, 80% of the emission that is captured by the waveguide will be directed in a narrow forward lobe, with an angular distribution in a half angle cone of 37° inside the assumed 2D Si_3N_4 layer. We note

that Yagi-Uda antennas realized so far have been essentially free-space designs placed for practical reasons on air/glass interfaces [2–4]. In this scenario, a directional beam results, that is however completely directed into the glass, along the critical angle for the air-glass interface [9]. The utility of this form of directionality for on-chip applications is very limited, as the directional beam is directed out-of-plane. Here we show that this limitation can be overcome by placing the Yagi-Uda concept into, or on a waveguiding dielectric structure. Our calculation shows that even moderate waveguide confinement strongly influences the directionality to be entirely in-plane and into the guided mode. Thereby, the Yagi-Uda-waveguide combination could be a promising route to plasmon quantum optics. As opposed to, *e.g.*, the plasmonic nanowire paradigm [22–24] that foresees quantum optics in networks in which the excitation remains in dark plasmons throughout, here the utility would be that photons experience entirely lossless transport through established dielectric technology, and conversion to plasmons for light-matter interaction is localized to the sites where it is needed.

3.3 Measurements of waveguide excited multi-element antennas

Based on the design presented in Sec. 3.2 Yagi-Uda antennas were fabricated following the procedure explained in Sec. 2.2. A typical example of a fabricated antenna and the waveguide structure is presented in Fig. 3.1a and b. The antennas were fabricated on top of 100 nm thick and 1000 nm wide Si_3N_4 waveguides on a fused silica substrate, and are composed of 5 rod shaped elements, 3 directors, 1 feed element and 1 reflector, with lengths of 115 nm 120 nm and 180 nm, respectively. The width of the elements is 65 nm and the total length of the antenna is ~790 nm. The measured center-to-center distances between the elements are 170 nm between reflector and feed element, and 183 nm between all other neighboring plasmonic rods. This periodicity of 183 nm or $0.32 \cdot \lambda_{\text{waveguide}}$ at the antenna strongest response wavelength (vacuum wavelength 830 nm) falls well in the range predicted to provide directional behavior according to the theory of the previous section (Fig. 3.2d). We investigated the Yagi-Uda antennas using the same methodology applied to the single-object nano-antennas in chapter 2. The measurements are shown in Fig. 3.3. Transmission measurements indicate that this antenna strongly scatters light from the guided mode, since up to 90% of the light is being scattered out of the waveguide due to the presence of the antenna (Fig. 3.3a (black curve)). The spectrum of the guided mode scattering into the air side of the sample shows a resonance at a wavelength of 830 nm, as shown in Fig. 3.3a (red curve). This resonance is significantly red-shifted compared to the resonance of single plasmon particles in Fig. 2.3. In part this shift is due to the fact that the antenna elements are slightly longer than the 100 nm rods, causing a red-shift of the resonance in each particle. In another part, this shift is due to the fact that the antenna response of Yagi Uda antennas is red shifted by plasmon hybridization [25], as reported already by [7, 8]. Quite unlike the case of a single rod antenna, the spectrum strongly depends
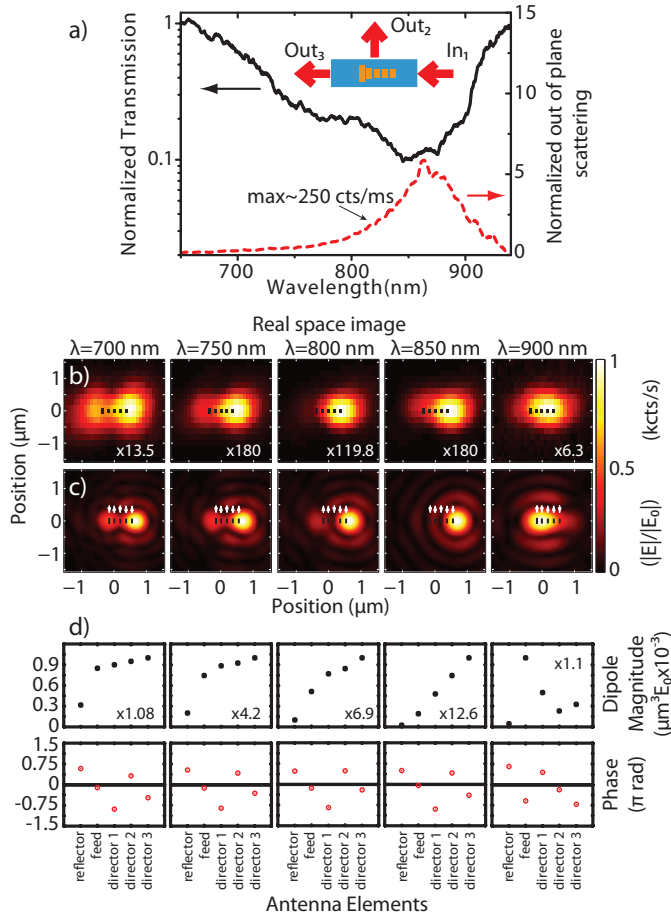
Figure 3.3: Measurements of the scattering of the guided mode to free space modes carried out on a Yagi-Uda antenna on top of a 1000 nm width waveguide. a) Normalized transmission spectra and normalized scattering spectrum into the free space of the guided mode by the antenna. b) Confocal scans over the sample plane of the scattering due to the antenna. As sketched in the cartoon the reflector is located at the left side of the image and the directors are located at the right side. The beam is incident from the right side through channel 1 and the scattering out-of-plane is measured in the air side through channel 2. The graphs in b) show different frequencies measured when focusing at different positions in the sample plane. Panel c) shows the calculated image generated by an array of dipoles with the polarizability of a prolate spheroid and the dimensions of the elements of the Yagi-Uda antenna. This image is calculated from the far fields generated by the scattering of the dipoles using the amplitude and vector microscope point spread function of confocal microscopy. Finally, panel d) shows the magnitude and phase of each dipole moment along the antenna array. The magnitudes and phases are presented for different wavelengths namely 700 nm, 750 nm, 800 nm, 850 nm and 900 nm.

on the part of the antenna from which the light is detected by our imaging system (see Fig. 3.3b). In fact in a spectrally resolved raster scan of the antenna one can visualize two clearly distinct zones which change relative intensity depending on the wavelength. For $\lambda = 700$ nm both zones show strong scattering of the waveguide mode, while the front zone decreases its intensity when shifting λ to the red. At 900 nm wavelength we observe that the antenna scatters light from the entire area of the antenna. Naively one might assume that a confocal scan reports an image of the local field intensity $|E|^2$ at the antenna, blurred by the diffraction limit. In this view, the appearance of distinct bright zones at different wavelengths would indicate spatial localization of induced dipole moments $|p|^2$ along the chain, similar to the report by de Waele *et al.* [8]. In reality, more information is hidden in our data, since image formation is a coherent process that actually results from interference of radiation from all the dipoles in the sample plane on the confocal pinhole. Thus, phase information is also hidden in the confocal images, and the collected spatial distribution should not be interpreted simply as a map of $|p|^2$ with Gaussian blurring due to the diffraction limit. We have performed calculations, shown in Fig. 3.3c and d, that include the interference in the image formation process using the amplitude and vector microscope point spread function of confocal microscopy [20], similar to the calculations used to support the measurement of wavelength-tunable localization of dipole excitations on plasmon chains in index-matched environments reported in Ref. [8]. Our calculations confirm that simply changing the input wavelength strongly changes both the spatial distribution of induced dipole strengths, as well as the distribution of phases excited along the array. For instance, having all elements in phase results in the antenna appearing as a bright entity in the confocal scan (Fig. 3.3b, 900 nm wavelength). Conversely, for wavelengths where the antenna lights up as two distinct regions (Fig. 3.3b, $\lambda < 800$ nm), a 180° phase jump occurs in the induced dipole moments along the length of the plasmon chain. To conclude, the spatial maps prove that the Yagi-Uda antenna indeed acts as a phased array, driven coherently by the waveguide mode.

The spatial mapping shows that, depending on excitation wavelength, the amplitude and phase of the dipole excitations on the particle chain is strongly varying. It is exactly this physics that gives rise to the interference that makes a Yagi-Uda antenna directional. An excellent way to assess the coupling between antenna particles is to map radiation patterns for different driving conditions. We measure the radiation patterns on the air side using Fourier imaging. We select distinct wavelength slices using 40 nm bandwidth band pass filters placed in front of the CCD camera. The scattering into the air side shows strong directionality with a distinct wavelength dependence (Fig. 3.4). From these measurements we see that Yagi-Uda antennas, when placed over a waveguide system, continue presenting directionality in their scattering. At 850 nm close to the scattering resonance the scattering in the forward direction is maximum. Far from resonance at 700 nm the backward directed scattering and the forward directed scattering have the same intensity. The scattered light is highly polarized in the direction parallel to the antenna elements, with polarization ratio > 1:9. In conclusion, Yagi-Uda antennas on top of waveguides allow spectrally controllable directional out-coupling of waveguide modes, as well as wavelength and excitation direction dependent control
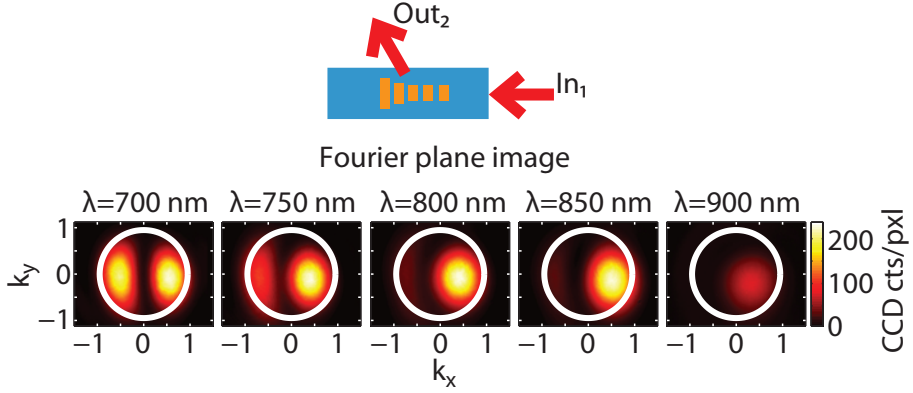
Figure 3.4: Measurements of the scattering of the guided mode to free space modes carried out on a Yagi-Uda antenna on top of a 1000 nm width waveguide. In the panels we show Fourier images of the Yagi-Uda antenna for the scattered light coming from the guided modes. The images are acquired with a CCD camera and the different ranges of wavelength are selected using bandpass filters with 40 nm FWHM. These graphs show that the antenna on the substrate has directionality in its scattering. (The integration times are: for 700 nm 9.64 s, for 750 nm 3.09 s for 800 nm 1.45 s, for 850 nm 6.6 s and for 900 nm 30 s.)

of amplitude and phase along the length of the antenna, very similar to observations recently made in scattering experiments [7, 8]. Such tunable radiation patterns upon local driving, and reciprocally tunable response upon far field driving can be viewed as a poor mans version of coherent control, where the phase and amplitude of fs pulses serve to optimize hot spots or directionality [26–28]. We envision that the localization and directionality could be further optimized in future experiments by using ultrafast fs waveguide excitation and pulse shaping strategies [29]. As a possible application one can envision the use of this platform of waveguide-addressable spatially tunable hot spots for, for instance spatially cross correlated spectroscopies, such as fluorescence correlation spectroscopy [30].

3.4 In-coupling by a Yagi-Uda antenna

As a final aspect of our experiment, we report on the in-coupling into the waveguide mode of a 1500 nm waveguide that can be achieved by raster scanning a focused spot over the antenna. Our theory has shown that for in-coupling of plane waves a multiple of $\lambda_{\text{waveguide}}$ spacing is optimal so that a grating coupling effect aids in-coupling. The Yagi-Uda antenna that we explore in this work is evidently not an ideal structure for in-coupling plane waves, owing to its much smaller periodicity. Indeed, Yagi-Uda antennas are designed for in-coupling *localized* excitations rather than plane waves. For diffraction limited illumination of just a few antenna elements one might approximate such localized excitation by almost achieving a situation in which just one element
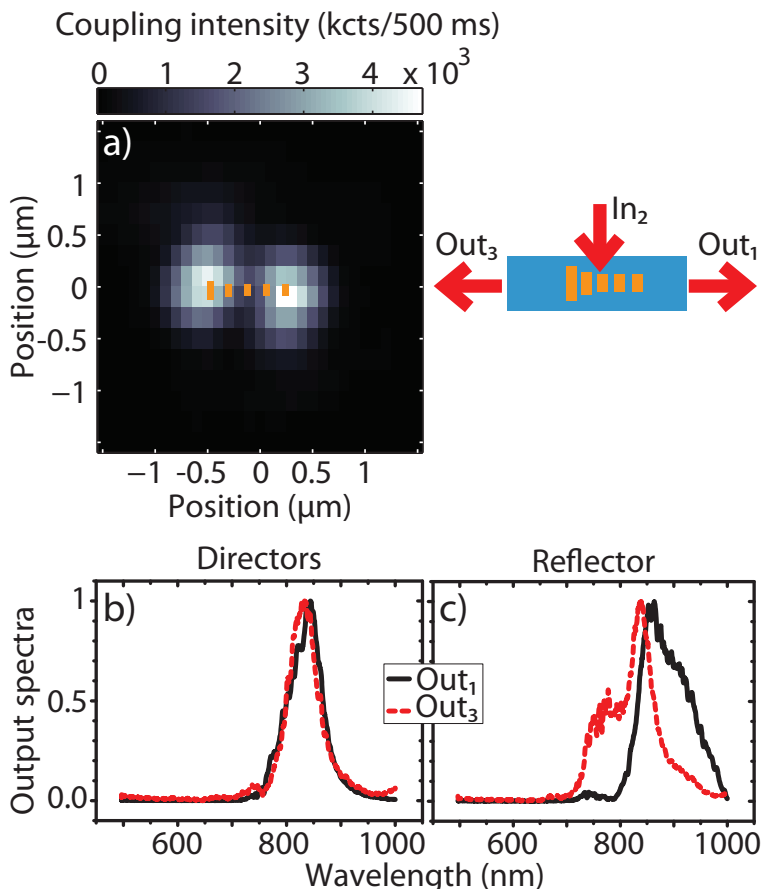
Figure 3.5: a) Confocal image of the waveguide obtained by scanning a focused spot over the Yagi-Uda antenna on top of a 1500 nm width waveguide and collecting spectra of light coupled into the waveguide at the waveguide end facet. The map is created by plotting the integrated count rate of the spectra taken at each position of the sample. b) and c) spectra acquired from the positions of maximum in-coupling located at the directors and reflector side of the antenna, when measured through channel 1 and channel 3, as depicted in the top right sketch of the experiment. These graphs show the different spectral behaviour of the different parts of the antenna, namely, when exciting the directors the same spectra emerge from both waveguide ends. In contrast when locally exciting the reflector and feed element the spectra coupled into both forward and backward guided mode are highly different. The observations show high-contrast unidirectional coupling into the waveguides that can be reversed by sweeping wavelength.

of the antenna is excited. Excitation of just the plasmonic feed element by a focused beam can thereby be used as an experimental probe of antenna directivity that mimics localized excitation by a molecule in a scattered signal, as realized by Kosako and

Hoffman for antennas on an air-glass interface [4]. Therefore, we record scattering into the forward and backward waveguide direction as a function of where we illuminate the antenna with a tight focus. As in scattering, two distinct zones of high in-coupling are found when we collect signal in both waveguide branches, and integrate over the full white light spectrum. Using spectrally resolved detection we assess whether these two zones of efficient in-coupling, one of which is at the feed element of the antenna, and the other of which is at the directors, are associated with the same or with different spectral features in the light that is coupled into both waveguide ends. In Fig. 3.5b we plot the spectrum that is collected at both the forward, and the backward waveguide end when we excite the directors of the antenna. When the excitation spot is focused on the directors, and therefore the directors are excited in phase, almost identical spectra emerge from both waveguide ends. In stark contrast, when the excitation spot is focused on the reflector side of the antenna, *i.e.*, largely on the feed element, generating a phase gradient over the directors, the spectra that emerge at the two waveguide ends are very different from each other. At the end facet corresponding to the backward direction (reflector side of the antenna) we obtain a spectrum that is significantly blue shifted from the spectrum retrieved at the the forward direction end facet. The steep gradient in the spectra around 830 nm imply that it is possible to completely reverse the direction of the in-coupled beam that is launched into the waveguide with a very high contrast, simply by a small change in excitation wavelength. This behavior is reciprocal to the strongly dependent receiver response of antenna arrays, that is expected to swap directionality as the excitation wavelength is swept through cutoff, a phenomenon first reported for plasmonic antennas in experiments by de Waele *et al.* [8]. When examining the in-coupling count rates in Fig. 3.5a for the Yagi-Uda antenna we see that the in-coupling for the Yagi-Uda is around three times more efficient than for the single element antenna.

3.5   Conclusions

To conclude, we have built on the results from chapter 2 to design plasmonic phased array antennas. Using the knowledge gained of the response of single element antennas on top of a waveguide, we have demonstrated how one can use the single dipole antenna as building block of a rational design strategy for multi-element antennas that derive functionality from a phased-array coherent response to driving by the waveguide mode. In particular, we have demonstrated that waveguide-coupled Yagi-Uda antennas provide a platform for waveguide addressable spatially tunable hot spots, that can for instance be used as programmable hot spots of pump light for spatially cross correlated spectroscopies. Conversely, the antennas can provide strong directionality, notably allowing to couple a local driving field unidirectionally into the waveguide. While our experimental demonstration of this unidirectional coupling used an external laser scattered off the antenna, our calculations show that this functionality will directly extend to fluorophores. Thereby, waveguide-hybridized plasmon array antennas are a highly promising platform for many applications. For instance, one can efficiently

collect all the fluorescence of single fluorophores directly through a waveguide. The combination with the programmable hot spots of pump light that can be generated, makes this platform highly attractive for making optofluidic lab-on-chip devices that have entirely on chip integration of driving and readout for advanced fluorescence assays at single molecule levels. Also, we envision that hybrid systems of plasmon antennas and dielectric waveguides may outperform proposed plasmon quantum optics schemes [23, 24]. While plasmonics offer very high light-matter interaction strength for coupling to localized emitters that act as qubits, the structures with the highest interaction strength are usually least suited as waveguides for transport, as losses are high. We propose that the combination of antennas and dielectric waveguides allows one to combine low loss transport as photons that are converted back and forth to plasmons only exactly where needed, *i.e.*, at an antenna surrounding an emitter.

References

[1] T. H. Taminiau, R. J. Moerland, F. B. Segerink, L. Kuipers, and N. F. van Hulst, *λ/4 resonance of an optical monopole antenna probed by single molecule fluorescence*, Nano Lett. **7**, 28 (2007).

[2] A. G. Curto, G. Volpe, T. H. Taminiau, M. P. Kreuzer, R. Quidant, and N. F. van Hulst, *Unidirectional emission of a quantum dot coupled to a nanoantenna*, Science **329**, 930 (2010).

[3] H. F. Hofmann, T. Kosako, and Y. Kadoya, *Design parameters for a nano-optical yagi-uda antenna*, New J. Phys. **9**, 217 (2007).

[4] T. Kosako, Y. Kadoya, and H. F. Hofmann, *Directional control of light by a nano-optical yagi-uda antenna*, Nat. Photon. **4**, 312 (2010).

[5] K. Aydin, I. M. Pryce, and H. A. Atwater, *Symmetry breaking and strong coupling in planar optical metamaterials*, Opt. Express **18**, 13407 (2010).

[6] J. Li, A. Salandrino, and N. Engheta, *Optical spectrometer at the nanoscale using optical yagi-uda nanoantennas*, Phys. Rev. B **79**, 195104 (2009).

[7] A. F. Koenderink, *Plasmon nanoparticle array waveguides for single photon and single plasmon sources*, Nano Lett. **9**, 4228 (2009).

[8] R. de Waele, A. F. Koenderink, and A. Polman, *Tunable nanoscale localization of energy on plasmon particle arrays*, Nano Letters **7**, 2004 (2007).

[9] T. H. Taminiau, F. D. Stefani, and N. F. van Hulst, *Enhanced directional excitation and emission of single emitters by a nano-optical yagi-uda antenna*, Opt. Express **16**, 10858 (2008).

[10] P. Offermans, M. C. Schaafsma, S. R. K. Rodriguez, Y. Zhang, M. Crego-Calama, S. H. Brongersma, and J. Gòmez Rivas, *Universal scaling of the figure of merit of plasmonic sensors*, ACS Nano **5**, 5151 (2011).

[11] F. Hao, P. Nordlander, Y. Sonnefraud, P. V. Dorpe, and S. A. Maier, *Tunability of subradiant dipolar and fano-type plasmon resonances in metallic ring/disk cavities: Implications for nanoscale optical sensing*, ACS Nano **3**, 643 (2009).

[12] B. J. Soller and D. G. Hall, *Energy transfer at optical frequencies to silicon-based waveguiding structures*, J. Opt. Soc. Am. A **18**, 2577 (2001).

[13] C. Rockstuhl, S. Fahr, and F. Lederer, *Absorption enhancement in solar cells by localized plasmon polaritons*, Journal of Applied Physics **104**, 123102 (2008).

[14] N. C. Panoiu and J. Richard M. Osgood, *Enhanced optical absorption for photovoltaics* via *excitation of waveguide and plasmon-polariton modes*, Opt. Lett. **32**, 2825 (2007).

[15] A. Christ, S. G. Tikhodeev, N. A. Gippius, J. Kuhl, and H. Giessen, *Waveguide-plasmon polaritons: Strong coupling of photonic and electronic resonances in a metallic photonic crystal slab*, Phys. Rev. Lett. **91**, 183901 (2003).

[16] E. S. Barnard, R. A. Pala, and M. L. Brongersma, *Photocurrent mapping of near-field optical antenna resonances*, Nat Nano **6**, 588 (2011).

[17] R. Quidant, C. Girard, J.-C. Weeber, and A. Dereux, *Tailoring the transmittance of integrated optical waveguides with short metallic nanoparticle chains*, Phys. Rev. B **69**, 085407 (2004).

[18] M. Février, P. Gogol, A. Aassime, R. Mégy, C. Delacour, A. Chelnokov, A. Apuzzo, S. Blaize, J.-M. Lourtioz, and B. Dagens, *Giant coupling effect between metal nanoparticle chain and optical waveguide*, Nano Letters **12**, 1032 (2012).

[19] C. F. Bohren and D. R. Huffmann, *absorption and scattering of light by small particles*, Wiley, New York, 1983.

[20] L. Novotny and B. Hecht, *Principles of Nano-optics*, Cambridge University Press, Cambridge, 2006.

[21] D. A. B. Miller, *Optical interconnects to electronic chips*, Appl. Opt. **49**, F59 (2010).

[22] D. E. Chang, A. S. Sørensen, P. R. Hemmer, and M. D. Lukin, *Quantum optics with surface plasmons*, Phys. Rev. Lett. **97**, 053002 (2006).

[23] A. V. Akimov, A. Mukherjee, C. L. Yu, D. E. Chang, A. S. Zibrov, P. R. Hemmer, H. Park, and M. D. Lukin, *Generation of single optical plasmons in metallic nanowires coupled to quantum dots*, Nature **450**, 402 (2007).

[24] A. L. Falk, F. H. L. Koppens, C. L. Yu, K. Kang, N. de Leon Snapp, A. V. Akimov, M.-H. Jo, M. D. Lukin, and H. Park, *Near-field electrical detection of optical plasmons and single-plasmon sources*, Nat. Phys. **5**, 475 (2009).

[25] E. Prodan, C. Radloff, N. J. Halas, and P. Nordlander, *A hybridization model for the plasmon response of complex nanostructures*, Science **302**, 419 (2003).

[26] T. S. Kao, S. D. Jenkins, J. Ruostekoski, and N. I. Zheludev, *Coherent control of nanoscale light localization in metamaterial: Creating and positioning isolated subwavelength energy hot spots*, Phys. Rev. Lett. **106**, 085501 (2011).

[27] M. I. Stockman, S. V. Faleev, and D. J. Bergman, *Coherent control of femtosecond energy localization in nanosystems*, Phys. Rev. Lett. **88**, 067402 (2002).

[28] X. Ni, N. K. Emani, A. V. Kildishev, A. Boltasseva, and V. M. Shalaev, *Broadband light bending with plasmonic nanoantennas*, Science **335**, 427 (2012).

[29] M. Aeschlimann, M. Bauer, D. Bayer, T. Brixner, F. J. Garcia de Abajo, W. Pfeiffer, M. Rohmer, C. Spindler, and F. Steeb, *Adaptive subwavelength control of nano-optical fields*, Nature **446**, 301 (2007).

[30] H. Aouani, O. Mahboub, N. Bonod, E. Devaux, E. Popov, H. Rigneault, T. W. Ebbesen, and J. Wenger, *Bright unidirectional fluorescence emission of molecules in a nanoaperture with plasmonic corrugations*, Nano Lett. **11**, 637 (2011).

4

Localized Excitation of Antennas on Waveguides

Plasmonic antennas fabricated on dielectric waveguides represent a very interesting option if one desires localized nodes with strong field confinement for spectroscopy or enhanced light-matter interaction that are addressable through on-chip channels with the lossless transmission of dielectric waveguides. In this chapter we show an experimental and theoretical study of the response of phased array antennas fabricated on waveguides to localized excitations. These excitations are created using the highly focused electron beam of an SEM, that can address each one of the antenna constitutive elements individually. These so-called cathodoluminescence experiments map how much light the antenna as a whole emits, given that one drives individual elements with a set driving strength. This total response is a combination of both the coupling between antenna elements, and the polarizability of each element. Our maps indicate a large variation in local response as a consequence of the exact antenna geometry. By calculating the directionality and excitability properties of a large ensemble of Yagi-Uda antennas with small size deviations, intrinsic to the fabrication process, we show that while small intrinsic disorder does not affect the directionality of the antennas, in the near field disorder may strongly affect the excitability of individual elements.

4.1   Introduction

Experiments on plasmonic antennas on waveguides [1–10] have shown that they constitute a possible route to use the capabilities of nano plasmonics in an integrated platform. For instance one could conceive of lab-on-chip applications that use on-chip routing of light in waveguides with plasmonic elements for plasmon-enhanced spectroscopies. This possibility combines the merits of lossless transmission of

dielectric waveguides and the strong field confinement of plasmonic antennas. The combination of these functionalities on a chip promises to bring detection of atto liter analyte volumes as well as control over the transmission of data in waveguides with plasmonic elements with sub micrometer footprint [11]. We have shown in Chapter 3 that Yagi-Uda *phased array* antennas on a waveguide not only scatter guided light directionally *out of the waveguide* but are also able to in-couple light from free space into guided modes directionally when one excites just one or a few elements of the antenna with a narrow focus [2]. This functionality ensues first from the strong coupling of resonant dipolar scatterers to waveguide modes (chapter 2) and second from the constructive interference that radiation from these antenna elements have in the forward direction, created by a properly engineered phased excitation of each antenna element. The experiment in chapter 3 to prove directional in-coupling into the waveguide used raster scanning of a focused spot of white light over the antenna and measuring the intensity of the light coupled to the waveguide with a spectrometer. However, this is really a poor man's version of the ideal experiment, which would be to provide local excitation of single elements by a point source. Curto et. al. [12] showed that this is feasible by lithographic attachment of quantum dots. As a complement to this technique we would like to determine maps with a measure of "excitability" as a function of position on the antenna, i.e., how strongly a point source of given strength excites the antenna depending on its location. A measurement technique that attains this is cathodoluminescence (CL). Although in our original plan we also wanted to measure the directive emission of localized excitations on Yagi-Uda antennas, it turned out that the number of interferences obtained from direct scattering off the chip edges, alignment markers and cathodoluminescence signal not coupled to the waveguide made impossible the identification of directional emission. Therefore, this chapter focuses solely on spatial maps obtained with cathodoluminescence, and not measured directionality.

Fabrication   In this work we set out to study the response of Yagi-Uda antennas fabricated on waveguides to local excitation by a 30 keV electron beam in a cathodoluminescence microscope set up, i.e., in an SEM with optical detection. This technique requires the samples to have a moderately high conductivity to avoid charging, which would decrease spatial accuracy of the electron beam excitation. Since we are interested in antennas placed on top of non-conductive dielectric waveguides, we chose to fabricate the samples on dielectric Si_3N_4 membranes thin enough to avoid charging effects. We fabricate samples in a two step process. First we deposit antennas made of gold on top of unstructured membranes. Next we define waveguides in a second fabrication step. The first step, i.e., definition of antennas was done by an e-beam (Raith) lithographic step using a ZEP resist on a silicon rich Si_3N_4 membrane (100 nm thick. Norcada Inc.), followed by gold evaporation and lift off, see Fig. 4.1a. See Chapter 2 for a full description of this process. After the evaporation a waveguide was defined around the resulting antennas with a Gallium focused ion beam (FIB FEI Helios) (see Fig. 4.1b). One-dimensional waveguides resulted from ion beam milling two rectangular holes of $\sim 5 \, \mu m \times 20 \, \mu m$ at each side of the antenna with a distance

equal to half the width of the waveguide. Subsequently, in order to extract the light coupled to guided modes in the waveguide, two gratings were defined on the front and back side of the waveguide as shown in Fig. 4.1c and d, at distances 6 microns away from the antenna. We fabricated Yagi-Uda antennas composed of five elements. As usual in literature [12], these elements are called the reflector element, the feed element, and in this case 3 directors. Since all antennas we report on had different
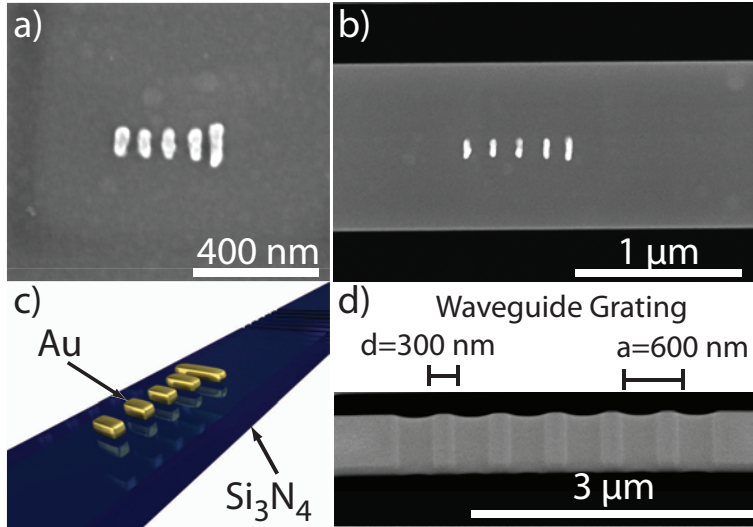
Figure 4.1: Scanning electron microscope images of: a) the smallest Yagi-Uda antenna used (YU1), b) a Yagi-Uda antenna on a bridge waveguide with 1000 nm width (YU4). c) Sketch of a Yagi-Uda antenna on a Si_3N_4 waveguide. The waveguide is terminated with gratings on each end. One of the gratings is shown in fig d). In this case the grating has a pitch of 600 nm and a duty cycle of 50%

dimensions, we list their sizes individually. To begin, antenna YU5 has a reflector size of 150 nm a feed size of 111 nm and directors with length 100 nm. The distance between the reflector and the feed is 170 nm and between the feed and the directors is 208 nm, respectively. The antennas YU4,YU3 and YU2 were designed in such a way that the rod elements as well as the distance between the elements would decrease 10% in between every realization of the antennas. Antennas YU1 and YU4 were designed with the same element size but the distance between the elements in antenna YU1 was decreased by 50% with respect to YU4. The reason to use these different antennas was to see how the size and spacing of elements influence the directional emission and what is the effective tunability that we can have while employing gold for fabricating these nano-antennas. Due to proximity effects changes in the distance between the elements also changed the final sizes of the antenna elements from the designed values. The measured sizes of the fabricated antennas are shown in table 4.1, while SEM pictures of these antennas are shown in Fig. 4.2.

Antenna	Refl.(nm)	Feed(nm)	Dir.(nm)	Refl.to Feed(nm)	Feed to Dir.(nm)	Dir to Dir.(nm)
YU1	126 nm	105 nm	95 nm.	89 nm.	100 nm	99 nm
YU2	93 nm	70 nm	60 nm.	119 nm.	140 nm.	137 nm
YU3	125 nm	100 nm	86 nm.	130 nm.	160 nm.	160 nm
YU4	130 nm	97 nm	84 nm.	158 nm.	183 nm.	183 nm
YU5	150 nm	111 nm	100 nm.	170 nm.	208 nm.	208 nm

Table 4.1: Dimensions used for the fabricated Yagi-Uda antennas.
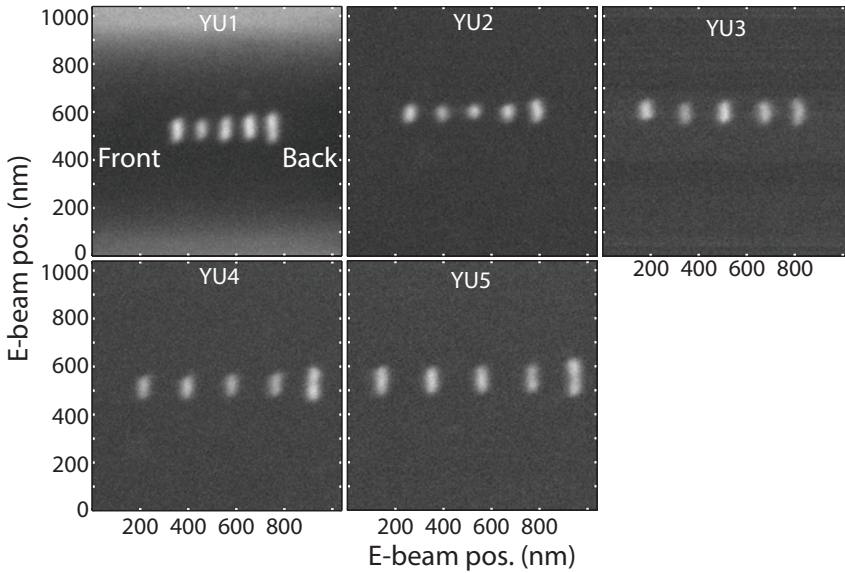
Figure 4.2: Scanning electron microscope images of the different antennas used. Starting from the front side of the antenna as indicated in the figure we find three directors, a feed element and a reflector located at the back of the antenna.

Measurements   We studied the samples in a so-called "cathodoluminescence set-up". Such a set-up essentially consists of a scanning electron microscope in which samples are illuminated by a 30 keV electron beam of 5 nm spot size. Any light that is emitted as a consequence of this irradiation is called "cathodoluminescence". While generally cathodoluminescence might originate from a variety of sources, such as luminescent centers in the material under study, for metallic structures it has been shown [13–17] that the dominant mechanism is that the fast electrons induce plasmons that can subsequently radiate out as light. It is generally accepted that this very localized and sudden excitation causes a spectrally broad response that upon spectral filtering allows one to make high resolution spatial maps. In the set up at AMOLF, this resolution solely derives from the excitation position and not from the detection process, which

uses a parabolic mirror that integrates over a ~25×25 μm area, and over 1.46π sr solid angle. In this work we refer to maps of this excitation-position and wavelength resolved CL intensity as "excitability maps". Since a fast electron is similar to a transient, i.e., very broadband, local current source, this "excitability" is often considered to be proportional to LDOS [18–20]. We refer to Ref. [13, 21] for a detailed account of this technique. As part of the measurement protocol it is important to note that we normalize the signal acquired with the spectrometer CCD array by the CL response obtained from a single crystalline Au substrate, for which we have a validated theoretical transition radiation (TR) excitation response function [13, 21]. This procedure is done in order to eliminate the setup response function. After the normalization, we subtracted the background in order to obtain the signal coming only from the photons created at the antenna position, and not from photons created due to defects in the substrate. We subtract background signal measured at the substrate far from the antenna from the signal acquired at and close to the antenna. Count levels on the CCD at bright antenna locations were about ~120 ADU.

In Fig. 4.3a we show the excitability maps measured (blue panels) on the different antennas of which the dimensions are indicated in Table 4.1. These figures show in general a very low excitability except at select locations that coincide with the extremities of the plasmon particles. This indicates the homogeneity of the substrate signal validating our background correction. In contrast, when the electron beam is positioned on the elements of the antenna we see that the intensity increases drastically. The maps show that the recorded intensity is highest at the ends of the plasmonic rods that compose the Yagi-Uda antenna. When comparing the different panels for a given antenna, i.e., when comparing different wavelengths, we also see that the recorded intensity distribution changes significantly with wavelength. For antenna YU1, for instance the reflector is the brightest element at 800 nm, while the other elements increase their signal intensity at shorter wavelengths. In general for all antennas we find the same behaviour, in the sense that the reflector is the most excitable at longer wavelengths while the feed and director elements become more easily excitable at shorter wavelengths. However, the precise order (in wavelength scale) in which directors progressively increase their excitability changes between antennas. An interesting observation that can be made from the measurements in the excitability maps is that, in the wavelength range used, all the elements support electric dipolar resonances. This is concluded from the maps which show that every rod element lights up at both ends of the rod, consistent with *in plane* electric dipolar currents excited with an electric point source aligned out of plane, just as the driving source obtained with CL. This result is also consistent with the study conducted in chapter 2, where we demonstrated based on far-field Fourier images that 100 nm long plasmonic rods show in-plane dipolar resonances at these working wavelengths.

In order to quantify the spectral response of every antenna element we integrate the recorded counts over an area of 4×4 pixels at the positions of maximum intensity as a function of wavelength. This dependence of intensity *vs.* wavelength is plotted in Fig. 4.3b. We consistently see that the e-beam excites resonances in the individual antenna elements which show up in our measurement as peaks with an average full
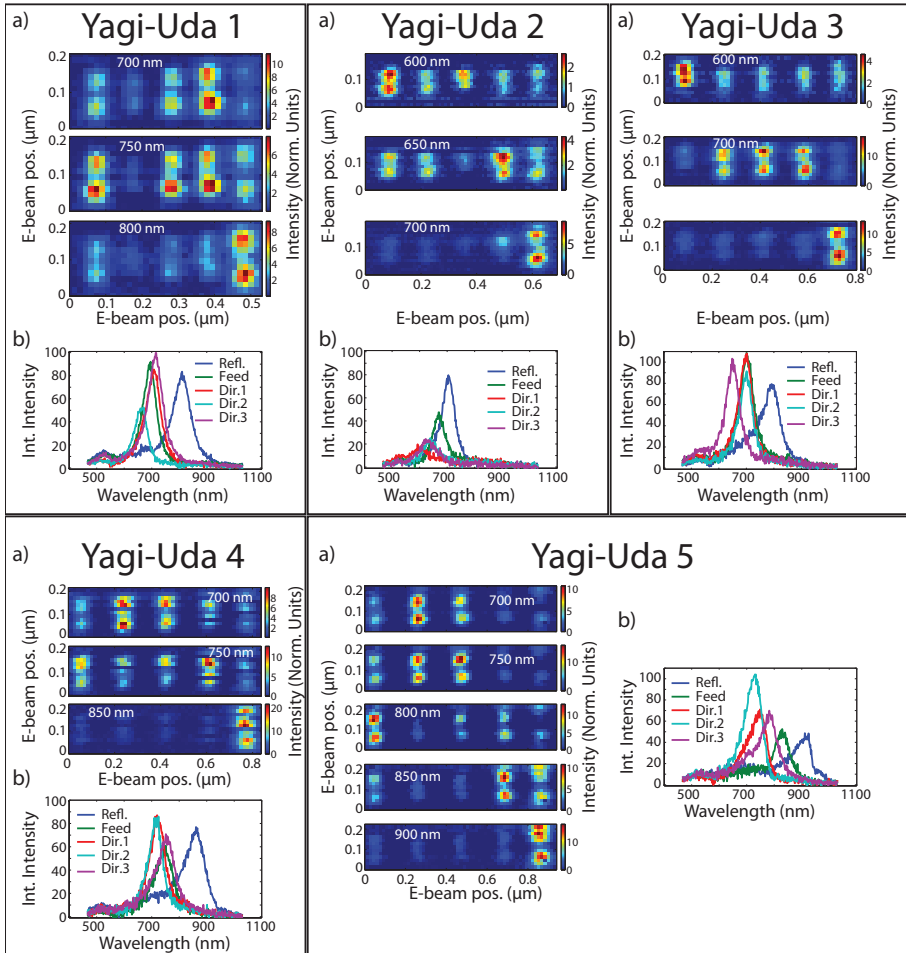
Figure 4.3: Panels a) show cathodoluminescence images of the Yagi-Uda antennas studied. These images present the signal acquired by a spectrometer when the electron beam spot is positioned at the positions indicated in the figures. The different wavelengths presented are indicated on the top of the image. Panels b) show the integrated spectra from the excitability maps at the positions of maximum excitation in the single elements that compose the antenna.

width half maximum (FWHM) of ~60 nm. Resonances close to 700 nm present the highest intensities in our measurements. This comes as a result of a combination of factors which include the gold plasmonic response. In general we see that the resonance central wavelengths red shift with increasing size of the antenna element. While the resonances of a given element should depend also on its neighbors, we first present a zero order analysis that neglects this coupling.

Fits to the spectra using a decomposition in Lorentzians show two resonances per element. The two Lorentzians are assigned to the in plane electric dipolar resonance along the antenna axes (long wavelengths and high peaks) and the out of plane dipolar resonance due to an oscillating current along the z direction, centered around λ=519 nm for all antenna elements. For the in-plane dipolar resonances the fitting procedure generally identifies one peak per resonance, unless the resonance is located far from the mean wavelength of the resonances of the other elements in the antenna. In such cases a shoulder is generally apparent. Such a shoulder is a direct signature that hybridization of resonances occurs through dipole-dipole interaction with neighboring antenna elements.

Fig. 4.4a shows the resonance wavelength dependence of all the elements as a function of the size of the element. Sizes are measured from SEM pictures of the antennas which gives an estimated accuracy of $\pm$10 nm. We see that longer rods present resonances at longer wavelengths. This resonance wavelength to size dependence is found to be linear, as seen by the fit in Fig. 4.4a. One might think that the linear dependence of resonance *vs.* size of the element is a trivial matter since it has been already studied in various published works [22–24]. It is important to realize that in this specific experiment a deep sub-wavelength excitation is performed locally on single antenna elements pertaining to a phased array antenna. Thus, this figure shows that the resonant response of an antenna element in a phased array antenna to a highly localized excitation is governed mainly by the response of the single element itself.

Nevertheless the phased array does have an influence on the response of some elements as evidenced in Fig. 4.4b. In this figure we show the main and secondary peaks fitted to the in-plane resonances for all elements of all antennas, sorted by the position of the element in the array. On the 'x' axis we present the different antenna elements (Reflector, Feed, *etc*...), while on the 'y' axis we present the center wavelength of the resonance of each antenna element. The directors and feed element show in general only the main resonance (blue symbols) and in few cases a small shoulder (red and cyan symbols). From these resonances we find the mean resonance wavelength $< \lambda_{dir} >$ per antenna which we use to normalize the 'y' axis in order to be able to compare all antennas in a single plot. The reflector element, being for all antennas the most disparate in size compared to the other elements, presents in all cases a shoulder in the resonant response peak (green and cyan symbols). This shoulder, as presented in Fig. 4.4b, is blue-shifted towards the mean wavelength of the director elements ($< \lambda_{dir} >$). This can be understood from the back-action exerted by the feed and directors on the reflector, when the reflector is the element driven by the electron beam. Another way to see this is to note that all the antenna elements hybridize due to the multiple scattering between the antenna elements. Since by design the reflector element is chosen to be strongly red-shifted compared to all other antenna elements, it is for this element that the hybridization process is most clearly visible in the data.

By investigating the resonances of the different elements of the Yagi-Uda antennas we find that in general the reflector presents a higher excitability at long wavelengths while the other elements have a low excitability at long wavelengths. In contrast at short wavelengths the feed and directors present a high excitability but the precise wavelength
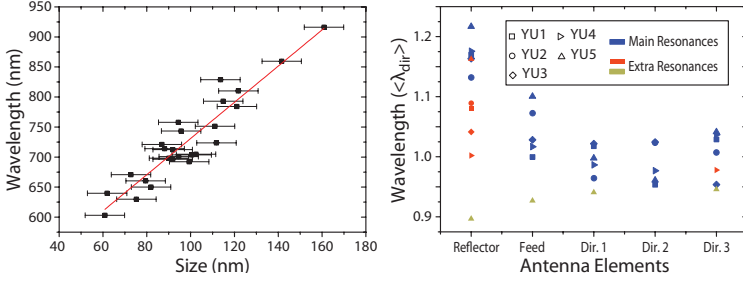
Figure 4.4: a) Wavelength of main resonance peak for every antenna element as a function of its length. b) Wavelength of the main and secondary resonances extracted form CL measurements for every element in the different antennas. The wavelengths are divided by the average wavelength of the director in every antenna, allowing us to visualize how close the secondary resonances are to the director resonance frequency.

and order at which this happens is not clearly evident from the measurements. In fact there is no clear correlation between the position of the antenna element and the wavelength at which its highest excitability occurs. A hypothesis that could explain the strong variability of the excitability of the director elements is based on the dependence of size *vs.* resonance wavelength shown in Fig. 4.4a. This figure indicates that a determining factor for this response might be found in small random size changes of the elements rather than their position in the array. On basis of this conjecture we turn to a theoretical study of phased array antennas, where we use a Monte Carlo approach to study the influence of random changes in antenna geometry.

4.2 Monte Carlo study of random disorder

We perform a Monte Carlo study of the properties of Yagi-Uda antennas and their dependence on intrinsic fabrication randomness of the geometry. Randomness is included in point dipole calculations as a deviation from the designed element geometry. As design geometry we use the dimensions of the antenna YU1 as stated in table 4.1. The deviations are introduced as a normal distribution of sizes with a standard deviation of 2.5 nm. An example of such a distribution for the antenna elements is shown in Fig. 4.5a. The point dipole calculation, as explained in Ref. [2, 25], is performed on antennas described by electrically polarizable prolate objects [26] by using the following self consistent point dipole expression:

$$\mathbf{p}_n = \overline{\alpha}_n(\mathbf{E}(\mathbf{r}_n) + \sum_{m \neq n} \omega^2 \mu \mu_0 \overline{\mathbf{G}}(\mathbf{r}_n, \mathbf{r}'_m)\mathbf{p}_m) \qquad (4.1)$$

where $\mathbf{p}_n$ and $\overline{\alpha}_n$ are the dipolar moment and polarizability of the rod element n, respectively. The rods are located at position $\mathbf{r}_n$ and are driven by the incident driving field $\mathbf{E}(\mathbf{r}_n)$ with a frequency ω. The environment is introduced both through the

Greens' function $\overline{\mathbf{G}}(\mathbf{r}_n, \mathbf{r}'_m)$ and through the permeability μ. Randomness is introduced through the polarizability $\overline{\alpha}$ of each element which changes in strength and resonance wavelength dependent on the size of the major and minor axes of the prolate spheroid. In these calculations we maintained the minor axis of the particle constant while the major axis is changed consistently with the normal distribution of Fig. 4.5a. We
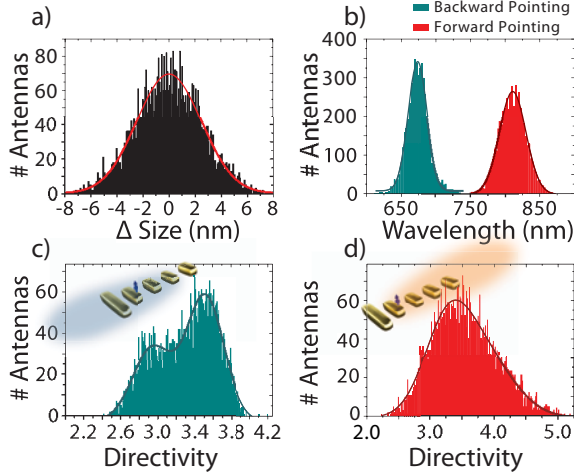
Figure 4.5: a) Distribution of the random deviations for all antenna elements, b) shows the distribution of wavelengths at which the directivity is maximum in either forward (red) or backward direction (cyan). c) and d) show the distributions of maximum directivity for the backward and forward directed radiation, respectively.

examine the response to Yagi-Uda antennas to localized excitation, setting the driving field $\mathbf{E}_{in}$ to the field of a dipolar current source. We calculate two important properties. The first is the directionality attained in emission, since this is the figure of merit that Yagi-Uda antennas are designed to improve. The second property we examine is the radiative local density of states, since this quantity should be a measure for the excitability in CL. By comparing simulations of the excitability of the different elements with and without a substrate for a number of cases, we found that the results agree well with each other and therefore we speed up the calculations using free space as embedding medium to increase the number of antennas and improve the statistical sampling.

We studied an ensemble of 5000 antennas, with a normal random size distribution independently drawn for each antenna element. We place an electric dipole at the feed position (the designed position of maximum directivity for a perfect antenna) and find the directivity (D) of each one of the realizations in the ensemble of 5000 antennas. For the directivity we use the following expression [27]: $D = max\left(4\pi U(\theta, \phi)/P_{tot}\right)$, where $U(\theta, \phi)$ is the radiation intensity and P_{tot} is the total emitted power which is

the angular integral of $U(\theta, \phi)$ over the 4π solid angle of a sphere. Thus, a perfectly isotropic source has $D = 1$ and a dipolar source which radiates perpendicular to its axes has $D = 1.64$. We also determine the wavelength at which $max(U(\theta, \phi))$ occurs. Results for directivity of all antennas when driven at the feed element are shown as histograms in Fig. 4.5. Panel a) shows a histogram of antenna size deviations, while panel b) shows the distribution of wavelengths of maximum forward and backward directivity, and panels c) and d) show histograms of the maximum directivity in either direction. We first discuss Fig. 4.5b, i.e., the wavelengths at which the antennas have a maximum directivity. There are two ranges of wavelengths at which the directivity peaks. The first peak in the histogram is centered around 674 nm with a FWHM of 27 nm, while the second peak is centered around 811 nm with a FWHM of 38 nm. For all antennas we find that the strongly directive emission occurring at short wavelengths is invariably (100% of the antennas) directed to the back of the antenna. On the other hand the strongly directive scattering occurring at long wavelengths (800 nm) is invariably directed to the front of the antenna. In general we find that when we drive these Yagi-Uda antennas at the feed element they all directionally radiate energy to the front side of the antenna at long wavelengths and to the back of the antenna when driven at short wavelengths. The original Yagi-Uda design is meant to operate through driving at the feed element and in the long wavelength band at 800 nm.

Fig. 4.5c and d show histograms of the maximum backward and forward directivity for the antenna ensemble. The backward directivity distribution (Fig. 4.5c) is centered at an average directivity $< D >=3.3$ and shows a bi-modal distribution to which we fit a double Gaussian as guide to the eye (blue line). For these two distributions we found a FWHM of 0.92. Fig. 4.5d shows the distribution of directivity for the forward directive radiation, corresponding to the actual design purpose of the antenna. This distribution is found to be centered at an average directivity $< D >=3.5$. The forward directivity distribution is spread in a single asymmetric peak with a FWHM of 0.97. In general these results indicate the robustness that the Yagi-Uda antennas have for angle and direction of its emission. We attribute this robustness due to the fact that the Yagi-Uda antenna operates by interference, which is generally not sensitive to variations of a few nm's, as opposed to operating on plasmonic near-field enhancement effects. However, we note that in this study we did not include positional disorder. The position accuracy of the e-beam during lithographic definition of the antennas is superior to the particle size accuracy.

The fact that Yagi-Uda antennas are robust against disorder when it comes to directivity need not imply that they are also robust when it comes to radiative LDOS enhancement, i.e., CL excitability. Fig. 4.6 shows the radiative LDOS for positions located at each one of the Yagi-Uda antenna elements. In essence such a calculation answers the question how sensitive CL maps, such as those shown in Fig. 4.3 for antenna YU1, are to size variations of the elements of nominally identical antennas. The different panels in Fig. 4.6a show radiative LDOS at wavelengths of 650, 700, 750 and 800 nm as indicated above the panels. In order to improve the readability of these figures we organize the different antenna realizations according to a digitization of the radiative LDOS. This digitization is inspired by Fig. 4.3, from which it appears that a
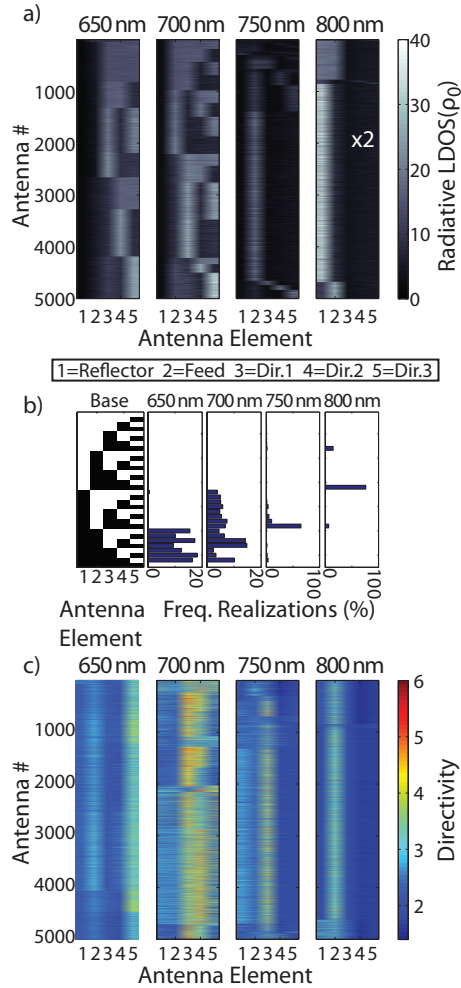
Figure 4.6: a) Radiative LDOS calculated for excitations at every one of the elements of the antennas. These calculations are done for 5000 realizations of antennas with random changes in the size of all their elements (σ =2.5 nm). b) Organizational base used and histograms with the frequency of occurrence of each pattern found in panels a). c) Directivity calculated for excitations at every one of the elements of the 5000 antenna realization.

particle as a whole will either be responsive and "bright" in a CL map, or "dark". For instance, from Fig. 4.3 it appears that at long wavelengths, for all antennas all particles are dark except for the last (digitized as 00001). As an arbitrary thresholding procedure for digitization we label any particle that has radiative LDOS within 20% of that of the

highest LDOS particle in the array as bright, and all others as dark. With this definition we can sort antenna realizations using an organizing base as shown in Fig. 4.6b. This organizing base is defined as the enumeration of all different possibilities of 'on' and 'off' states in a 5 element binary array. The sorting allows to assess visually what excitability maps should be predominantly observed for a given wavelength. We present our results as follows. Fig. 4.6a shows the calculated radiative LDOS as grayscale on all 5000 antennas, sorted according to the digitization base in panel 6b. In order to assess how many antennas would be quantified to correspond to a certain five digit binary "on-off" pattern Fig. 4.6b shows histograms with the frequency of occurrence of each pattern. For 650 nm we see that the reflector element is mostly not excitable, while the element where the highest radiative LDOS is located is usually one of the directors. Only for very few cases (<1%) (top of Fig. 4.6a left panel), the feed element is found as a highly excitable element. Since this wavelength matches very well to the resonance of the directors, and not that of the feed and reflector, it is not surprising that they are generally easiest to excite. Nevertheless, the excitability of these elements may vary from 'on' to 'off' state, which is a clear sign of the sensitivity of hybridization between nominally identical elements to the actual geometry.

For 700 nm we find more realizations (44%) where the feed element is highly excitable. Again just as for 650 nm, excitability is mainly distributed over all director elements with a large variation between realizations. For 750 nm the trend shows that in general the radiative LDOS is lower than for 650 and 700 nm, with a maximum average of $12.7\rho_0$ located at the feed element. For circa 70% of the realizations the feed is the only excitable element, while in 30% of the realizations also director elements show high LDOS. Finally, at long wavelengths (800 nm) we find that mostly the reflector is the element with the highest excitability (above 90% of realizations). Realizations where both the reflector and the feed element are highly excitable are also found. Broadly speaking, the conclusion that the excitability shifts from directors to feed and reflector when approaching the red edge of the spectrum is consistent with the difference in element size, and also borne out by our experimental observations. A less trivial conclusion is that in the 650 to 700 nm spectral range, the excitability strongly differs from antenna to antenna realization and is spread over the entire set of directors. This is also consistent with the wavelength range over which experimental excitability maps show patterns spread out over the directors and large differences between antennas.

A final question we examine is if near-field CL measurements on a given antenna should be expected to have predictive power to say something about directivity. For this we proceed to compare the previous calculations of radiative LDOS to calculations of the directivity attained by every antenna of the ensemble. We present the results in Fig. 4.6c by showing maps of the directivity calculated for the studied ensemble of antennas. We organize the antennas in the same order as the one found for the radiative LDOS figure in Fig. 4.6a. That is, we can compare every realization from both figures directly. The panels in c) are organized by wavelength starting with 650 nm and ending with 800 nm just as in panel a). Again every column in the panel defines the element position at which a current source is placed to drive the antenna. We see that at 650 nm

the radiation is most directional when the antenna is driven through director 3. At 700 nm both director 1 and 2 provide strong directional emission with <D>=3.7 and 3.4. At 750 nm director 1 creates the most directional emission with a max(D)=6.4 and <D>=3.08. Finally at 800 nm, which is the wavelength at which the antenna is designed to work, the antenna presents its maximum directionality when driven at the feed element, with a <D>=3.06 and a max(D)=5.0.

Comparison of Fig. 4.6a and 4.6c suggests that there is little correlation between LDOS maps and maximum directionality except for the antenna design wavelength (800 nm). That is, at 800 nm for all antennas that are directional as designed (highest directionality obtained at the feed element), the radiative LDOS map indicates highest radiative LDOS at the reflector. Conversely, those antennas in which the LDOS map shows low excitability in the reflector tend to also show poor directivity performance. At other wavelengths, however, it is evident that the correlation between radiative LDOS distribution and directivity is poor. At 700 nm, for instance, directivity is high for excitation at directors 3 and 4 almost irrespective of the antenna realization, although antenna realizations have very different LDOS maps.

4.3 Conclusions

We reported cathodoluminescence images of phased array antennas fabricated on 1D Si_3N_4 waveguide. The images clearly show in-plane electric dipole resonances in the individual elements. To first order the resonance wavelengths per element simply follow the expected size relation for single elements. However, spectra per element show subtle features of hybridization. We observe large variations in pattern at wavelengths shorter than 750 nm. We performed a Monte Carlo study of radiative LDOS and directivity for antennas modeled as point dipoles with randomly varying particle size. We find that directivity features are fairly robust at the design wavelength, and that the design usage of exciting the feed means high directivity but low radiative LDOS. At shorter wavelengths antennas may be strongly directional too, in the opposite direction. We expect LDOS maps at these shorter wavelengths to vary remarkably strongly. This study highlights the importance of studying robustness to fabrication disorder in plasmonic designs of antennas, especially since different figures of merits will be very differently affected.

References

[1] R. D. Kekatpure, E. S. Barnard, W. Cai, and M. L. Brongersma, *Phase-coupled plasmon-induced transparency*, Phys. Rev. Lett. **104**, 243902 (2010).

[2] F. Bernal Arango, A. Kwadrin, and A. F. Koenderink, *Plasmonic antennas hybridized with dielectric waveguides*, ACS Nano **6**, 10156 (2012).

[3] K. Yanazawa, Y. Tobisu, S. Maeda, H. F. Hofmann, and Y. Kadoya, *Radiation and receiving gain of nano-optical yagi-uda antenna embedded in slab dielectric waveguide*, in *CLEO: 2013*, page QF2A.8, Optical Society of America, 2013.

[4] A. Kriesch, S. P. Burgos, D. Ploss, H. Pfeifer, H. A. Atwater, and U. Peschel, *Functional plasmonic nanocircuits with low insertion and propagation losses*, Nano Letters **13**, 4539 (2013).

[5] C.-G. Xu, X. Xiong, C.-L. Zou, X.-F. Ren, and G.-C. Guo, *Efficient coupling between dielectric waveguide modes and exterior plasmon whispering gallery modes*, Opt. Express **21**, 31253 (2013).

[6] N. S. King, M. W. Knight, N. Large, A. M. Goodman, P. Nordlander, and N. J. Halas, *Orienting nanoantennas in three dimensions to control light scattering across a dielectric interface*, Nano Letters **13**, 5997 (2013).

[7] A. Manekkathodi, Y.-J. Wu, L.-W. Chu, S. Gwo, L.-J. Chou, and L.-J. Chen, *Integrated optical waveguide and photodetector arrays based on comb-like zno structures*, Nanoscale **5**, 12185 (2013).

[8] M. Chamanzar, Z. Xia, S. Yegnanarayanan, and A. Adibi, *Hybrid integrated plasmonic-photonic waveguides for on-chip localized surface plasmon resonance (lspr) sensing and spectroscopy*, Opt. Express **21**, 32086 (2013).

[9] R. Bruck and O. L. Muskens, *Plasmonic nanoantennas as integrated coherent perfect absorbers on soi waveguides for modulators and all-optical switches*, Opt. Express **21**, 27652 (2013).

[10] R. Tellez-Limon, M. Fevrier, A. Apuzzo, R. Salas-Montiel, and S. Blaize, *Theoretical analysis of bloch mode propagation in an integrated chain of gold nanowires*, Photon. Res. **2**, 24 (2014).

[11] M. Février, P. Gogol, G. Barbillon, A. Aassime, R. Mégy, B. Bartenlian, J.-M. Lourtioz, and B. Dagens, *Integration of short gold nanoparticles chain on soi waveguide toward compact integrated bio-sensors*, Opt. Express **20**, 17402 (2012).

[12] A. G. Curto, G. Volpe, T. H. Taminiau, M. P. Kreuzer, R. Quidant, and N. F. van Hulst, *Unidirectional emission of a quantum dot coupled to a nanoantenna*, Science **329**, 930 (2010).

[13] T. Coenen, E. J. R. Vesseur, A. Polman, and A. F. Koenderink, *Directional emission from plasmonic yagi-uda antennas probed by angle-resolved cathodoluminescence spectroscopy*, Nano Lett. **11**, 3779 (2011).

[14] T. Coenen, E. J. R. Vesseur, and A. Polman, *Angle-resolved cathodoluminescence spectroscopy*, Applied Physics Letters **99**, (2011).

[15] T. Coenen, F. Bernal Arango, A. Femius Koenderink, and A. Polman, *Directional emission from a single plasmonic scatterer*, Nat Commun **5**, (2014).

[16] T. Coenen and A. Polman, *Polarization-sensitive cathodoluminescence fourier microscopy*, Opt. Express **20**, 18679 (2012).

[17] M. Frimmer, T. Coenen, and A. F. Koenderink, *Signature of a fano resonance in a plasmonic metamolecule's local density of optical states*, Phys. Rev. Lett. **108**, 077404 (2012).

[18] M. Kuttge, E. J. R. Vesseur, A. F. Koenderink, H. J. Lezec, H. A. Atwater, F. J. García de Abajo, and A. Polman, *Local density of states, spectrum, and far-field interference of surface plasmon polaritons probed by cathodoluminescence*, Phys. Rev. B **79**, 113405 (2009).

[19] F. J. García de Abajo, *Optical excitations in electron microscopy*, Rev. Mod. Phys. **82**, 209 (2010).

[20] R. Sapienza, T. Coenen, J. Renger, M. Kuttge, N. F. van Hulst, and A. Polman, *Deep-subwavelength imaging of the modal dispersion of light*, Nat Mater **11**, 781 (2012).

[21] M. Kuttge, E. J. R. Vesseur, J. Verhoeven, H. J. Lezec, H. A. Atwater, and A. Polman, *Loss mechanisms of surface plasmon polaritons on gold probed by cathodoluminescence imaging spectroscopy.*, Applied Physics Letters **93**, (2008).

[22] G. W. Bryant, F. J. García de Abajo, and J. Aizpurua, *Mapping the plasmon resonances of metallic nanoantennas*, Nano Letters **8**, 631 (2008).

[23] J. Dorfmüller, R. Vogelgesang, W. Khunsin, C. Rockstuhl, C. Etrich, and K. Kern, *Plasmonic nanowire antennas: Experiment, simulation, and theory*, Nano Letters **10**, 3596 (2010).

[24] E. S. Barnard, T. Coenen, E. J. R. Vesseur, A. Polman, and M. L. Brongersma, *Imaging the hidden modes of ultrathin plasmonic strip antennas by cathodoluminescence*, Nano Letters **11**, 4265 (2011).

[25] L. Novotny and B. Hecht, *Principles of Nano-optics*, Cambridge University Press, Cambridge, 2006.

[26] C. F. Bohren and D. R. Huffmann, *absorption and scattering of light by small particles*, Wiley, New York, 1983.

[27] C. A. Balanis, *Antenna Theory: Analysis and Design*, Wiley, New Jersey, 3 edition, 2005.

5

Method to Retrieve Magneto-Electric Polarizability Tensors of Metamaterial Antennas

A key quantity in design of plasmonic antennas and metasurfaces, as well as metamaterials, is the electrodynamic polarizability of a single scattering building block. In particular, in the current merging of plasmonics and metamaterials, subwavelength scatterers are judged by their capability to present a large, generally anisotropic electric and magnetic polarizability, as well as a bi-anisotropic magnetoelectric polarizability. This bi-anisotropic response, whereby a magnetic dipole is induced through electric driving, and vice versa, is strongly linked to optical activity and chiral response of plasmonic metamolecules. We present two distinct methods to retrieve the polarizability tensor from electrodynamic simulations. As basis for both we use the Surface Integral Equation method (SIE) to solve for the scattering response of arbitrary objects exactly. In the first retrieval method, we project scattered fields onto vector spherical harmonics with aid of an exact discrete spherical harmonic Fourier transform on the unit sphere. In the second, we take the effective current distributions generated by SIE as basis to calculate dipole moments. We verify that the first approach holds for scatterers of any size, while the second is only approximately correct for small scatterers. We present benchmark calculations, revisiting the zero-forward scattering paradox of Kerker [1] and Alú [2], relevant in dielectric scattering cancelation and sensor cloaking designs.

5.1 Introduction

Metallic and dielectric nano-scatterers currently enjoy a surge of interest in photonics, due to the unusual optical properties that may be obtained through a suitable choice

of material and geometry. In plasmonics, it is well established that Ag and Au single nano-spheres, rods, wires, pyramids, triangles, cubes, stars or core-shell particles, as well as oligomers and arrays of such objects have very distinct scattering resonances that can be used for optical sensing, improvement of LEDs and solar cells, as well as plasmon-enhanced spectroscopy on basis of large field enhancements near metals at the plasmon resonance [3–9]. In a related development, the field of metamaterials uses metal split rings, loops, as well as so called cut-wire pairs to generate a strong collective magnetic response [10–12]. The effective magnetic permeability and electric permittivity that is achieved arises from the strong electric and magnetic polarization obtained in each building block. Recently, the fields of plasmonics and metamaterials have come together in so-called 'metasurfaces', where non-identical subwavelength resonant scatterers are organized in a plane at subwavelength distances, in order to achieve arbitrary phase and amplitude masks that control the transmission, reflection, refraction and diffraction of light [13–15]. In all these developments, the response is fundamentally quantified by the geometrical arrangement of scatterers on one hand, and the electric and magnetic polarizability of each building block on the other hand.

Numerical methods in electrodynamics play an increasingly important role in the design and understanding of nano structures in an electromagnetic field. In daily practice, finite difference time domain codes, finite element simulations, and boundary element methods are used to replicate experiments, and extract expected observables such as transmission and reflection coefficients, or the brightness and directivity of localized sources. Remarkably, it is not common practice to use simulations to extract the fundamental parameter, i.e., the electric and magnetic polarizability, as well as possibly higher order multipoles, that quantify how a building block scatterers. A first step to this goal is a recent paper by Mühlig et al. [16] that shows a retrieval of the multipolar moments induced in various metamaterial scatterers for a particular incident field. Here we propose a rapid and accurate method to retrieve electric, magnetic and magneto-electric polarizabilities of meta-atoms which can be applied to any electromagnetic solver (FDTD [17], VEM [18], BEM [19]). In our specific implementation this method is based on Surface Integral Equation calculations to solve Maxwell equations for electric and magnetic field exactly, and to calculate the induced effective electric and magnetic surface currents that quantify the scatterer response. We show how to extract polarizabilities both from the calculated scattered field, and as an alternative method, also from the induced currents. This chapter is organized as follows. In section 5.2 we present the surface integral equation method, and the retrieval of polarizability tensors. In section 5.3 and 5.4 we benchmark the retrieval for magnetoelectric spheres, illustrating the zero-forward scattering paradox of Kerker.

5.2 Surface integral equation method and α-tensor retrieval

Any electromagnetic problem is completely specified by the Maxwell equations, together with a definition of the source, and the boundary condition. We use the

equations in integral form [20]. We divide space into a region 1, defined as the embedding medium that we take to be a homogeneous dielectric with permittivity ϵ_1 and permeability μ_1, and a region 2 that represents the volume occupied by the scattering material of dielectric constant ϵ_2 and permeability μ_2. In the integral equation formalism, it is useful to solve for the electromagnetic response by first finding effective auxiliary electric and magnetic surface current densities **J** and **M** on the interface between medium 1 and 2 that are used to satisfy the boundary conditions for continuity of tangential **E** and **H**, and normal **B** and **D**. Once these surface currents are solved for, they can be used to construct the electromagnetic field solution everywhere. Assuming harmonic time dependence (frequency ω) the currents are set by an Electric Field Integral Equation (EFIE),

$$\frac{\omega \mu_i}{i} \int_S dS' \overline{\mathbf{G}}_i(\mathbf{r}, \mathbf{r}') \cdot \mathbf{J}(r') - \int_S dS' [\nabla' \times \overline{\mathbf{G}}_i(\mathbf{r}, \mathbf{r}')] \cdot \mathbf{M}(\mathbf{r}') = \begin{cases} \mathbf{E}_1^{\mathbf{inc}}(\mathbf{r}) & \text{for } \mathbf{r} \text{ in region i} = 1 \\ 0 & \text{for } \mathbf{r} \text{ in region i} = 2 \end{cases} \tag{5.1}$$

and a Magnetic Field Integral Equation (MFIE) that reads:

$$\int_S dS' [\nabla' \times \overline{\mathbf{G}}_i(\mathbf{r}, \mathbf{r}')] \cdot \mathbf{J}(\mathbf{r}') + \frac{\omega \epsilon_i}{i} \int_S dS' \overline{\mathbf{G}}_i(\mathbf{r}, \mathbf{r}') \cdot \mathbf{M}(\mathbf{r}') = \begin{cases} \mathbf{H}_1^{\mathbf{inc}}(\mathbf{r}) & \text{for } \mathbf{r} \text{ in region i} = 1 \\ 0 & \text{for } \mathbf{r} \text{ in region i} = 2 \end{cases}. \tag{5.2}$$

Here $\overline{\mathbf{G}}(\mathbf{r}, \mathbf{r}')$ is the electric dyadic Green function for each type of homogeneous medium 'i' (with i = 1, 2) and $\nabla' \times \overline{\mathbf{G}}(\mathbf{r}, \mathbf{r}')$ is the curl of the Green's function. The integral runs over the surface S that contains the current densities. We use the method introduced by Kern et al. [21], which is based on the method of moments (MoM) [22], coined the Surface Integral Equation (SIE) method to solve these equations. In brief, in the SIE method any scatterer is represented by effective electric and magnetic surface current densities **J** and **M** that are discretized on finite elements over the surface of the scatterer with the help of the Rao, Wilton and Glisson (RWG) basis functions $\mathbf{f}_n$ [23]. Consider the surface S meshed with triangles. We define $n = 1 \dots N$ nodes as the shared edges of the triangles. The basis function $\mathbf{f}_n(\mathbf{r})$ is zero everywhere except on the triangle pair $T^\pm$ that shares node n. Here the function is pyramid shaped, with,

$$\mathbf{f}_n = \begin{cases} \frac{\pm L_n}{2 A_n^\pm} \left(\mathbf{r} - \boldsymbol{p}_n^\pm \right) & : \mathbf{r} \in T^\pm \\ 0 & : \text{otherwise} \end{cases} \tag{5.3}$$

where L_n is the length of the shared node, $A_n^\pm$ is the area of the triangle pair and $\boldsymbol{p}_n^\pm$ are the non-shared vertices of the triangles, as explained in [21]. The discretized strength and direction of the currents is accounted for through basis expansion coefficients α_n and β_n in the following way,

$$\mathbf{J}(\mathbf{r}) = \sum_{n=1}^N \alpha_n \mathbf{f}_n(\mathbf{r}) \tag{5.4}$$

$$\mathbf{M}(\mathbf{r}) = \sum_{n=1}^N \beta_n \mathbf{f}_n(\mathbf{r}). \tag{5.5}$$

By projecting the EFIE and MFIE equations onto the RWG basis functions, the integral equations transform into a set of linear equations for the α_n and β_n values:

$$\mathcal{M} \cdot \begin{pmatrix} \alpha_n \\ \beta_n \end{pmatrix} = q. \tag{5.6}$$

In this system of linear equations the matrix $\mathcal{M}$ needs to be found only once and can be used for any incident field, that is only contained in q. The matrix $\mathcal{M}$ is defined by:

$$\mathcal{M} = \begin{bmatrix} D^1 + D^2 & -K^1 - K^2 \\ K^1 + K^2 & \frac{D^1}{Z_1^2} + \frac{D^2}{Z_2^2} \end{bmatrix} \tag{5.7}$$

where $Z_i = \sqrt{\mu_i/\epsilon_i}$,

$$D^i_{mn} = \frac{\omega\mu_i}{i} \int_{S_m} dS \mathbf{f}_m(\mathbf{r}) \cdot \int_{Sn} dS' \overline{\mathbf{G}}_i(\mathbf{r},\mathbf{r}') \cdot \mathbf{f}_n(\mathbf{r}'), \tag{5.8}$$

$$K^i_{mn} = \int_{S_m} dS \mathbf{f}_m(\mathbf{r}) \cdot \int_{Sn} dS' \nabla' \times \overline{\mathbf{G}}_i(\mathbf{r},\mathbf{r}') \cdot \mathbf{f}_n(\mathbf{r}'). \tag{5.9}$$

Note how $\mathcal{M}$ self-consistently contains the interactions between all the discretized current elements, as evident from the appearance of $\overline{\mathbf{G}}_i(\mathbf{r},\mathbf{r}')$. After this matrix is calculated it can be inverted and multiplied by the vector q which is the projection of the incident field that drives the scatterer into the RWG functions. Specifically,

$$q = \begin{cases} \int_{S_m} dS \mathbf{f}_m(\mathbf{r}) \cdot \mathbf{E}_1^{inc}(\mathbf{r}) & : m = 1....N \\ \int_{S_{m-N}} dS \mathbf{f}_{m-N}(\mathbf{r}) \cdot \mathbf{H}_1^{inc}(\mathbf{r}) & : m = N+1....2N. \end{cases} \tag{5.10}$$

We order the variables such that the vector q has the projections of $\mathbf{E}^{inc}$ on the N basis functions as the first N elements, and the projection of $\mathbf{H}^{inc}$ on the basis functions as elements $N+1$ to $2N$. As an important implementation note, one of the key features of this method is that the Green's function, which is singular at $\mathbf{r} = \mathbf{r}'$, is written as the sum of a smooth $\overline{\mathbf{G}}(\mathbf{r},\mathbf{r}_0)_S$ and singular part $\overline{\mathbf{G}}(\mathbf{r},\mathbf{r}_0)_{NS}$ as follows

$$\overline{\mathbf{G}}(\mathbf{r},\mathbf{r}_0)_S = [\overline{1} + \frac{\nabla\nabla}{k_i^2}]G(\mathbf{r},\mathbf{r}_0)_S = [\overline{1} + \frac{\nabla\nabla}{k_i^2}]\frac{1}{4\pi}\left(\frac{e^{ik_iR}-1}{R} + \frac{k_i^2 R}{2}\right), \tag{5.11}$$

$$\overline{\mathbf{G}}(\mathbf{r},\mathbf{r}_0)_{NS} = [\overline{1} + \frac{\nabla\nabla}{k_i^2}]G(\mathbf{r},\mathbf{r}_0)_{NS} = [\overline{1} + \frac{\nabla\nabla}{k_i^2}]\frac{1}{4\pi}\left(\frac{1}{R} - \frac{k_i^2 R}{2}\right) \tag{5.12}$$

where k_i is the wave vector defined as $k_i = 2\pi/\lambda \cdot \sqrt{\mu_i\epsilon_i}$ and $R = |\mathbf{r} - \mathbf{r}_0|$. The singular part of the integral is treated analytically. For a detailed explanation of this separation method, we refer to Ref. [21]. Without this separation, the matrix $\mathcal{M}$ would be highly inaccurate on its diagonal, as well as for elements D_{mn} and K_{mn} that correspond to close triangles. Moreover subsequent retrieval of the scattered field from the calculated currents would be highly inaccurate close to the scatterers.

Once found, the coefficients α_n and β_n completely specify the electric and magnetic surface currents that in turn allow one to find the scattered field and the total field by propagating the currents with the aid of the Green's function in the following manner:

$$\mathbf{E}_i(\mathbf{r}) = \begin{Bmatrix} + \\ - \end{Bmatrix} \sum_n \left[-\alpha_n \frac{\omega\mu_i}{i} \int_{S_n} dS' \overline{\mathbf{G}}(\mathbf{r},\mathbf{r}') \cdot \mathbf{f}_n(\mathbf{r}') \right.$$
$$\left. + \beta_n \int_{S_n} dS' [\nabla' \overline{\mathbf{G}}(\mathbf{r},\mathbf{r}')] \times \mathbf{f}_n(\mathbf{r}') \right] + \begin{cases} \mathbf{E}_1^{inc}(\mathbf{r}): & \text{for } \mathbf{r} \text{ in region i}=1 \\ 0: & \text{for } \mathbf{r} \text{ in region i}=2 \end{cases} \quad (5.13)$$

$$\mathbf{H}_i(\mathbf{r}) = \begin{Bmatrix} + \\ - \end{Bmatrix} \sum_n \left[-\beta_n \frac{\omega\epsilon_i}{i} \int_{S_n} dS' \overline{\mathbf{G}}(\mathbf{r},\mathbf{r}') \cdot \mathbf{f}_n(\mathbf{r}') \right.$$
$$\left. - \alpha_n \int_{S_n} dS' [\nabla' \overline{\mathbf{G}}(\mathbf{r},\mathbf{r}')] \times \mathbf{f}_n(\mathbf{r}') \right] + \begin{cases} \mathbf{H}_1^{inc}(\mathbf{r}): & \text{for } \mathbf{r} \text{ in region i}=1 \\ 0: & \text{for } \mathbf{r} \text{ in region i}=2 \end{cases} \quad (5.14)$$

We have implemented the described algorithm in MATLAB, using triangular surface gridding that defines the set of $\mathbf{f}_n(\mathbf{r})$ as input that we generated using Gmsh [24]. The main objective of our paper is to discuss the retrieval of polarizabilities from the SIE calculations. On basis of the current contributions found through SIE *two* different approaches can be taken in order to find the polarizability tensor. On one hand the fields produced by the effective currents can be propagated with the aid of $\overline{\mathbf{G}}$ and $\nabla' \times \overline{\mathbf{G}}$ (Eq. (5.13) and Eq. (5.14)) onto a sphere that is centered around the structure under consideration. The projection of the fields on the sphere on vector spherical harmonics directly define the multipole moments through the expansion coefficients a_{nm} and b_{nm}, as explained by Jackson [Ch.10][20], as well as by Mühlig et al. [16]. Thus, for this first retrieval method we use two steps. First we use SIE to solve for the fields $\mathbf{E}$ and $\mathbf{H}$ and then we project these fields onto VSH to find the dipolar moments and hence the polarizability tensor. This means that $\mathbf{E}$ and $\mathbf{H}$ might as well be found by using any other full wave calculation, for instance FDTD or FEM. As an alternative method, multipole moments can be defined directly from the current distributions, without calculating fields. Here we first discuss the multipole expansion method, and then the direct definition based on $\mathbf{J}$ and $\mathbf{M}$.

Multipole moments based on the projection onto Vector spherical harmonics

We use the vector spherical harmonic functions as defined by Mühlig et al. [16], which are equivalent to the textbook definition of [25]. As proven in [25] the vector spherical harmonics form a complete and orthonormal set [25]. Therefore the field $\mathbf{E}(r,\theta,\phi)$ found from SIE has a unique expansion

$$\mathbf{E}(r,\theta,\phi) = \sum_{n=1}^{\infty} \sum_{m=-n}^{n} [a_{nm}\mathbf{N}_{nm}(r,\theta,\phi) + b_{nm}\mathbf{M}_{nm}(r,\theta,\phi)], \quad (5.15)$$
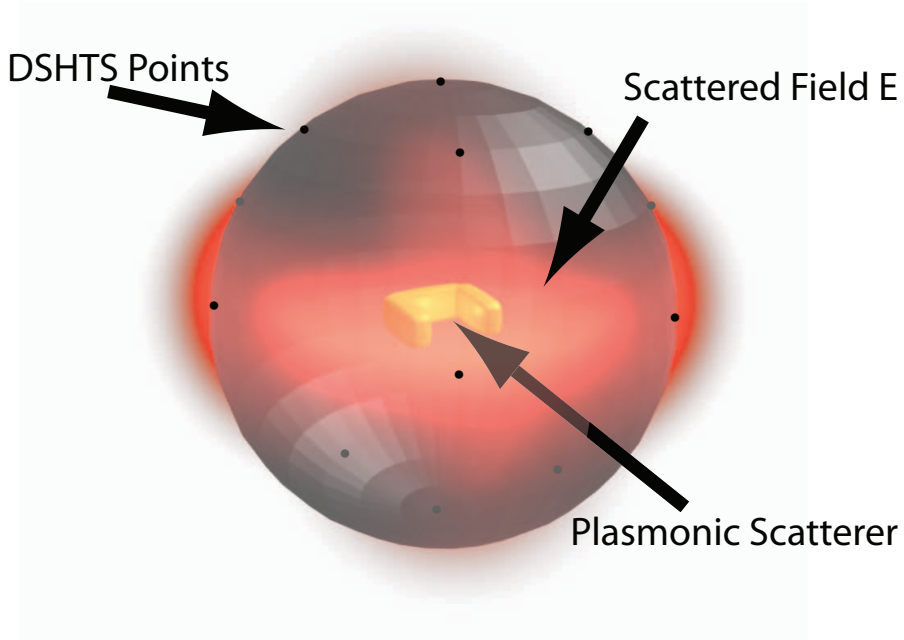
Figure 5.1: Sketch of the calculation protocol for retrieving multipolar moments with vector spherical harmonics (VSH). Here a gold split ring represents the scatterer, while the scattered field is represented in red. The sphere and black points, located around the scatterer and field, show how we only use a small number of points at which we calculate the electric field for the discrete spherical harmonics transform on the sphere (DSHTS).

where the expansion coefficients a_{nm} and b_{nm} can simply be found by taking the inner product of the calculated $\mathbf{E}(r,\theta,\phi)$ with the vector spherical harmonic functions. Here $\mathbf{N}_{nm}(r,\theta,\phi)$ and $\mathbf{M}_{nm}(r,\theta,\phi)$ are the vector spherical harmonic functions, and the inner product is defined as the integration over the unit sphere. Therefore the a_{nm} and b_{nm} coefficients are corresponding to the "Mie" coefficients [20]. While in principle one could densely sample $\mathbf{E}(r,\theta,\phi)$ on the unit sphere to evaluate the inner product, it is particularly advantageous to use the fact that a discrete spherical harmonic transform is exact for Legendre polynomials up to order N if sampling points and weights are chosen consistent with Legendre quadratures for Legendre polynomials of order $N+1$. Thereby one can obtain a highly efficient and ***exact*** algorithm, that requires only very few field sampling points for multipole expansion coefficients up to order $n=N$ [26], by carefully separating the vector spherical harmonics into ordinary spherical harmonics. As in any discrete Fourier transform, the only caveat for this exact method is that aliasing artifacts may occur if the radiated field contains significant contribution from multipoles of order higher than the truncation order of the transform. Therefore we use a truncation order $N=5$, corresponding to just 50 sampling points on the unit sphere,

as we do not expect multipole moments beyond N=2 to be significant throughout this chapter. The coefficients a_{nm}, and b_{nm}, and hence the retrieved moments finally, will depend on where the center of the sphere is chosen [16, 20, 27] but are independent of the radius of the sphere as long as the scatterers are fully enclosed. The dipolar moments $\mathbf{p}$ and $\mathbf{m}$ are calculated from the coefficients a_{nm} and b_{nm} using the procedure explained in [16]. A sketch of how this calculation is performed is shown in Fig. 5.1.

Multipole moments based on the effective currents

As a second method to obtain the induced dipole moments $\mathbf{p}$ and $\mathbf{m}$ (electric and magnetic dipole moments) we can directly use the effective magnetic and electric current densities $\mathbf{M}$ and $\mathbf{J}$ calculated as the intermediate solution step in SIE. In particular

$$\mathbf{p} = \frac{i}{k}\sqrt{\mu\epsilon}\int_\Omega \mathbf{J}(\mathbf{r})dS - \frac{\epsilon}{2}\int_\Omega \mathbf{r}\times\mathbf{M}dS \qquad (5.16)$$

$$\mathbf{m} = \frac{i}{k}\sqrt{\frac{\epsilon}{\mu}}\int_\Omega \mathbf{M}(\mathbf{r})dS + \frac{1}{2}\int_\Omega \mathbf{r}\times\mathbf{J}dS, \qquad (5.17)$$

where the integration is performed over the surface of the scatterer Ω. In contrast to other brute force methods, SIE naturally provides the effective magnetic and electric currents as an essential part of its solution strategy. In standard implementations of, for instance, FDTD modeling, retrieving these currents with enough numerical accuracy would itself be a challenge. On a standard FDTD Yee-grid inaccuracies arise from the approximation of curved boundaries into discretized Cartesian grids, as well as from the fact that in general the field components and their derivatives are not sampled right on the boundary. Consequently, right at object boundaries large inaccuracies of local fields, fluxes and currents are obtained unless one uses specially improved FDTD algorithms [28]. The definitions of the RWG basis functions imply that

$$\int_{T^+ + T^-} \mathbf{f}_n(\mathbf{r})dS = L_n(\mathbf{r}_n^{c-} - \mathbf{r}_n^{c+}) \qquad (5.18)$$

$$\int_{T^+ + T^-} \mathbf{r}\times\mathbf{f}_n(r)dS = (L_n/6)(p_n^+ - p_n^-)\times(\mathbf{r}_2 + \mathbf{r}_3), \qquad (5.19)$$

where $\mathbf{r}_n^{c-}$ and $\mathbf{r}_n^{c+}$ are the centroid vector of the two triangles that share node n, L_n is the length of the shared line between the two triangles, and finally $\mathbf{r}_2$ and $\mathbf{r}_3$ are the vector positions of the shared vertices of the two triangles. Inserting these results in the discretized form of Eq. (5.16 and 5.17) allows to retrieve $\mathbf{p}$ and $\mathbf{m}$ in terms of the coefficients α_n and β_n:

$$\mathbf{p} = \frac{i}{k}\sqrt{\mu\epsilon}\sum_{n=1}^N L_n(\mathbf{r}_n^{c-} - \mathbf{r}_n^{c+})\alpha_n - \frac{\epsilon}{2}\sum_{n=1}^N (L_n/6)(p_n^+ - p_n^-)\times(\mathbf{r}_{\mathbf{n}2} + \mathbf{r}_{\mathbf{n}3})\beta_n \qquad (5.20)$$

$$\mathbf{m} = \frac{i}{k}\sqrt{\frac{\epsilon}{\mu}}\sum_{n=1}^N L_n(\mathbf{r}_n^{c-} - \mathbf{r}_n^{c+})\beta_n + \frac{1}{2}\sum_{n=1}^N (L_n/6)(p_n^+ - p_n^-)\times(\mathbf{r}_{\mathbf{n}2} + \mathbf{r}_{\mathbf{n}3})\alpha_n. \qquad (5.21)$$

Both the electric dipoles **p** arising from the effective magnetic currents as well as the magnetic dipoles **m** arising from the electric effective currents depend on the choice of origin. One of the potential advantages of the effective current approach over the VSH approach is that one can find the dipolar contributions of single scatterers in close proximity to other scatterers, for instance when examining the physics of multi-element plasmon antennas. Furthermore one can even envision that one could calculate the multipole moments for structures close to an interface or inside lossy environments, while this is certainly not possible with the VSH approach.

Polarizability tensor retrieval

For both the VSH retrieval method and the direct current-base retrieval method the electric dipole moment **p** and magnetic dipole moment **m** are retrieved given a particular incident field. Motivated by recent developments in the field of metamaterials, we propose to retrieve polarizability tensors that specify the response for *any* incident field, rather than induced moments for a particular incident field. We focus on objects with an electric and magnetic dipole response, which we expect to be fully captured by a 6×6 polarizability tensor[29]:

$$\begin{pmatrix} \mathbf{p} \\ \mathbf{m} \end{pmatrix} = \overline{\boldsymbol{\alpha}} \cdot \begin{pmatrix} \mathbf{E} \\ \mathbf{H} \end{pmatrix} = \begin{pmatrix} \overline{\boldsymbol{\alpha}}_E & \overline{\boldsymbol{\alpha}}_{EH} \\ \overline{\boldsymbol{\alpha}}_{HE} & \overline{\boldsymbol{\alpha}}_H \end{pmatrix} \cdot \begin{pmatrix} \mathbf{E} \\ \mathbf{H} \end{pmatrix} \tag{5.22}$$

In this tensor the upper diagonal 3×3 block $\bar{\alpha}_E$ is the usual electric polarizability tensor, while the lower diagonal block $\bar{\alpha}_H$ is the magnetic polarizability tensor. The off-diagonal blocks represent magnetoelectric response, i.e., the electric (magnetic) moment that might be induced through magnetic (electric) driving. This form of the polarizability tensor is commonly used in the field of bi-anisotropic and chiral media [30]. Evidently, one should choose six independent incident conditions, retrieve the induced moments, and apply matrix inversions to obtain

$$\overline{\boldsymbol{\alpha}} = \begin{pmatrix} \mathbf{p}_1 & \cdots & \mathbf{p}_6 \\ \mathbf{m}_1 & \cdots & \mathbf{m}_6 \end{pmatrix} \cdot \begin{pmatrix} \mathbf{E}_1^{inc} & \cdots & \mathbf{E}_6^{inc} \\ \mathbf{H}_1^{inc} & \cdots & \mathbf{H}_6^{inc} \end{pmatrix}^{-1} . \tag{5.23}$$

In our work we use as incidence conditions standing waves constructed as plane waves incident from opposing Cartesian directions. To construct six independent conditions we use the three Cartesian axes as incident directions, each with two orthogonal polarizations (also along the Cartesian axes). Due to the fact that SIE rigorously respects the linear superposition principle, this choice of incidence conditions is immaterial for the final result. Although this choice is entirely arbitrary it has the esthetic appeal of corresponding exactly to each one of the six Cartesian basis vectors used for the driving fields. As a final note on the retrieval protocol we add that the definition of origin that is chosen to refer the dipole moments to, is a nontrivial matter, due to the well-known dependence of electric and magnetic dipoles on the choice of origin (more precisely, both the contributions to the electric dipoles created by magnetic currents and to the magnetic dipoles created by electric currents depend on origin). We have

made use of the Onsager relations that the polarizability tensor has to fulfill due to reciprocity. Onsager relations in particular state that the upper diagonal and lower diagonal cross-polarizabilities are each other's negative transpose for purely dipolar scatterers. Accordingly, we choose the origin for both retrieval algorithms as the position for which the sum $|\overline{\alpha}_{EH} + \overline{\alpha}_{HE}|$ is minimum.

5.3 Benchmark of vector spherical harmonics and effective current density α-retrieval

In order to benchmark the SIE code and the retrieval of the polarizability tensor we consider an entirely known object, i.e., a Mie sphere. We focus on a sphere that has both a dielectric and magnetic response in order to benchmark both the electric and magnetic dipole retrieval. We compare to the rigorous theoretical values for electric and magnetic polarizability given by the Mie coefficients (labeled here as c_1^{TM} and c_1^{TE}) [31, 32]:

$$\overline{\alpha}_{\mathbf{E}} = -\frac{6\pi i \epsilon_0 c_1^{TM}}{k_0^3}\overline{\mathbf{I}}, \tag{5.24}$$

$$\overline{\alpha}_{\mathbf{H}} = -\frac{6\pi i c_1^{TE}}{k_0^3}\overline{\mathbf{I}}, \tag{5.25}$$

For our benchmark, we fix $\mu = 4$ and set ϵ equal to the dielectric constant of gold as tabulated by [33]. While these values do not represent any currently physically realizable object, these values allow to asses whether we can accurately separate electric and magnetic dipole moments. We use a fixed discretization of the sphere surface by 572 nodes composed of 1241 triangles. While the vertices of the mesh are exactly located on the assumed nano-particle radius of 10 nm, we note that the triangulated surface is entirely located *within* the assumed sphere. For this reason, SIE simulations effectively underestimate the sphere size, to a degree that reduces with increasing number of nodes. We quantify the effective radius by calculating the mean distance from the center of the sphere to the surface of the meshing triangles. For the particular meshing conditions used here, the effective radius is 9.96 nm, which we use in the Mie calculations to which we compare the SIE results. In Fig. 5.2 we plot the diagonal elements α_{Exx} and α_{Hyy} of the polarizability tensor over the wavelength range from 100 nm to 4000 nm. For both the vector spherical harmonic projection, and for the equivalent current retrieval there is an excellent correspondence between the retrieved dipole moments and the polarizabilities predicted by Eq. (5.24) and Eq. (5.25). The origin used for the retrieval was found to coincide with the center of the sphere, as expected based on symmetry. The error between the VSH retrieval procedure and the theoretical dipole moments is less than 0.1% throughout the whole wavelength range of the simulation. This agreement is only possible due to the precision of the discrete spherical harmonic transformation over the sphere on which the scattered field is collected (taken here to have radius of 10 μm), and of course also to the extremely

good convergence of the SIE method. Furthermore this almost perfect agreement to the theoretical values spans all the way to wavelengths equal to the diameter of the sphere. This agreement is hence beyond what is needed for metamaterial analysis where wavelengths around 5 to 10 times bigger than the structures are commonly used. When examining the current retrieval procedure we find that the error between the effective currents retrieval and the theoretical electric dipole moments is less than 0.006% at 4000 nm and grows monotonically up to 1% at 100 nm wavelength. For the magnetic dipole it is 0.03% at 4000 nm and 8.7% at 100 nm. The difference between the rigorous values and those extracted from the effective currents method is due to the fact that the current-to-dipole expression used in the current retrieval procedure (Eq. (5.16 and 5.17)) are only valid for $kr_{max} \ll 1$ as explained by Jackson [20]. These two equations, which are the equations commonly used in the metamaterial field [34–36], derive from exact formulae (9.167 and 9.168 in [20]) by replacing the involved spherical Bessel functions by their small-argument asymptotes. Therefore the effective current method is only expected to be accurate for $r \ll \lambda/2\pi$ (i.e. kr~1). The error is thus not a numerical error but an error due to a poorly met approximation. This error and whether it is larger for **p** than for **m** or vice versa, not only depends on the size of the scatterer but also on the specific weighting given by the current distribution. In contrast the VSH retrieval through fields is valid for arbitrary frequency and arbitrary size of the radiating object.

MatLab code for the VSH retrieval method can be found in our group webpage (http://www.amolf.nl/research/resonant-nanophotonics/), to be used with the fields calculated with any full wave Maxwell solver.
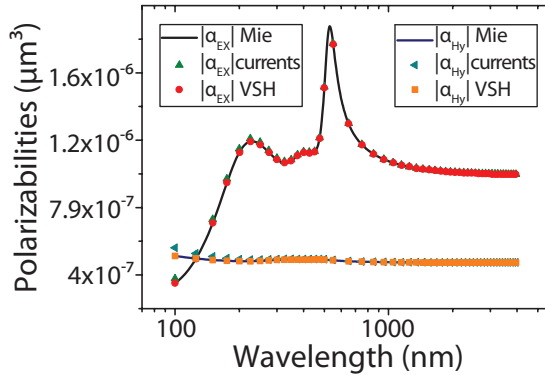
Figure 5.2: Magnitude of the electric and magnetic polarizabilities for a bead 10 nm radius, with $\epsilon = \epsilon_{Gold}$ and $\mu = 4$. The polarizabilities are calculated with a vector spherical harmonic expansion of the scattered fields (VSH), with the use of the effective currents (currents) and finally based on the theoretical Mie expansion of a sphere. The electrical polarizabilities are divided by $4\pi\epsilon_0$ while the magnetic polarizabilities are divided by 4π so as to have the dimensions of volume.

5.4 Polarizability retrieval applied to Kerker's paradox of zero-forward scattering spheres

As a more challenging benchmark we consider magnetoelectric spheres where material parameters are set to the very special condition that is the subject of Kerker's paradox raised in [1] and resolved in [2]. It was first noted by Kerker [1] that at a particular combination of ϵ and μ, spheres appear to have zero forward scattering, yet nonzero extinction. This apparent paradox that occurs for very small spheres when $\epsilon = (4 - \mu)/(2\mu + 1)$ gained new interest in the framework of cloaking and invisibility [37, 38]. Alú et. al. [2] showed that these spheres indeed have very low, yet nonzero forward scattering, thereby complying with the optical theorem. The almost zero forward scattering results from destructive interference in the forward direction of the radiation of the generated electric dipole and magnetic dipole moment. Here we reproduce three of the examples studied by Alú [2], using the SIE method (see Fig. 5.3) and retrieve the polarizability tensor. First, in Fig. 5.3 the bistatic scattering cross section or differential scattering efficiency is plotted for the spheres treated in [2]. The spheres have different radius a=λ/100, a=λ/20 and a=λ/4. The permeability of the three spheres is μ=3 while the permittivity is ϵ=0.143, ϵ=0.121 and ϵ=0.315. It should be noted that for larger spheres, the condition of minimal forward scattering is shifted away from the criterion $\epsilon = (4 - \mu)/(2\mu + 1)$. The calculated efficiencies are in excellent quantitative agreement with the values reported by Alú [2]. It is evident that the forward scattering for the

	a=λ/100	a=λ/20	a=λ/4
$\alpha_E[a^3]$	−4.985	−4.917+0.040i	−1.155+0.565i
$\alpha_H[a^3]$	4.990	4.928+0.040i	1.710+0.700i
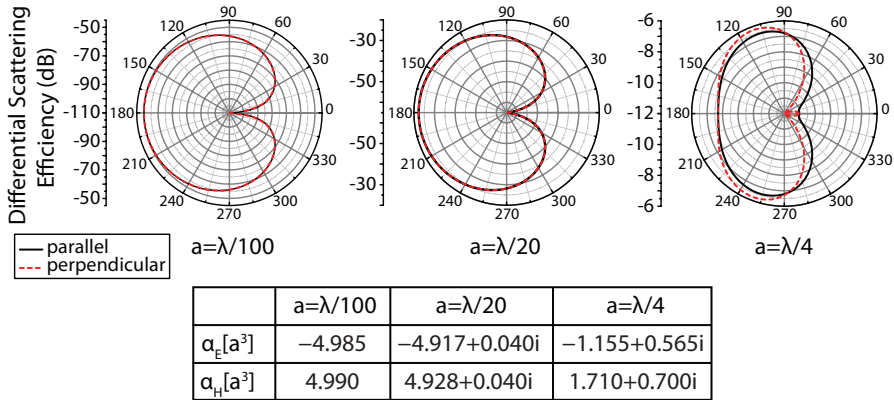
Figure 5.3: Differential scattering efficiency (bistatic scattering cross section/πa^2) for parallel and perpendicular scattered field form three different magneto electric spheres of radius 'a', as studied in [1]. The first sphere has an $\epsilon = 0.143$ and $\mu = 3$, the simulation is done at $\lambda = 100a$. The second sphere has an $\epsilon = 0.121$ and $\mu = 3$, the simulation is done at $\lambda = 20a$. The third sphere has an $\epsilon = 0.315$ and $\mu = 3$, the simulation is done at $\lambda = 4a$. The table shows the retrieved values of α expressed in units of a^3 for all three spheres, as extracted from the VSH method and expressed in units of the particle radius cubed.

three spheres is close to zero. We report as a table in Fig. 5.3b the retrieved values of α expressed in units of a^3 for all three cases, as extracted from the VSH method and expressed in units of the particle radius cubed. All off-diagonal elements are at least 10^5 times smaller than the diagonal elements, i.e., zero within numerical precision. The retrieved polarizabilities are isotropic to within 0.1%. We therefore only report the mean diagonal α_E and α_H. Evidently, for all three spheres the condition $\mathbf{p} = -\mathbf{m}$ required for complete destructive interference in the forward direction is almost met, consistent with the conclusion derived in [2] and [1] that this is a necessary condition for zero forward scattering. For increasing sphere size compared to the wavelength the imaginary part of the diagonal elements of the tensor increases due to radiation damping. For the largest sphere, $\mathbf{p}$ deviates noticeably from -$\mathbf{m}$, and forward scattering is noticeable.

This benchmark shows the usefulness of SIE to simulate magneto-electric scatterers with a very high precision, and suggests that the retrieved α-tensor can be used on more complex systems to gain insight into the problem beyond that usually obtained from just brute force calculations.

5.5 Conclusions

We have developed and benchmarked the SIE method to retrieve the polarizability tensor of scatterers. This retrieval is performed in two different ways. The first method consists of a vector spherical harmonics projection of the scattered fields, which yields an extremely good precision for any wavelength and size of the scatterer, thanks to the aid of a discrete harmonic transform on the sphere. With the second method, based on effective electric and magnetic surface currents, we can successfully retrieve the polarizabilities of small scatterers with the advantage that this retrieval can be done on non-isolated structures.

References

[1] M. Kerker, D.-S. Wang, and C. L. Giles, *Electromagnetic scattering by magnetic spheres*, J. Opt. Soc. Am. **73**, 765 (1983).

[2] A. Alù and N. Engheta, *How does zero forward-scattering in magnetodielectric nanoparticles comply with the optical theorem?*, J. Nanophot. **4**, 041590 (2010).

[3] W. L. Barnes, A. Dereux, and T. W. Ebbesen, *Surface plasmon subwavelength optics*, Nature **424**, 824 (2003).

[4] C. Sonnichsen, B. M. Reinhard, J. Liphardt, and A. P. Alivisatos, *A molecular ruler based on plasmon coupling of single gold and silver nanoparticles*, Nat. Biotechnol. **23**, 741 (2005).

[5] S. Lal, S. Link, and N. J. Halas, *Nano-optics from sensing to waveguiding*, Nat Photon **1**, 641 (2007).

[6] J. B. Lassiter, J. Aizpurua, L. I. Hernandez, D. W. Brandl, I. Romero, S. Lal, J. H. Hafner, P. Nordlander, and N. J. Halas, *Close encounters between two nanoshells*, Nano Letters **8**, 1212 (2008), PMID: 18345644.

[7] M. Rahmani, D. Y. Lei, V. Giannini, B. Lukiyanchuk, M. Ranjbar, T. Y. F. Liew, M. Hong, and S. A. Maier, *Subgroup decomposition of plasmonic resonances in hybrid oligomers: Modeling the resonance lineshape*, Nano Lett. **12**, 2101 (2012).

[8] C. L. Nehl, H. Liao, and J. H. Hafner, *Optical properties of star-shaped gold nanoparticles*, Nano Lett. **6**, 683 (2006).

[9] M. Hentschel, M. Saliba, R. Vogelgesang, H. Giessen, A. P. Alivisatos, and N. Liu, *Transition from isolated to collective modes in plasmonic oligomers*, Nano Letters **10**, 2721 (2010).

[10] G. Dolling, C. Enkrich, M. Wegener, J. F. Zhou, C. M. Soukoulis, and S. Linden, *Cut-wire pairs and plate pairs as magnetic atoms for optical metamaterials*, Opt. Lett. **30**, 3198 (2005).

[11] S. Zhang, Y.-S. Park, J. Li, X. Lu, W. Zhang, and X. Zhang, *Negative refractive index in chiral metamaterials*, Phys. Rev. Lett. **102**, 023901 (2009).

[12] N. Liu, H. Guo, L. Fu, S. Kaiser, H. Schweizer, and H. Giessen, *Three-dimensional photonic metamaterials at optical frequencies*, Nat Mater **7**, 31 (2008).

[13] N. Yu, F. Aieta, P. Genevet, M. A. Kats, Z. Gaburro, and F. Capasso, *A broadband, background-free quarter-wave plate based on plasmonic metasurfaces*, Nano Letters **12**, 6328 (2012).

[14] F. Aieta, P. Genevet, N. Yu, M. A. Kats, Z. Gaburro, and F. Capasso, *Out-of-plane reflection and refraction of light by anisotropic optical antenna metasurfaces with phase discontinuities*, Nano Letters **12**, 1702 (2012).

[15] A. Pors, M. G. Nielsen, R. L. Eriksen, and S. I. Bozhevolnyi, *Broadband focusing flat mirrors based on plasmonic gradient metasurfaces*, Nano Lett. **13**, 829 (2013).

[16] S. Mühlig, C. Menzel, C. Rockstuhl, and F. Lederer, *Multipole analysis of meta-atoms*, Metamaterials **5**, 64 (2011).

[17] K. Yee, *Numerical solution of initial boundary value problems involving maxwell's equations in isotropic media*, IEEE Trans. Antennas Prop. **14**, 302 (1966).

[18] G. H. Goedecke and S. G. O'Brien, *Scattering by irregular inhomogeneous particles via the digitized green's function algorithm*, Appl. Opt. **27**, 2431 (1988).

[19] F. J. Garcìa de Abajo and A. Howie, *Retarded field calculation of electron energy loss in inhomogeneous dielectrics*, Phys. Rev. B **65**, 115418 (2002).

[20] J. D. Jackson, *Classical Electrodynamics*, Wiley, New York, third edition, 1999.

[21] A. M. Kern and O. J. F. Martin, *Surface integral formulation for 3d simulations of plasmonic and high permittivity nanostructures*, J. Opt. Soc. Am. A **26**, 732 (2009).

[22] R. F. Harrington, *Field computation by method of moments*, MacMillan, 1968.

[23] S. Rao, D. Wilton, and A. Glisson, *Electromagnetic scattering by surfaces of arbitrary shape*, IEEE Trans. Antennas Prop. **30**, 409 (1982).

[24] C. Geuzaine and J.-F. Remacle.

[25] C. T. Tai, *Dyadic Green's Functions in Electromagnetic Theory*, IEEE Press, New York, second edition, 1993.

[26] M. J. Mohlenkamp, *A fast transform for spherical harmonics*, J. Fourier Anal. Appl. **5**, 159 (1999).

[27] J. Petschulat, J. Yang, C. Menzel, C. Rockstuhl, A. Chipouline, P. Lalanne, A. Tüennermann, F. Lederer, and T. Pertsch, *Understanding the electric and magneticresponse of isolated metaatoms by meansof a multipolar field decomposition*, Opt. Express **18**, 14454 (2010).

[28] A. Mohammadi, H. Nadgaran, and M. Agio, *Contour-path effective permittivities for the two-dimensional finite-difference time-domain method*, Opt. Express **13**, 10367 (2005).

[29] I. Sersic, C. Tuambilangana, T. Kampfrath, and A. F. Koenderink, *Magnetoelectric point scattering theory for metamaterial scatterers*, Phys. Rev. B **83**, 245102 (2011).

[30] I. Lindell, A. H. Sihvola, S. A. Tretyakov, and A. J. Viitanen, *Electromagnetic Waves in Chiral and Bi Isotropic Media*, Artech House, Norwood, MA, 1994.

[31] J. Li, A. Salandrino, and N. Engheta, *Shaping light beams in the nanometer scale: A yagi-uda nanoantenna in the optical domain*, Phys. Rev. B **76**, 245403 (2007).

[32] A. Alù and N. Engheta, *Achieving transparency with plasmonic and metamaterial coatings*, Phys. Rev. E **72**, 016623 (2005).

[33] P. G. Etchegoin, E. C. L. Ru, and M. Meyer, *An analytic model for the optical properties of gold*, The Journal of Chemical Physics **125**, 164705 (2006).

[34] N. Papasimakis, V. A. Fedotov, K. Marinov, and N. I. Zheludev, *Gyrotropy of a metamolecule: Wire on a torus*, Phys. Rev. Lett. **103**, 093901 (2009).

[35] T. Kaelberer, V. A. Fedotov, N. Papasimakis, D. P. Tsai, and N. I. Zheludev, *Toroidal dipolar response in a metamaterial*, Science **330**, 1510 (2010).

[36] Y.-W. Huang, W. T. Chen, P. C. Wu, V. Fedotov, V. Savinov, Y. Z. Ho, Y.-F. Chau, N. I. Zheludev, and D. P. Tsai, *Design of plasmonic toroidal metamaterials at optical frequencies*, Opt. Express **20**, 1760 (2012).

[37] R. V. Mehta, R. Patel, R. Desai, R. V. Upadhyay, and K. Parekh, *Experimental evidence of zero forward scattering by magnetic spheres*, Phys. Rev. Lett. **96**, 127402 (2006).

[38] B. García-Cámara, F. Moreno, F. González, and J. M. Saiz, *Comment on "experimental evidence of zero forward scattering by magnetic spheres"*, Phys. Rev. Lett. **98**, 179701 (2007).

6

Designing Antennas with the Aid of the Polarizability Retrieval Method

Based on the retrieval of the polarizability tensor discussed in chapter 5 we can understand the basic response of antennas in a more complete way than is possible by analyzing snapshots of near fields or surface currents. In order to demonstrate the ease with which this method can be used we report the polarizability tensor of split rings, and show that split rings will strongly influence emission of dipolar single emitters. We find that in the context of plasmon enhanced emission, split rings can impart their large magnetic dipole moment to the emission of simple electric dipole emitters. Finally, we present a split ring antenna array design that is capable of converting the emission of a single linear dipole emitter in forward and backward beams of directional emission of opposite handedness. This design can for instance find application in spin angular momentum encoding of quantum information.

6.1 Introduction

Metamaterials and 'metasurfaces' are engineered structures with properties that cannot be found in nature. These 'materials' and 'surfaces' have been designed to have extraordinary responses to incident fields e.g. negative refraction [1], pseudochirality [2] or in general an arbitrary phase and amplitude response to incident light. For all these structures their extraordinary response to incident light originates from the magnetoelectric polarizability of their constitutive elements, which essentially are optical nano antennas. In literature we find many examples for such scatterers, ranging from single metallic rod nano antennas, to V-shaped metal particles [3, 4],

large dielectric objects [5], and split ring resonators [6]. Split rings have drawn a considerable amount of attention due to their strong magneto electric response, and their possible application for cloaking [7] and enantiomeric discrimination of molecules [2, 8]. Several workers have argued that split rings should be viewed either as an electric plus a magnetic dipole each with a polarizability [9], or as a cross-coupled object that also has a magneto-electric response [10]. By applying the polarizability retrieval method developed in chapter 5 to, among other objects, split rings, we retrieve exciting insights regarding the electric and magnetic response of split rings. We show that split rings are strongly magneto-electric, implying that a large magnetic dipole moment is most easily induced by electric driving. The particular phase relation between the electric, magnetic and magneto-electric polarizability further implies record-high per-building block optical activity in extinction and scattering. We show that the insights gained from the polarizability tensor can be used to construct new types of plasmonic array antennas that have the directivity of Yagi-Uda antennas [11, 12], but with unique polarization properties. In particular we show how metamaterial antennas allow control over the magnetic dipole content of emission, and over the handedness of emitted light. On basis of this type of control over emission we envision applications in control of magnetic dipole emitters [13], directionality of single dipole emission [14], photon spin angular momentum encoding in single photon sources, and enantioselective spectroscopies that employ near-field enhancement of chirality.

This chapter is organized as follows. In section 6.2 we discuss the polarizability of split rings. In section 6.4 and 6.5 we demonstrate how, on basis of the extracted polarizability, split rings can be used for rational design of antennas for emission control.

6.2 LC model for split rings

In the metamaterial community the performance of a material is usually quantified through effective responses ϵ and μ. However the fundamental parameter underlying the effective ϵ and μ is the α-tensor of the metamaterial building block, which is much less frequently studied. Here we use the benchmarked code of chapter 5 to understand split rings. Extensive literature has been devoted to explain the response of this structure [2, 6, 15] in terms of LC resonators. Fig. 6.1 a shows a sketch of an LC resonator circuit. The basic ideas behind the split ring are that it can be driven by an incident magnetic field **H** that points through the loop, that circulating current in the ring will correspond to a magnetic dipole, and finally that the current is strongly enhanced by generating an LC resonance using the split as capacitor. Thus it should have the basic property that it has a magnetic dipole polarizability in response to magnetic fields. However, note that a circulating current will pile up as charge at the capacitor, meaning that an electric dipole response is inextricably linked to the magnetic response. The equation of motion for the current in this type of circuit with external driving is:

$$L\frac{dI(t)}{dt} + \frac{q(t)}{C} = E_{\mathrm{drv}}\mathrm{d} + A\frac{dH_{\mathrm{drv}}}{dt},$$ (6.1)
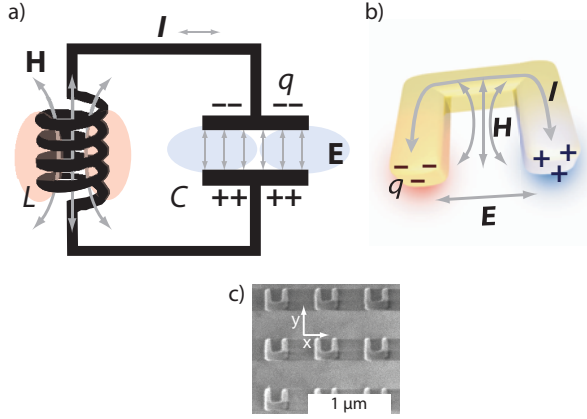
Figure 6.1: Figures a) and b) show a comparison between an LC circuit and a split ring resonator. c) shows a SEM picture of an array of split ring resonators which work at near infrared frequencies. Picture courtesy of Ivana Seršic

where L is the inductance, $I(t)$ is the time dependent current, $q(t)$ is the time dependent charge, C is the capacitance, E_{drv} is the magnitude of the driving electric field along the capacitor gap, d is the distance of the gap between the capacitor plates, A is the effective area of the inductor and H_{drv} is the driving magnetic field which flux drives a current along the inductor.

The LC-circuit has often been used to describe the scattering of split rings. The main important predictions for polarizability that it represents are the following. First, the LC circuit is expected to have a Lorentzian resonance line shared among all tensor elements. Second, the LC circuit will respond only to electric fields along the gap direction x, and magnetic fields oriented through the ring (z) . Third, the response will involve an induced electric dipole moment $p = qd$ solely along x and a magnetic moment $m = AI$ solely along z. Fourth, the fact that $I = \dot{q}$ imposes a relation between p and m, which means that it is not trivial to independently control either the magnitude, or the phase between p and m. Fifth, the driving side of the LC equation shows that both p and m will be driven by both **E** and **H**. That means there must be cross coupling, known in the field as "bi-anisotropy" or "magneto-electric coupling". Finally, it should be noted that the off-diagonal polarizabilities will be a quarter cycle out of phase with the diagonal elements, as embodied in the d/dt in Faraday's law, and in the relation $m \sim I = \dot{q} \sim \dot{p}$.

To summarize these findings from the LC circuit, we would expect the polarizability tensor to have the following form

$$\begin{bmatrix} \mathbf{p} \\ \mathbf{m} \end{bmatrix} = \mathscr{L}(\omega) \begin{bmatrix} \alpha_E & \alpha_{EH} \\ \alpha_{HE} & \alpha_H \end{bmatrix} \cdot \begin{bmatrix} \mathbf{E} \\ \mathbf{H} \end{bmatrix}. \tag{6.2}$$

Note that this form satisfies a set of general constraints known as Onsager constraints.

The Onsager constraints require that $\alpha_E = \alpha_E^T$, $\alpha_H = \alpha_H^T$ and $\alpha_{HE} = -\alpha_{EH}^T$ (See Ref. [10]). Any violation of these constraints would mean that the scatterer violates reciprocity. A further observation is that if you evaluate Eq. 6.1 for polarizability then α_E and α_H turn out to be real and α_{EH} and α_{HE} turn out to be imaginary, with values given by geometry. In other words there is a quarter wave phase offset for the off-diagonal elements. This is also a fundamental requirement, as otherwise energy conservation would be violated.

6.3   Retrieved polarizability tensor of split rings

Here we report the full polarizability tensor of split rings resonant at 1.5 μm as retrieved from full wave SIE calculations using the methods of chapter 5. We consider a gold split ring with dimensions of 30 nm height, 200 nm length and 200 nm width with a central hole of 140 nm by 80 nm. A SEM picture of a fabricated array of such split rings is shown in Fig. 6.1c. In our simulation the split ring is placed in a homogeneous environment with $\epsilon = 1$ and $\mu = 1$ and the surface discretization used consists of 774 nodes. Fig. 6.2a reports the total scattering cross section upon excitation by a plane wave with polarization of the electrical field in the x direction and **k** vector directed in the negative z direction. The response of the split ring presents two resonant peaks in the wavelength range studied i.e. from 400 nm to 1700 nm. The first resonance is centered around 1544 nm with a width of 124 nm and the second resonance is centered at 689 nm with a width of 44 nm, in excellent agreement with experiment and FDTD simulations [16]. The first resonant peak is also called the LC resonance as described in Ref. [16]. This resonance has a calculated maximum total scattering cross section of 0.13 μm^3 very well in agreement with measured data, that show an extinction cross section of 0.3 μm^3 at an albedo of 30% [16, 17]. We focus on this fundamental resonance and its scattering characteristics, choosing the wavelength of 1544 nm for the retrieval of the polarizability tensor. At the split ring resonance, the quadrupolar terms contribute less than 2% to the total extinction. Therefore, here we disregard any higher multipolar terms. The center used for the retrieval was found at the point where magnetic moments created by electric fields and the electric moments created by magnetic fields are the negative of each other. This condition arises from Onsager relations [2]. This center is -25 nm from the geometrical center in the y direction. i.e. closer to the base of the split ring. The SIE dipole polarizability retrieval procedure allows us to quantify both the diagonal values in the polarizability tensor as well as the cross-coupling between the magnetic and electric moments. We find the following

values for the VSH and effective current retrieval procedures

Elements of α	VSH	Eff. Currents	
$\alpha_{E_x}/(4\pi V \epsilon_0)$	$-1.38 + 10.47i$	$0.32 + 10.87i$	
$\alpha_{E_y}/(4\pi V \epsilon_0)$	$1.52 + 0.10i$	$1.53 + 0.10i$	
$\alpha_{E_z}/(4\pi V \epsilon_0)$	$0.11i$	0.12	
$\alpha_{EH_{xz}}/(4\pi V/c)$	$-2.83 - 0.41i$	$-2.92 + 0.04i$	(6.3)
$\alpha_{HE_{zx}}/(4\pi V/Z)$	$2.85 + 0.48i$	$2.92 - 0.00i$	
$\alpha_{H_x}/(4\pi V)$	$-0.01i$	-0.01	
$\alpha_{H_y}/(4\pi V)$	0	0	
$\alpha_{H_z}/(4\pi V)$	$-0.15 + 0.78i$	$-0.02 + 0.79i$	

where V denotes the geometrical volume of the split ring $V = 6.33 \times 10^{-4} \mu m^3$. All the other values in the polarizability tensor are 10^{-3} below α_{E_x}. Both the VSH and the effective currents retrieval procedures indicate that the scatterer has a magneto electric nature given the values of the magnetic and cross polarizabilities. The difference in magnitude between both retrieval procedures is maximally 16%. Based on Mie calculations (Chapter 5) we already saw that the VSH retrieval procedure is accurate, whereas the common current-based definition is fundamentally limited and only valid for small objects of size r$< \lambda/2\pi$. This condition is not met for the split ring. Therefore we will focus now on the values retrieved with the VSH procedure. The electric polarizability for the p_x oriented dipole α_{E_x} is the largest polarizability in this structure, and is well in excess of the physical particle volume. Thereby the split ring is very much like a strongly plasmonic particle. That the retrieved α_{E_x} is mostly imaginary confirms that $\lambda =$1544 nm corresponds to resonant driving. The magnetic polarizability for the m_z oriented dipole α_{H_z} is 13 times smaller than the electric polarizability. The off-diagonal values $\alpha_{EH_{xz}}$ and $\alpha_{HE_{zx}}$ significantly exceed the magnetic polarizability. We note that the retrieval very well confirms fundamental constraints on the cross polarizabilities. In particular, the cross polarizabilities are the negative of each other to within 2%, as fundamentally expected from Onsager relations. Also the phase relations $\arg(\alpha_{EH_{xz}}/\alpha_{E_x}) = \pi/2$ and $\arg(\alpha_{H_z}/\alpha_{E_x}) = 0$ are satisfied to within 0.06 rad. These phase relations are consistent with the LC-circuit intuition that if a magnetic response arises through electric driving, i.e., through cross polarizability, it must lag by a quarter wave, as it is due to relaxation of the charge that accumulates in response to $\mathbf{E}$ across the capacitor. Finally, we note that $\alpha_{HE_{zx}}=i\sqrt{\alpha_{H_z}\alpha_{E_x}}$ to within 0.4%. The numerical values that we retrieve are in reasonable accordance with experimentally retrieved values [2], which were reported to be approximately $|\alpha_{E_x}| = 6.4V$, $|\alpha_{H_z}| = 0.9V$ and $\alpha_{HE_{zx}} = 2.1V$. That the split ring in our model is comparatively even less magnetic than extracted in experiment is likely due to either one of two causes. First, the split ring resonator (SRR) response depend sensitively on geometrical details such as the exact gap size and the rounding assumed for approximating the SRR shape. The SRR that we model is comparatively thin and rounded compared to the SRRs in experiment. Secondly, in the experiments the polarizability was retrieved rather indirectly, from comparison of SRR array transmission to a lattice summation model. The fact that SRRs were located at an air-glass interface was disregarded. At a dielectric interface,
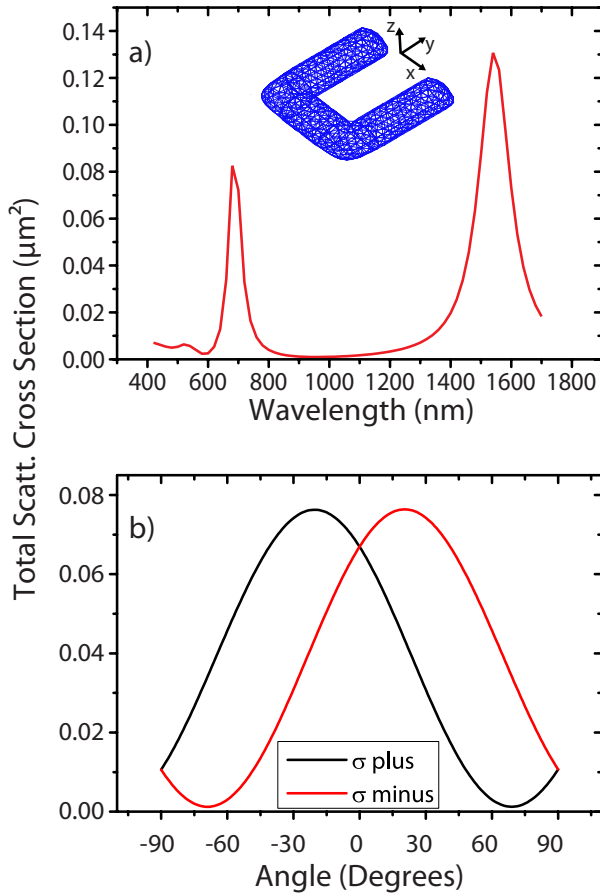
Figure 6.2: a) Total Scattering cross section of a split ring with width=200 nm, length=200 nm, height=30 nm and an inner hole of 80×140 nm. The inset shows a model of the split ring used. b) Total Scattering cross section of a split ring for different angles of incidence of circularly polarized light with right-handed polarization $\sigma+$ and left-handed polarization $\sigma-$.

polarizabilities can be significantly renormalized [18].

Optical activity

As mentioned earlier optical activity or pseudo-chirality is expected to exist in every antenna with a cross-coupled term in the polarizability tensor [2]. This can be seen from the following example. Suppose we have a structure with a polarizability tensor

α which defines the response of the particle as in:

$$\begin{bmatrix} p_x \\ m_z \end{bmatrix} = \mathscr{L}(\omega) \begin{bmatrix} \alpha_E & i\alpha_C \\ -i\alpha_C & \alpha_H \end{bmatrix} \cdot \begin{bmatrix} E_x \\ H_z \end{bmatrix} \tag{6.4}$$

The eigenvectors of this tensor are:

$$\begin{bmatrix} E_1 \\ H_1 \end{bmatrix} = \begin{bmatrix} -i(\alpha_H - \alpha_E + \sqrt{4\alpha_C^2 + (\alpha_E - \alpha_H)^2})/(2\alpha_C) \\ 1 \end{bmatrix} \tag{6.5}$$

and

$$\begin{bmatrix} E_2 \\ H_2 \end{bmatrix} = \begin{bmatrix} i(\alpha_E - \alpha_H + \sqrt{4\alpha_C^2 + (\alpha_E - \alpha_H)^2})/(2\alpha_C) \\ 1 \end{bmatrix} \tag{6.6}$$

which define a minimum and a maximum strength of the structure's response given by the eigenvalues

$$\alpha_1 = (1/2)\mathscr{L}(\omega)(\alpha_E + \alpha_H - \sqrt{4\alpha_C^2 + (\alpha_E - \alpha_H)^2}) \text{ and} \tag{6.7a}$$

$$\alpha_2 = (1/2)\mathscr{L}(\omega)(\alpha_E + \alpha_H + \sqrt{4\alpha_C^2 + (\alpha_E - \alpha_H)^2}). \tag{6.7b}$$

For a non vanishing α_C we see that the right eigenvectors present a phase delay between **E** and **H**, evident from the fact that the arguments of E and H are different. This phase delay can be approximately met by using circularly polarized light under an oblique incident condition. A change in the handedness in the circular polarization, even under the same incident angle, would change the response of the structure, as seen in the right eigenvalues and eigenvectors. This is a form of optical activity, specifically circular dichroism in extinction. Note that in this formulation there also evidently is a degree of maximum cross coupling. If $\alpha_C > \sqrt{\alpha_H \alpha_E}$, the extinction corresponding to the smallest eigenvalue will flip sign, meaning an unphysical negative cross section. This would only be possible if there would be gain in the system and is hence unphysical.

Now we turn to the full wave SIE calculations for split rings. Fig. 6.2b shows the extinction cross section for left-handed and right-handed illumination as a function of incident angle, for a wavelength of 1544 nm (i.e., on resonance). Fig. 6.2b indeed shows a strong optical activity for the split ring, as evidenced from the change of scattering cross section for right- and left-handed circularly polarized excitations at different incident angles. In order to compare the split-ring to other antennas with reported magnetic responses, we show in Fig. 6.3 the calculated optical activity for different metamaterial antennas. The data used to compare them comes from our VSH retrieval method and from measurements performed by Ivana Seršic and Marie Anne van de Haar in Ref. [2]. This retrieval is applied on archetypical metamaterial scatterers as shown in Fig. 6.3a, which are essentially split rings, Omega particles, and nested split rings. Given that the Omega particles have a very clearly defined symmetry center, we use the polarizability retrieval on these structures to verify that the Onsager constraints are satisfied. We calculate scattering cross sections and polarizability tensors in the
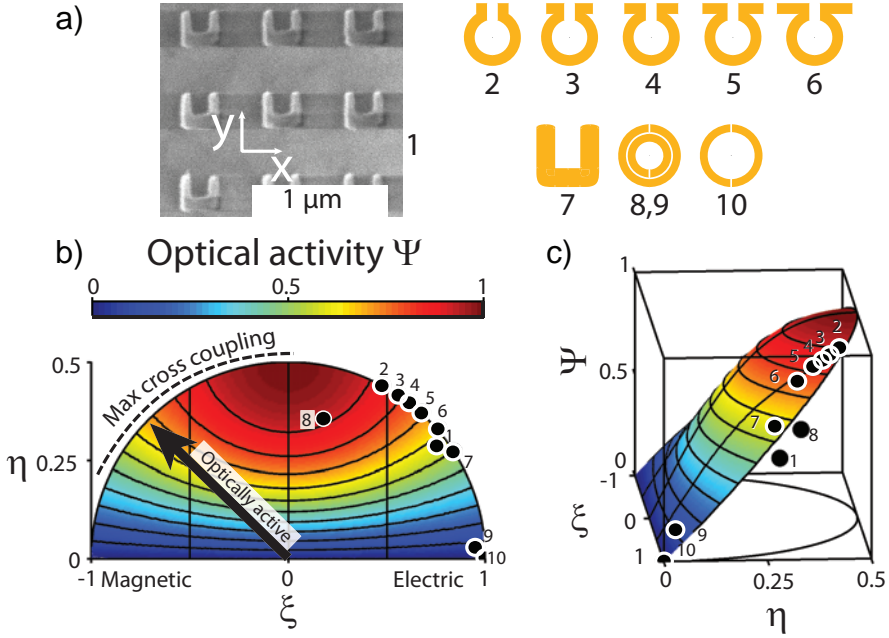
Figure 6.3: Master diagrams summarizing optical activity and bi-anisotropy mapped as a function of $\xi = (\alpha_E - \alpha_H)/((\alpha_E + \alpha_H)$ and $\eta = (\alpha_C)/((\alpha_E + \alpha_H)$. All structures we tested, numbered as in panel a), are close to the locus of maximum cross coupling (ellipse), except (8). The color scale shows optical activity contrast Ψ, in the dipole approximation (color scale) and for tested structures (dots). Panel c) is a 3D representation of b).

same way as we did for the split ring which in this case is represented by the structure number 7 in Fig. 6.3.

In order to allow a comparison of scatterers independent of their size we summarize the results for the retrieved polarizabilities and scattering cross sections in a 'master plot'. The scatterers are shown in Fig. 6.3a. As a first variable we use $\xi = (\alpha_E - \alpha_H)/(\alpha_E + \alpha_H)$, which is dimensionless and equals $+1$ for purely electric scatterers, -1 for purely magnetic scatterers, and 0 for equal electric and magnetic polarizability. As a second variable we use the cross coupling and normalize it to the electric and magnetic polarizabilities i.e. $\eta = \alpha_C/(\alpha_E + \alpha_H)$. The location of maximum cross coupling is the ellipse $\eta = \sqrt{1-\xi^2}/2$. Almost all metamaterial scatterers we analyzed have ξ far from 1 as shown in Fig. 6.3, indicating significant magnetic polarizability. Furthermore all particles lie essentially on the boundary of the ellipse, demonstrating that all the scatterers present maximum cross coupling. This is a strong indication that bianisotropy is ubiquitous as claimed in Ref. [2]. If one considers the LC model, it is in fact evident that since p and m derive from the same circulating charge, there is little room to independently engineer α_E, α_H and α_C by variation of geometrical parameters.

Explicitly, calculation shows that the LC model always results in $\alpha_C = \sqrt{\alpha_E \alpha_H}$, i.e., maximum cross coupling.

The measure of optical activity for these scatterers is presented as a third axis for the master plot. In order to quantify the optical activity we use the scattering cross section for right $\sigma_R(\theta)$ and left $\sigma_L(\theta)$ handed polarized light. The parameter that we use for this quantification is $\Psi = |\sigma_R(\theta) - \sigma_L(\theta)|/(\sigma_R(\theta) + \sigma_L(\theta)))$ evaluated at incidence angle $\theta = 45°$. This parameter has the merit of allowing us to quantify the maximum attained difference in extinction which is always maximal at 45° and also of being dimensionless so that we can compare all the scatterers regardless of their size. The colored surface in Fig. 6.3b shows Ψ versus ξ and η as predicted by point scattering theory. Optical activity is expected to be absent for zero cross coupling, and to increase monotonically as cross coupling increases. From point dipole theory we expect a very strong contrast in extinction for right and left polarized light along most of the ellipse that defines maximum cross coupling. This contrast should vanish only for purely electric ($\xi = 1$), and purely magnetic ($\xi = -1$)dipole scatterers. Our simulations in SIE show that all the calculated metamaterial scatterers exhibit strong optical activity in very good agreement with the dipole model. The only object that does not show maximum cross coupling is the nested split ring that has two resonances, formed by hybridization of the resonance in each ring. The fact that this object has a resonance with bi-anisotropy smaller than the maximum cross coupling value is due to the fact that it cannot be described as a single LC resonator. When multiple resonances are combined, partial cancelation of bi-anisotropy is possible.

6.4   Single split ring as a magnetic dipole converter

One of the most exciting features of plasmonic antennas is that since the plasmons are a combined oscillation of the optical fields and the free electrons in the metal, its resonances can be confined to very small modal volumes [19]. These small modal volumes make plasmonic antennas perfect candidates for coupling to single emitters since near fields and LDOS are enhanced [20]. Some of the functionalities that have been already experimentally proven for single emitters coupled to these antennas are change of polarization of the emitted field by using rod antennas [21] and directionality in the emission of the emitter through the use of Yagi-Uda antennas [22]. We present calculations of the interaction between a single emitter and a split ring resonator.

A technical issue is that the field of a dipolar source driving the scatterer is singular at the position of the emitter. Therefore unless a very fine discretization is used simulations are prone to big numerical errors. This holds for virtually any brute force method. In the case of SIE this problem occurs when calculating the values of the projection of the electric and magnetic fields over the discretized surface of our scatterer as is done for calculating q (see Eq. (5.10)) for fields stemming from a dipole in close vicinity to the scatterer. However since the field of the dipole source is given by the Green's function of the environment, we can follow a similar procedure to Eq. (5.11 and 5.12), in which the integral over $\overline{\mathbf{G}}(\mathbf{r}, \mathbf{r}_0)$ is separated into a smooth $\overline{\mathbf{G}}(\mathbf{r}, \mathbf{r}_0)_S$ and

singular part $\overline{\mathbf{G}}(\mathbf{r}, \mathbf{r}_0)_{NS}$, leading to the following equation for q:

$$q = \begin{cases} \int_{S_m} dS(\omega^2 \mu \mu_0)(\overline{\mathbf{G}}(\mathbf{r}_0, \mathbf{r})_S + \overline{\mathbf{G}}(\mathbf{r}_0, \mathbf{r})_{NS}) \cdot \mathbf{f}_m(\mathbf{r}) \cdot \mathbf{p} & : m = 1....N \\ \int_{S_{m-N}} dS(i\omega)(\nabla(G(\mathbf{r}_0, \mathbf{r})_S + G(\mathbf{r}_0, \mathbf{r})_{NS})) \times \mathbf{f}_{m-N}(\mathbf{r})) \cdot \mathbf{p} & : m = N+1....2N \end{cases}$$

(6.8)

where we used Eq. (5.10) and the facts that $\overline{\mathbf{G}}(\mathbf{r}, \mathbf{r}')^T = \overline{\mathbf{G}}(\mathbf{r}', \mathbf{r})$ and $(\nabla \times \overline{\mathbf{G}}(\mathbf{r}, \mathbf{r}'))^T = -\nabla \times \overline{\mathbf{G}}(\mathbf{r}', \mathbf{r})$ for the free space Green's function [23], and the identity $\nabla \times \overline{\mathbf{G}}(\mathbf{r}_0, \mathbf{r}) = \nabla G(\mathbf{r}_0, \mathbf{r}) \times \overline{\mathbf{1}}$ (Eq. (28) in Ref. [24]). The smooth part can be calculated with a normal quadrature routine. The singular part can be calculated by using the integration of the RWG function found in Ref. [25], i.e. by

$$q_{NS} = \begin{cases} \int_{S_m} dS(\omega^2 \mu \mu_0)((\frac{3L_n}{8\pi k_i^2}[\frac{1}{A_n^+}(\frac{k_i^2}{2}\mathbf{K}_3^1(T_n^+) - \mathbf{K}_3^{-1}(T_n^+))... \\ -\frac{1}{A_n^-}(\frac{k_i^2}{2}\mathbf{K}_3^1(T_n^-) - \mathbf{K}_3^{-1}(T_n^-))])... \\ +(\frac{1}{4\pi}[\mathbf{K}_2^{-1}(S_n) - \frac{k_i^2}{2}\mathbf{K}_2^1(S_n)])) \cdot \mathbf{p} & : m = 1....N \\ \int_{S_{m-N}} dS(i\omega)(\frac{1}{4\pi}[\mathbf{K}_4^{-1}(S_{m-N}) - \frac{k_i^2}{2}\mathbf{K}_4^1(S_{m-N})]) \cdot \mathbf{p} & : m = N+1....2N, \end{cases}$$

(6.9)

where $\mathbf{K}_j^l(T_n)$ are the integrals defined in Ref. [25] which are performed over the triangle T_n or over the surface S_n linked to the triangle with the same index. After having found q, we find the strength of the current densities $\mathbf{J}$ and $\mathbf{M}$ by finding α_n and β_n as already explained in chapter 5. It is important to notice that this same procedure can be used to find the scattered field at the source and thereby the local density of states [26] when using SIE, avoiding common problems encountered when working with the fields from a dipolar emitter close to scattering structures.

We performed simulations of an electric dipolar emitter located at different distances to the split ring and also at a fixed position in the middle of the split ring for different orientations of the emitter. Fig. 6.4a shows the calculated electric and magnetic dipole moments found from just the scattered field of the split ring for different distances of the emitter to the center of the split ring. In other words we calculate the *induced* dipole moments in the antenna. The induced electric dipole is given in units of the emitter dipole strength (p_0), while the units of the magnetic dipole are given in terms of $p_0 c$. With this choice of units we can compare the magnetic and electric dipoles directly, since the magnitude of the radiated power produced by an electric dipole with strength p_0 is the same as the one generated by a magnetic dipole with strength $p_0 c$. Fig. 6.4a shows that when the dipole is far from the split ring the induced dipole is fairly weak. Therefore the total system emits only with an electric dipolar nature given by the emitter itself. As the emitter gets closer to the split ring to within 230 nm, the total electric dipole moment of the system increases to exceed that of just the emitter, as expected for a high local density of states position near a plasmonic structure. Furthermore the nature of the lumped system starts to acquire a magnetic character to the point that 30% of the emission is of magnetic nature. In the bottom part of the graph we see that the phase of the driven electric dipole when the emitter is in close proximity to the split ring (50 nm from the geometrical center of the split ring) is delayed $\pi/2$ as expected
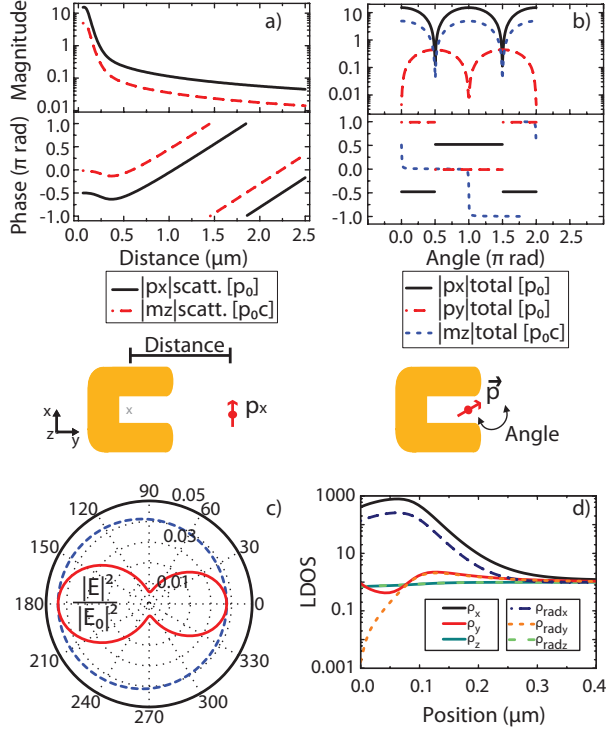
Figure 6.4: Single emitter in the vicinity of a split ring. In a) we show the calculated dipolar moment of the scattered field for different distances to the split ring center. In b) we show the dipolar moment of the total field (scattered field plus single emitter field) for different orientation angles of the single emitter in a position 0.05 μm from the center of the split ring. The angles are rotated around the z axis, therefore, we show the x and y electric dipole as well as the z magnetic dipole. The other components of the electric as well as the magnetic dipole are negligible in magnitude. In c) we show the scattered field pattern of a split ring excited with an electric dipolar emitter at the position on maximum coupling. The electric field magnitude $|E|^2$ is calculated at a radius 100 μm from the center of the split ring. The red continuous line shows the field in the plane 'xy' and the blue dashed line shows the field in the plane 'yz'. In d) we show the calculation of the normalized total and radiative LDOS for different positions in a line along the y axis through the center of the splitring.

for a structure driven on resonance. On the other hand the magnetic dipole is in phase with the driving emitter, $\pi/2$ advanced with respect to the induced electric dipole. This is expected from Ref. [10] since $\alpha_{EH} = -i\sqrt{\alpha_E \alpha_H}$ in the polarizability tensor of a split ring.

In a subsequent calculation we have placed the electric dipolar emitter at the position of maximum radiative LDOS i.e. 0.05 μm from the center of the split ring, and we varied the orientation of the dipole. From the total scattered plus emitted

field of the lumped system we calculate the effective dipole moments of the complete system. Fig. 6.4b shows the electric and magnetic dipole moments as a function of the orientation of the electric emitter, where the emitter orientation is rotated around the z axis that points through the split ring plane. It is evident that the coupling to the structure only occurs for the x component of the dipole, i.e., when p_x from the emitter couples to α_{E_x} of the split ring. The maximum total electric and magnetic dipole moment occurs when the dipolar emitter is aligned with the x axis. For this alignment, $p_y < 0.005 \, p_0$ is essentially zero, while $p_x = 15.1 \, p_0$ and $m_z = 4.9 \, p_0 c$. This result is commensurate with the relative magnitude of the purely electric and cross coupled polarizability of the split ring in Eq. (6.3), indicating that the dipolar scattering approximation of the split ring can be used for dipolar emitter excitations while still obtaining an agreement of 85% with the full wave calculation. It is important to notice that this agreement is dependent on the distance of the emitter to the split ring, since dipolar emitters in close proximity to a plasmonic structure (typically <20 nm) can increasingly excite higher multipolar moments of the plasmonic structures due to the strong gradients in the exciting fields [27]. When the dipolar emitter is aligned with the y axis, i.e., rotation angle $\pi/2$ then $p_y = 0.44 \, p_0$, $p_x = 0.12 \, p_0$ and $m_z = 0.04 \, p_0 c$. This result indicates, first, that p_y hardly induces a magnetic dipole and second that this position has a local density of states for y oriented dipoles lower than free space. Fig. 6.4c shows a polar plot of the far field intensity distribution of the scattered field for a split ring, excited with a dipole located at the position of maximum coupling and aligned along the gap of the split ring i.e. along the x direction. The $|E|^2$ distribution is evidently different to that of an electric dipole, since on the one hand the emission is asymmetric in the y axis due to the front-to-back asymmetry of the split ring, and on the other hand the emission in the x axis is different than zero, evidencing the partial magnetic nature of the scatterer. Finally in Fig. 6.4d we show the calculated total and radiative LDOS normalized to the vacuum LDOS. The calculations are done for different positions on the y axis along a line which starts at the center of the split ring. The maximum total and radiative LDOS occurs at a position ~50 nm away from the center of the split ring. While at this position the total LDOS for an x oriented dipole is ~755 ρ_0 the radiative LDOS for an x oriented dipole is ~252.7 ρ_0. This radiative LDOS is consistent with the generated total electric dipolar moment of 15.1 p_0 and magnetic moment of 4.9 $p_0 c$ for the lumped system. These values for the dipole moments indicate a radiative LDOS enhancement of $(p^2 + m^2)/p_0^2 = 252$. The fact that the total LDOS is 3 times the radiative LDOS is consistent with experimental measurements of the albedo of ~30% measured for a single Au split ring by Husnik et. al. [17]. The relative magnitude of the total vs. radiative LDOS indicates that the quantum efficiency of the system is η ~33% equal to the albedo of the split ring.
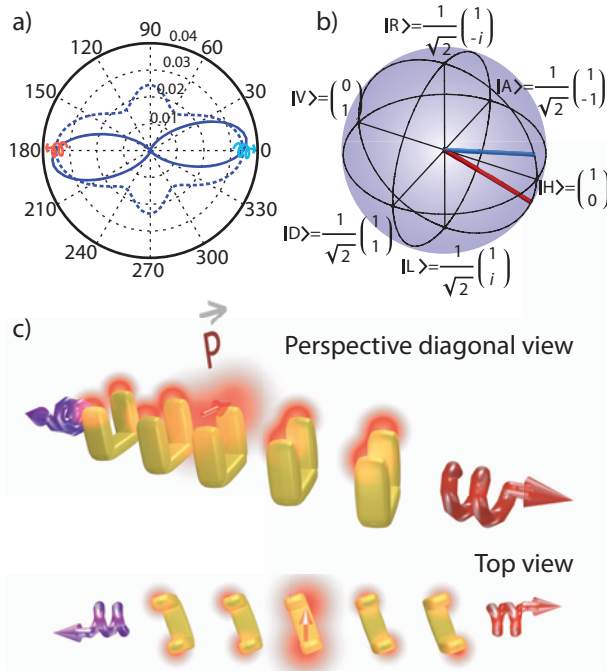
6.5   Split ring array antenna

Having understood the split ring as a system composed of an electric and a magnetic coupled dipole moment whose maximal response to circularly polarized plane waves

occurs for a certain polar angle θ_{MAX}, and having studied the way electric dipoles couple to single split rings we turn to the design of an array of split rings and to the study of the special properties that arise from it. In our design we combine *two* of our earlier results. Firstly, Fig. 6.2 shows that the purest handed response is obtained at off-normal incidence of 20°. Secondly, excitation of a split ring array with a single molecule is most advantageous when placed 50 nm from the geometrical center and with a dipolar orientation along the gap. In addition we know from Ref. [11, 12, 22, 28] that one can attain directionality in the scattering of arrays of particles by placing them in a linear array with a pitch of $\sim \lambda/3$. Our design combines these three ideas in an array of 5 split rings tilted at θ_{MAX} and excited by a dipolar emitter in the central element. Figure 6.5a presents the scattering pattern of the antenna which clearly shows directivity in its scattering, with scattered fields confined in a half angle $< 40°$. By studying the complex fields obtained from the front and back scattering from the antenna we can retrieve the polarization and plot it on the Poincare sphere, see Fig. 6.5b. We find right handed elliptically polarized light emanating from the front of the antenna (depicted by the blue point in Fig. 6.5(a and b)) and left handed elliptically polarized light emanating from the back of the antenna. Both fields have an electric field 7 times stronger in the x direction than in the y direction and the major axis of the ellipse is aligned with the x axis. Thereby, metamaterial antennas allow new forms of control over emission compared to plasmon antennas. We foresee that with split rings with a stronger magnetic polarizability term, it would be possible to reach a totally circular polarized light regime. Reaching stronger magnetic polarizability currently seems easiest at mid-infra-red and microwave frequencies [2]. We foresee interesting applications especially if one can reach this at optical frequencies. In this regime one could envision using split ring antennas to generate a single photon source from a simple linear electric dipole emitter, or from a localized $\chi^{(2)}$ nonlinear material that emits its photons in handed beams, or split in two narrow beams, where handedness and direction are entangled.

6.6 Conclusions

We have made use of the polarizability tensor retrieval method to calculate the α tensor of split rings. This method allows us to confirm that these type of planar scatterers can be described excellently by an LC circuit model, where the α tensor must have maximally strong cross coupling. It also lets us confirm and quantify the strong response in the $\boldsymbol{\alpha}_{EH}$ cross-coupled polarizability elements. This cross-coupled response implies that the structure possess optical activity. We have used the lumped system of a dipolar emitter and a split ring to show how the radiation nature of the system changes drastically from a simple electrical dipole emitter. In the lumped system the emission is modified by the scattering of the split ring, which can imprint its magneto-electric nature on the emission. This realization further extends current research efforts that have shown how emission from a single electric dipole transition in a quantum dot can appear as if it originates from a multipole transition by strong coupling of the emitter to

Figure 6.5: a) Scattered field pattern of a split ring array antenna showing directionality in its scattering. The antenna is excited with a unit dipole positioned at 50 nm from the center in between the arms of the central split ring in the array. The field is calculated at a sphere 100 μm from the center of the antenna. The solid line shows $|E|^2$ in the plane zx and the dashed line shows $|E|^2$ in the plane zy. b) Depiction of the polarization state of the scattered field of the array antenna found on the forward (blue) and backward direction (red). c) Cartoon model that shows the positioning of the electric dipole on the split ring array antenna as well as the angled relative positioning of the split rings.

a plasmon antenna multipole resonance [29]. Also, such magnetic and magnetoelectric antennas may enhance the magnetic LDOS that magnetic transitions are sensitive to, as recently shown for rare earth ions near an interface [13]. Finally we used our understanding of split rings to design an array antenna that splits emission from a point source into two beams of oppositely handed elliptical polarization. For ultimately strong magnetic scatterers, these findings might provide new ways to manipulate spins via light, and enhance enantioselective spectroscopies in the near field [8, 30].

References

[1] V. M. Shalaev, *Optical negative-index metamaterials*, Nat. Photonics **1**, 41 (2007).

[2] I. Sersic, M. A. van de Haar, F. Bernal Arango, and A. F. Koenderink, *Ubiquity of optical activity in planar metamaterial scatterers*, Phys. Rev. Lett. **108**, 223903 (2012).

[3] N. Yu, P. Genevet, M. A. Kats, F. Aieta, J.-P. Tetienne, F. Capasso, and Z. Gaburro, *Light propagation with phase discontinuities: Generalized laws of reflection and refraction*, Science **334**, 333 (2011).

[4] F. Aieta, P. Genevet, N. Yu, M. A. Kats, Z. Gaburro, and F. Capasso, *Out-of-plane reflection and refraction of light by anisotropic optical antenna metasurfaces with phase discontinuities*, Nano Letters **12**, 1702 (2012).

[5] A. Ahmadi and H. Mosallaei, *Physical configuration and performance modeling of all-dielectric metamaterials*, Phys. Rev. B **77**, 045104 (2008).

[6] J. Pendry, A. Holden, D. Robbins, and W. Stewart, *Magnetism from conductors and enhanced nonlinear phenomena*, Microwave Theory and Techniques, IEEE Transactions on **47**, 2075 (1999).

[7] D. Schurig, J. J. Mock, B. J. Justice, S. A. Cummer, J. B. Pendry, A. F. Starr, and D. R. Smith, *Metamaterial electromagnetic cloak at microwave frequencies*, Science **314**, 977 (2006).

[8] Y. Tang and A. E. Cohen, *Optical chirality and its interaction with matter*, Phys. Rev. Let **104**, 163901 (2010).

[9] J. Li and J. B. Pendry, *Non-local effective medium of metamaterial*, eprint arXiv:cond-mat/0701332 (2007).

[10] I. Sersic, C. Tuambilangana, T. Kampfrath, and A. F. Koenderink, *Magnetoelectric point scattering theory for metamaterial scatterers*, Phys. Rev. B **83**, 245102 (2011).

[11] T. Kosako, Y. Kadoya, and H. F. Hofmann, *Directional control of light by a nano-optical yagi-uda antenna*, Nat. Photon. **4**, 312 (2010).

[12] A. F. Koenderink, *Plasmon nanoparticle array waveguides for single photon and single plasmon sources*, Nano Lett. **9**, 4228 (2009).

[13] S. Karaveli and R. Zia, *Spectral tuning by selective enhancement of electric and magnetic dipole emission*, Phys. Rev. Lett. **106**, 193004 (2011).

[14] I. M. Hancu, A. G. Curto, M. Castro-López, M. Kuttge, and N. F. van Hulst, *Multipolar interference for directed light emission*, Nano Letters **14**, 166 (2014).

[15] C. Enrich, M. Wegener, S. Linden, S. Burger, L. Zschiedrich, F. Schmidt, J. F. Zhou, T. Koschny, and M. Soukoulis, C. *Magnetic metamaterials at telecommunication and visible frequencies*, Phys. Rev. Lett. **95**, 203901 (2005).

[16] I. Sersic, M. Frimmer, E. Verhagen, and A. F. Koenderink, *Electric and magnetic dipole coupling in near-infrared split-ring metamaterial arrays*, Phys. Rev. Lett. **103**, 213902 (2009).

[17] M. Husnik, M. W. Klein, N. Feth, M. Konig, J. Niegemann, K. Busch, S. Linden, and M. Wegener, *Absolute extinction cross-section of individual magnetic split-ring resonators*, Nat. Photonics **2**, 614 (2008).

[18] A. Kwadrin and A. F. Koenderink, *Probing the electrodynamic local density of states with magneto-electric point scatterers*, Phys. Rev. B **86**, 125123 (2013).

[19] W. L. Barnes, A. Dereux, and T. W. Ebbesen, *Surface plasmon subwavelength optics*, Nature **424**, 824 (2003).

[20] A. V. Akimov, A. Mukherjee, C. L. Yu, D. E. Chang, A. S. Zibrov, P. R. Hemmer, H. Park, and M. D. Lukin, *Generation of single optical plasmons in metallic nanowires coupled to quantum dots*, Nature **450**, 402 (2007).

[21] T. H. Taminiau, F. D. Stefani, F. B. Segerink, and N. F. van Hulst, *Optical antennas direct single-molecule emission*, Nat. Photonics **2**, 234 (2008).

[22] A. G. Curto, G. Volpe, T. H. Taminiau, M. P. Kreuzer, R. Quidant, and N. F. van Hulst, *Unidirectional emission of a quantum dot coupled to a nanoantenna*, Science **329**, 930 (2010).

[23] C. T. Tai, *Dyadic Green's Functions in Electromagnetic Theory*, IEEE Press, New York, second edition, 1993.

[24] A. M. Kern and O. J. F. Martin, *Surface integral formulation for 3d simulations of plasmonic and high permittivity nanostructures*, J. Opt. Soc. Am. A **26**, 732 (2009).

[25] I. Hanninen, M. Taskinen, and J. Sarvas, *Singularity subtraction integral formulae for surface integral equations with rwg, rooftop and hybrid basis functions*, Progress In Electromagnetics Research **63**, 243 (2006).

[26] L. Novotny and B. Hecht, *Principles of Nano-optics*, Cambridge University Press, Cambridge, 2006.

[27] H. Mertens, A. F. Koenderink, and A. Polman, *Plasmon-enhanced luminescence near noble-metal nanospheres: Comparison of exact theory and an improved gersten and nitzan model*, Phys. Rev. B **76**, 115123 (2007).

[28] F. Bernal Arango, A. Kwadrin, and A. F. Koenderink, *Plasmonic antennas hybridized with dielectric waveguides*, ACS Nano **6**, 10156 (2012).

[29] A. G. Curto, M. Kuttge, G. Volpe, T. H. Taminiau, M. P. Kreuzer, R. Quidant, and N. F. van Hulst, *Magnetic and electric multipolar interactions with nanoantennas*, in *The 12th international conference on near-field optics, nanophotonics and related techniques*, 2012.

[30] M. Schäferling, D. Dregely, M. Hentschel, and H. Giessen, *Tailoring enhanced optical chirality: Design principles for chiral plasmonic nanostructures*, Phys. Rev. X **2**, 031010 (2012).

7

Adding Electric Quadrupolar Terms to the Retrieval of the Polarizability Tensor

In this chapter we extend the retrieval of the polarizability tensor that we explained in chapter 5 with the electric quadrupolar terms. We do this to underpin hybridization intuition for complex nanoantennas. In plasmonics and metamaterials it is a common practice to explain scattering features of complex structures in an intuitive manner as due to hybridization of electric dipoles. Recent developments in metamaterials as well as in plasmonic Fano systems have further included magnetic dipoles, and electric quadrupoles in this reasoning. We derive a method based on retrieval of the dipole and quadrupole polarizability tensors of nano scatterers from full-wave simulations that allows us to underpin this intuitive reasoning by quantifying the existent modes and their strengths in complex nano antennas. By application to a dolmen plasmon structure, we show how the retrieval sheds new light on plasmon induced transparency. Further by applying this method to aluminum nanopyramids we show how the interference between the multipole moments create asymmetrical LDOS enhancement that can be used for increasing LED's as well as solar cell efficiencies.

7.1 Introduction

The fields of plasmonic antennas, metasurfaces, and metamaterials, revolve around the idea that very strong scattering resonances in deeply subwavelength objects can be used to tailor the strength of optical near fields, scattering, and radiative processes [1–3]. Indeed great strides have been reported in using engineered clusters of nanoparticles to enhance solar cell absorption [4, 5], LED light emission [6, 7], single molecule

emission brightness and directivity [3, 8–13], optical sensing of very dilute analytes [14–16], and the development of metasurfaces [17, 18]. A workhorse interpretative tool to understand complex clusters of antennas is to reason in terms of coupled induced dipole moments that hybridize [19–21]. Surprisingly, once retardation and radiative corrections are taken into account accurate results can be obtained for especially far field observables such as extinction and scattering spectra, describing very well the essential physics of hallmark structures such as Yagi-Uda phased array antennas [10, 11, 22] as well as oligomers with plasmon induced transparency (PIT) features, such as the plasmon heptamer in which collective modes with large, resp. small net electric dipole moment form [23–28]. In fact, viewing a complex plasmon antenna as a collection of electric point dipoles has been employed not just as qualitative, but also as quantitative tool known as the "Discrete Dipole Approximation" (DDA) that is recognized to be valid as long as field gradients are small on the scale of the discretization [29]. More recently, efforts in metasurfaces as well as in plasmonically induced transparency have underlined that, rather than separating a structure into a set of discrete constituent electric dipoles, intuition may be advantageously developed by assigning to a given structure not just an electric dipole response, but also a magnetic dipole and electric quadrupole moment. While it is evident that both the DDA (taking many dipoles) and a full multipole expansion by definition can always capture the complete physics, the important notion here is that intuition benefits from reasoning with just few terms, and that for moderately sized antennas the response is usually assumed to derive from at most three leading multipoles. The first is the electric dipole response to incident electric field that is key to plasmonic hybridization. The second is a resonant response to curls of the electric field that embody magnetism in metamaterials and is implicitly assumed whenever a metamaterial object is viewed as an LC resonator. Thirdly, in recent works the resonant response of a structure to symmetric gradients of the electric field, *i.e.*, the electric quadrupole response has been invoked. Including just the electric dipole and magnetic dipole response allows to derive simple models for the response of metamaterials that quantitatively explain most reported optical experiments on split rings [30–32] and provide a minimal model to understand chirality and 'pseudo-chirality' in nano-optics, *i.e.*, the handed optical response of geometrically chiral, respectively non chiral structures [33, 34]. In a separate body of literature, workers focusing on plasmonically induced transparency have invoked the excitation of electric quadrupole modes as responsible for the occurrence of sharp features in extinction of antennas such as dolmens. Generally, one then fits the optical response to a coupled oscillator model, where one interprets the fitted coupling constants, damping rates and resonance frequencies to represent properties of the assumed quadrupole resonance (often coined 'dark mode') and electric dipole mode (often coined 'bright'). We argue that there is a large need for a simple but quantitative method to underpin whether the intuition that magnetic dipoles and electric quadrupoles are indeed at play is valid, and if so, what their properties are in terms of scattering strength, resonance frequency and width. One should realize that the common underpinning of intuition by examination of snapshots of field or charge distributions from full-wave simulations at distinct frequencies is problematic, since snapshots represent unseparated superpositions of

excited modes. For particular structures, several authors have sought to overcome this problem [28, 35]. Here we propose a method to retrieve and visualize electric and magnetic dipolar polarizabilities as well as quadrupolar polarizabilities, that generically allows us to underpin the intuition of which modes are involved in the scattering processes. As a useful byproduct this model can be used not just as an *a posteriori* interpretative tool. In a predictive manner, the output of our polarizability retrieval can be used as input for self-consistent multiple scattering calculations [20, 21, 31] for point particles that are assigned the retrieved responses. This predictive power then allows firstly design of new structures, and secondly to put the intuitive reasoning to the test and find out until what point it remains valid. To summarize the structure of this chapter, first we show that using a few essential symmetries, quadrupole moments can be treated with the same ease as dipole moments. In particular we retrieve the quadrupolar moments as well as electric and magnetic dipole moments from full-wave calculations, and show how these retrieved moments can be used to quantitatively underpin hitherto qualitative explanations of the physics of interesting systems. As a first example we revisit the "dolmen" structure [24, 26, 35–39], which was reported to show a Fano interference due to electric dipole-electric quadrupole coupling. We show that while these two modes are indeed at play, this description misses essential physics of the dolmen structure. Indeed, we find that the narrow resonance is due not just to a strong electric quadrupole, but in equal parts to a strong magnetic dipole character. This example thereby shows how our method greatly helps to objectify which modes to pinpoint as input for a coupled oscillator model. As a second example we apply the retrieval method to aluminum nano pyramid antennas, which show a strong asymmetrical directional emission of fluorescent dyes. In this example the super polarizability tensor retrieval gives us an insight of the origin of the very complex near field interferences that create this exotic effect.

7.2 Retrieval of quadrupoles and reduction of terms

The starting point of our work is chapter 9 in the book of Jackson [40] and recent work by Mühlig *et al* [41]. To recapitulate this starting point, we assume that a full-wave solution for the near field of the scatterer of interest in a homogeneous medium, and upon plane wave excitation is available. While any method may be used, we employ a surface integral equation method (SIE) [42] that we implemented previously (chapter 5). To derive induced multipole moments, we use the fact that the vector spherical harmonic functions $\mathbf{N}_{nm}(r,\theta,\phi)$ and $\mathbf{M}_{nm}(r,\theta,\phi)$ form a complete and orthonormal set [43]. Therefore the scattered near field $\mathbf{E}(r,\theta,\phi)$ has a unique expansion

$$\mathbf{E}(r,\theta,\phi) = \sum_{n=1}^{\infty} \sum_{m=-n}^{n} [a_{nm}\mathbf{N}_{nm}(r,\theta,\phi) + b_{nm}\mathbf{M}_{nm}(r,\theta,\phi)], \qquad (7.1)$$

where the expansion coefficients a_{nm} and b_{nm} can be simply found by projecting the calculated $\mathbf{E}(r,\theta,\phi)$ on the vector spherical harmonic functions. The expansion

coefficients are linearly related to the multipole moments in the following way:

$$p_x = \epsilon C_0 (a_{11} - a_{1-1})$$
$$p_y = \epsilon C_0 i (a_{11} + a_{1-1})$$
$$p_z = \epsilon C_0 (-\sqrt{2} a_{10})$$
$$m_x = -\sqrt{\frac{\epsilon}{\mu}} i c C_0 (b_{11} - b_{1-1})$$
$$m_y = \sqrt{\frac{\epsilon}{\mu}} c C_0 (b_{11} + b_{1-1})$$
$$m_z = -\sqrt{\frac{\epsilon}{\mu}} i c C_0 (-\sqrt{2} b_{10}) \qquad (7.2)$$
$$Q_{xy} = D_0 (a_{2-2} - a_{22})$$
$$Q_{xz} = D_0 i (a_{2-1} - a_{21})$$
$$Q_{yz} = D_0 (a_{2-1} + a_{21})$$
$$Q_{xx} = D_0 (i (a_{22} + a_{2-2}) - i \frac{\sqrt{6}}{3} a_{20})$$
$$Q_{yy} = D_0 (-i (a_{22} + a_{2-2}) - i \frac{\sqrt{6}}{3} a_{20})$$
$$Q_{zz} = D_0 (i \frac{2\sqrt{6}}{3} a_{20}).$$

Where $C_0 = 2\sqrt{6}\pi i / (c Z_0 k^3)$, $D_0 = -12\epsilon\sqrt{30}\pi / (Z_0 c k^4)$, $k = (\omega/c)\sqrt{\epsilon\mu}$, $Z_0 = \sqrt{\mu_0/\epsilon_0}$, ϵ_0 is the permittivity of free space μ_0 is the permeability of free space, c is the speed of light, ω is the frequency and finally ϵ and μ are the permittivity and permeability of the medium inside which the scatterer is positioned. As explained in chapter 5, one can very efficiently calculate the coefficients with excellent accuracy using numerical integration on just very few sampling points with points and weights chosen consistent with Legendre quadratures [44], owing to special properties for discrete Fourier transforms on the unit sphere.

Having summarized the established starting point, we turn to the key question, *i.e.*, how to reconstruct and analyze *polarizabilities*, given that it is possible to calculate multipole moments for any given illumination condition. The polarizability is the central quantity that summarizes the possible responses of a scattering unit to arbitrary incident fields, and can be used as input for predictive modeling of complicated arrangements of such units. For electric and magnetic dipoles deriving the polarizability from calculations of induced moments is completely resolved in chapter 5. Therefore, the key ingredient in this work is to revisit the quadrupole tensor. The quadrupole

moment is defined as a symmetric traceless tensor [40]

$$\overline{\mathbf{Q}} = \begin{pmatrix} Q_{xx} & Q_{xy} & Q_{xz} \\ Q_{xy} & Q_{yy} & Q_{yz} \\ Q_{xz} & Q_{yz} & Q_{zz} \end{pmatrix} \tag{7.3}$$

In a deeply subwavelength object, the quadrupole moments are generally set up by the symmetric part of the gradients of an incident electric field, through a fourth rank 'quadrupolarizability' [45] tensor [46, 47] α^Q_{ijmn}

$$Q_{ij} = \alpha^Q_{ijmn}(\partial_m E_n + \partial_n E_m)/2 \tag{7.4}$$

Here we use the Einstein summation notation, and abbreviate the spatial derivatives ∂/∂_{x_m} as ∂_m ($m = 1, 2, 3$ for x, y, z). If we use the fact that both the traceless tensor Q_{ij} and the tensor $(\partial_m E_n + \partial_n E_m)/2$ are symmetric, we can eliminate some redundancy in Eq. (7.4) and obtain a much simpler matrix equation $Q_i = \alpha^Q_{ij} \Diamond E_j$. Here the vectors

$$\mathbf{Q} = \{2Q_{xy}, 2Q_{xz}, 2Q_{yz}, Q_{xx}, Q_{yy}, Q_{zz}\} \text{ and} \tag{7.5}$$

$$\Diamond\mathbf{E} = \{(\partial_x E_y + \partial_y E_x)/2, (\partial_x E_z + \partial_z E_x)/2, (\partial_y E_z + \partial_z E_y)/2, \partial_x E_x, \partial_y E_y, \partial_z E_z\} \tag{7.6}$$

represent complete information on the quadrupolarizability tensor and the Diamond operator $\Diamond$ is introduced to ease the handling of the symmetric gradient operations.

We now combine this insight for quadrupoles, with the insight we reported in Ref. [31] and in chapter 5 for electric and magnetic dipole polarizability. We define the combination of dipole and quadrupole response as a 'superpolarizability' $\overline{\alpha}^{\mathbf{S}}$ tensor of the form:

$$\begin{pmatrix} \mathbf{p} \\ \mathbf{m} \\ \mathbf{Q} \end{pmatrix} = \overline{\alpha}^{\mathbf{S}} \begin{pmatrix} \mathbf{E} \\ \mathbf{H} \\ \Diamond\mathbf{E} \end{pmatrix} \tag{7.7}$$

An important practical merit of this definition over the use of the rank 4 quadrupolarizability is that the rank 2 superpolarizability tensor can be immediately plotted as a 2D color image, allowing direct comparison of dipolar and quadrupolar contributions. The superpolarizability furthermore leaves open the possibility that a scatterer or scattering cluster is strongly plasmonic (electric dipole polarizability is dominant), a metamaterial object (magnetic dipole polarizability is strong), bi-anisotropic (cross-polarizability in which magnetic (electric) driving begets an electric (magnetic) dipolar response, as in an LC-resonator), and quadrupolar. The quadrupole could be driven by the 6 components of $\Diamond\mathbf{E}$, as appropriate for a deeply subwavelength object, or by $\mathbf{E}$ or $\mathbf{H}$, through an equivalent of "bi-anisotropic cross coupling", as we will see below for the well-known dolmen plasmon antenna.

To find the 12×12 superpolarizability of an arbitrarily shaped object, it is necessary to supply sufficient linearly independent incident conditions, retrieve the induced moments, and then perform matrix inversion. A subtle point is that invertibility requires to remove one more degree of redundancy, which owes to the facts that

the quadrupole tensor is traceless $Q_{xx} + Q_{yy} + Q_{zz} = 0$, and that $\mathbf{E}$ is divergence free *i.e.* $\partial_x E_x + \partial_y E_y + \partial_z E_z = 0$. The redundancy can be removed by replacing $\mathbf{Q}$ by $\hat{\mathbf{Q}} = \{2Q_{xy}, 2Q_{xz}, 2Q_{yz}, Q_{xx}, Q_{yy}\}$ and $\lozenge\mathbf{E}$ by $\hat{\lozenge}\mathbf{E} = \{(\partial_x E_y + \partial_y E_x)/2, (\partial_x E_z + \partial_z E_x)/2, (\partial_y E_z + \partial_z E_y)/2, (\partial_x E_x - \partial_z E_z), (\partial_y E_y - \partial_z E_z)\}$. To cast the 12×12 tensor α^S in 11×11 form $\hat{\alpha}^S$ requires simply dropping the last column and row. In this work, procedurally, we first find the 11×11 $\hat{\alpha}^S$ tensor from the moments $(\mathbf{p}, \mathbf{m}, \hat{\mathbf{Q}})$ induced by 11 incidence conditions, and then expand to 12×12 form. To this end we define the 11×12 matrix M which has the 11×11 identity matrix as upper diagonal block, and which as last column has zeros except for its last two entries $M_{11,11} = M_{11,12} = -1$. With this definition, the expanded polarizability is retrieved as $\alpha^S = M^T \hat{\alpha}^S M$. Throughout this work we plot the full 12×12 superpolarizability, while for calculations that require matrix inversion we cast to and from the equivalent 11×11 form.

A sketch of the 11 required driving conditions is presented in Fig. 7.1. First, to construct three incidence conditions that only provide an electric field at the origin, without any magnetic field or electric-field gradient, we take counter-propagating co-polarized plane waves along the three Cartesian axes. Fig. 7.1a shows such a driving for the y axis. Next, to provide no electric field, but an H-field, at the origin, we shift the three standing waves by $\lambda/4$. Fig. 7.1b also shows such a driving for the y axes. It should be noted that this condition is not, in fact, free of electric field gradient at the origin. To form the 5 required electric field gradients without any admixing of E and H, we use 2 orthogonal pair sets of counter propagating plane waves with antiparallel polarization of the E field. Fig. 7.1c shows the combination of these 4 plane waves on the xy plane, which generates the required $\lozenge E_{xy}$ driving. We create 3 of the 5 required excitations with zero E and H field, but a strong field gradient, at the origin, by combinations along the Cartesian axes. In addition 2 excitations are created by using diagonals of the Cartesian cube. The superpolarizability simply follows from matrix inversion and is in fact entirely independent of the actual choice of linearly independent input fields. Finally we note two important facts. Firstly, it is important to realize that the simplification to a superpolarizability tensor does *not* involve an electrostatic approximation. Indeed, we use vector spherical harmonic projection of the full field solution to obtain the generalized Mie coefficients a_{nm} and b_{nm}, *i.e.*, the electrodynamic multipole coefficients that include all retardation effects. Secondly, while it is the sole purpose of this paper to derive an interpretative tool to underpin prior works that have invoked electric dipole, magnetic dipole and electric quadrupole responses only, the method can be extended also to include higher order moments. In particular, we note that while so far it has often been taken on face value that orders beyond the electric quadrupole are not relevant, the important question whether taking only the selected multipole terms indeed suffices at all is easily answered for any structure simply by calculating the higher order expansion coefficients of the scattered field using Eq. (7.1).
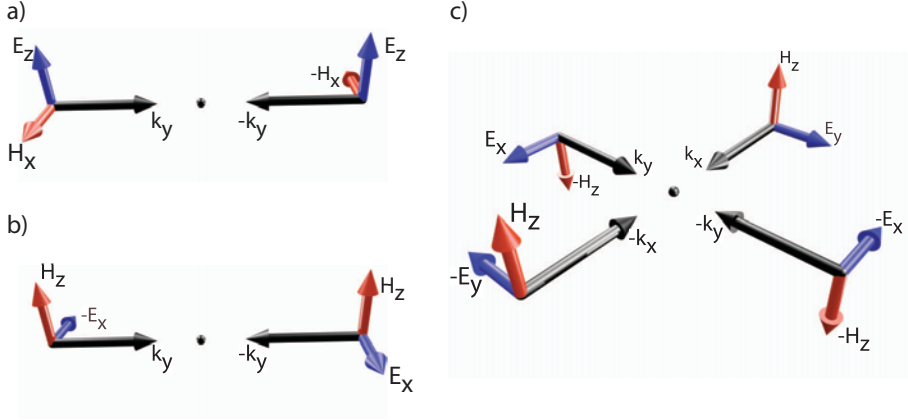
Figure 7.1: Sketches of the fields used for (a) a "pure" electric field driving with a combination of plane waves, (b) an antisymmetrical gradient (magnetic field) and a symmetric gradient field driving with a zero electric field, and finally in c) we show a "pure" symmetrical field gradient driving created with the combination of 4 counter-propagating plane waves.

Note on units

In order to be able to compare the magnitudes of driving field components, polarizabilities, respectively induced dipole moments in a useful way, we use a non-SI scaling of quantities based on the CGS unit system. Here we provide the unit conversion to SI, and the rationale behind the choice. In summary the rationale is that equal entries in the polarizability tensor correspond to equal scattered power. First, we scale the electric field, magnetic field, and electric field gradient to share as common unit [V/m], scaled such that a simple plane wave represents unit strength for all its nonzero components. The conversion reads

$$\mathbf{E} = \mathbf{E}_{SI}, \quad \mathbf{H} = Z_0 \mathbf{H}_{SI} \quad \text{and} \quad \Diamond \mathbf{E} = k \Diamond \mathbf{E}_{SI}. \tag{7.8}$$

Here Z_0 is the free space impedance. Next we scale all the induced moments from their SI definition so as to obtain as common unit [C m] (Coulomb meter), and such that any moment of unit strength radiates exactly the same power into the far field. The conversion reads

$$\mathbf{p} = \mathbf{p}_{SI}, \quad \mathbf{m} = 1/c\,\mathbf{m}_{SI} \quad \text{and} \quad \mathbf{Q} = \frac{k}{\sqrt{60}} \mathbf{Q}_{SI}. \tag{7.9}$$

The factor $k/\sqrt{60}$ results from the quadrupolar equivalent of Larmor's formula. For a dipole, Larmor's formula states that the radiated power is $P = c^2 Z_0 k^4/(12\pi)|\mathbf{p}_{SI}|^2$, while for a quadrupole $P = c^2 Z_0 k^6/(1440\pi)\sum_{\alpha,\beta}|Q_{SI,\alpha,\beta}|^2$. Finally, it should be noted that with this choice of units the superpolarizability tensor is automatically cast to have

units $\epsilon_0\mathrm{m}^3$ for all entries, where comparable entries necessarily contribute comparably to the scattered power. For completeness, here we tabulate the complete conversion. For the block diagonals the conversion reads:

$$\alpha_{\mathbf{p}}^{\mathbf{E}} = \alpha_{\mathrm{SI}}{}_{\mathbf{p}}^{\mathbf{E}}, \quad \alpha_{\mathbf{m}}^{\mathbf{H}} = \frac{1}{Z_0 c}\alpha_{\mathrm{SI}}{}_{\mathbf{m}}^{\mathbf{H}}, \quad \text{and} \quad \alpha_{\mathbf{Q}}^{\Diamond\mathbf{E}} = \frac{k^2}{\sqrt{60}}\alpha_{\mathrm{SI}}{}_{\mathbf{Q}}^{\Diamond\mathbf{E}}. \tag{7.10}$$

For the off-diagonal blocks, the conversion reads

$$\alpha_{\mathbf{m}}^{\mathbf{E}} = \frac{1}{c}\alpha_{\mathrm{SI}}{}_{\mathbf{m}}^{\mathbf{E}}, \quad \alpha_{\mathbf{p}}^{\mathbf{H}} = \frac{1}{Z_0}\alpha_{\mathrm{SI}}{}_{\mathbf{p}}^{\mathbf{H}}, \quad \alpha_{\mathbf{Q}}^{\mathbf{E}} = \frac{k}{\sqrt{60}}\alpha_{\mathrm{SI}}{}_{\mathbf{Q}}^{\mathbf{E}},$$

$$\alpha_{\mathbf{Q}}^{\mathbf{H}} = \frac{k}{Z_0\sqrt{60}}\alpha_{\mathrm{SI}}{}_{\mathbf{Q}}^{\mathbf{H}}, \quad \alpha_{\mathbf{p}}^{\Diamond\mathbf{E}} = k\alpha_{\mathrm{SI}}{}_{\mathbf{p}}^{\Diamond\mathbf{E}}, \quad \alpha_{\mathbf{m}}^{\Diamond\mathbf{E}} = \frac{k}{c}\alpha_{\mathrm{SI}}{}_{\mathbf{p}}^{\Diamond\mathbf{E}}. \tag{7.11}$$

Also, due to our definition of the vector $\mathbf{Q}$, the rows 7,8 and 9 in α^S are divided by 2. In Figures 7.3 and 8.2 we further take out the factor ϵ_0 so that the plotted quantity has units of volume and can be directly compared to particle volume.

## 7.3 Dolmen α^S-tensor

To demonstrate the utility of the multipole polarizability retrieval for the rigorous underpinning of hybridization intuition, we apply it to retrieve the α^S-tensor of a silver dolmen structure. This structure is composed of a single x-oriented rod, closely coupled to a y-oriented dimer of rods, and is well known because it exhibits PIT [24, 26, 35–39] when measuring extinction for x-polarized light incident along z. The structure
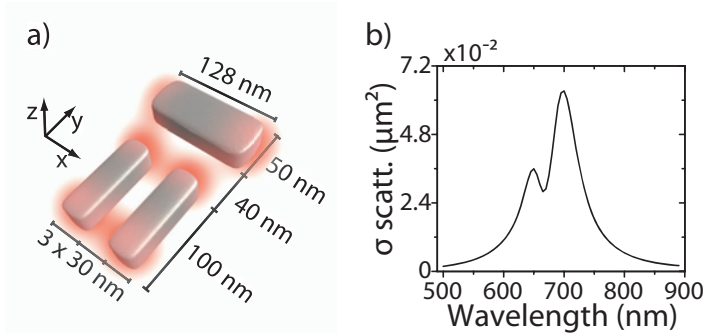
Figure 7.2: a) Sketch of the dolmen structure and the expected areas with high field enhancement. The sketch also presents the dimensions used. b) Total scattering cross section of the silver dolmen structure. The thickness is 20 nm.

used in our calculations is shown in Fig. 7.2a, with the corresponding dimensions. For the silver material we use the tabulated data in [48]. In Fig. 7.2b we show the

total scattering cross section of the structure as a function of optical wavelength. The resonant scattering cross section has two distinct features. The dominant feature is a maximum cross section at 687 nm, with a minimum close by at 665 nm. The spectral features are in good agreement with literature reports [36]. The proposed physics in those reports is that a Fano resonance occurs upon direct driving of the x-oriented dipolar resonance, which in turn through near field coupling drives a dark quadrupolar resonance of the dimer [36].
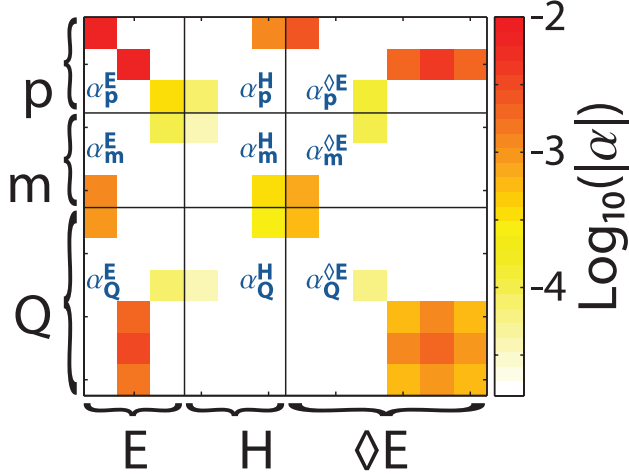
Figure 7.3: Plot of the superpolarizability tensor and the magnitude of its different components at a wavelength $\lambda = 665$ nm. The units of α^S are μm^3. (see note on units in sec. 7.2)

We retrieve the 12x12 superpolarizability of the entire dolmen and visualize its elements in Fig. 7.3. Figure 7.3 shows α^S at a wavelength of 665 nm as a color plot, where we present the logarithm of the magnitude of the elements of α^S. The logarithmic scale has the merit that it allows to quickly identify the entries that dominate the optical response as the red/orange color (see Methods in Sec. 7.2). Since the logarithmic scale unfortunately obscures small relative differences between elements (differences smaller than a factor 2) as well as phase information, we also report quantitative values for all non-negligible tensor elements in Appendix B of this thesis, and plot the amplitude and phase for select elements in Fig. 7.4.

To understand the structure of the reported tensor, the α^S tensor can be divided in 9 block matrices, four 3x3 matrices, two 3x6 matrices, two 6x3 matrices and one 6x6 matrix. Throughout its diagonal we find that the first block matrix ($\alpha_{\mathbf{p}}^{\mathbf{E}}$) is related to the purely electric dipolar response of the object, *i.e.* it quantifies the electric dipole created by an electric field. In particular, for the dolmen structure at 665 nm one finds a strong electric dipole polarizability $\alpha_{p_x}^{E_x} = 7.8 \times 10^{-3}$ μm^3 along x, attributable to the resonance of the top rod. The two y-oriented rods are responsible for a sizeable
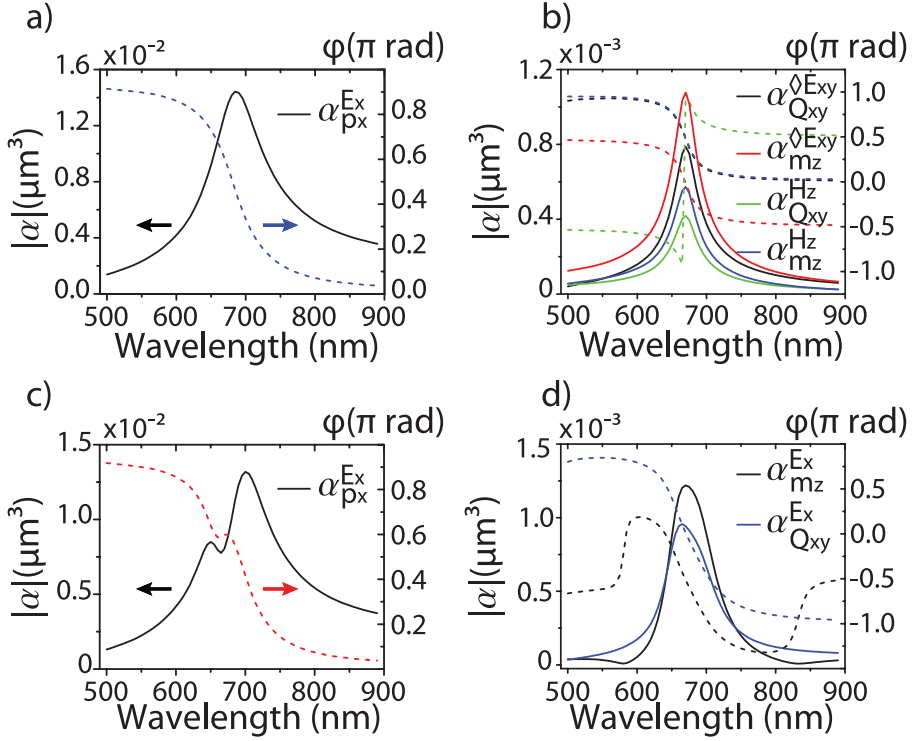
electric dipole polarizability $\alpha_{p_y}^{E_y} = 7 \times 10^{-3}$ μm^3 along y. While their resonance is shifted away from that of the x-oriented rod towards the blue to 625 nm, their large joint volume still ensures a significant polarizability comparable to that of the single x-rod. Finally, due to the small height of the rods the electric dipole polarizability along z is $\alpha_{p_z}^{E_z} = 3.4 \times 10^{-4}$ μm^3 or 1.3 orders of magnitude smaller.

The second diagonal block ($\alpha_{\mathbf{m}}^{\mathbf{H}}$) of the α^S tensor can be likewise interpreted as the purely magnetic dipolar response due to incident magnetic fields, while the third diagonal block is the quadrupolar response of the object due to symmetric gradients of the electric field ($\alpha_{\mathbf{Q}}^{\diamondsuit \mathbf{E}}$). The blocks outside the diagonal quantify cross coupling terms. In particular the 3x3 off-diagonal blocks quantify bi-anisotropy, *i.e.*, the generation of a magnetic dipole response upon driving by electric fields ($\alpha_{\mathbf{m}}^{\mathbf{E}}$) and vice versa. Finally, we also find quadrupoles induced directly by an electric or magnetic field($\alpha_{\mathbf{Q}}^{\mathbf{E}}, \alpha_{\mathbf{Q}}^{\mathbf{H}}$). In terms of polarizability contributions that stand out for the dolmen in terms of magnitude (apart from the electric dipole polarizability), we find that a strong z-oriented magnetic dipole, as well as a strong Q_{xy} can be induced by driving simply with the x−oriented E-field (first column of α^S, discussed at length below), while driving by y-oriented E-fields (second column) sets up a strong linear quadrupole moment along y (since $Q_{yy} = -2Q_{xx} = -2Q_{zz}$ [phase not shown in plot], with all other quadrupole moments negligible). We further note the approximate symmetry of α^S, which for purely dipolar magnetoelectric scatterers (top 6x6 block) is rigorous and a consequence of Onsager reciprocity [31, 49].

Evidently, the entire α^S tensor contains very rich physics that allows pinpointing for each excitation condition exactly which moments are induced. Such insights may then be further cast into a microscopic analysis by examination how particular incident field distributions set up, for instance, particular charge oscillations inside the cluster. To illustrate how such an analysis can enrich insights in important optical phenomena, we specifically focus on the dolmen response to an x-polarized plane wave, i,e, the first column only of α^S. The retrieved polarizability shows that the dominant responses driven by an x-polarized plane wave as used in all reported experiments, involve p_x, and the expected 'dark' quadrupole Q_{xy}. More unexpectedly an out-of-plane magnetic response m_z also is significant. These three response contributions are cross coupled, in the sense that driving any of the three 'directly' (via the diagonal of α^S), also excites the others. For instance, in the original description of PIT experiments, it is understood that one drives p_x directly by E_x, which then induces the expected in-plane quadrupole response Q_{xy} (as well as the associated magnetic response m_z). Conversely, the quadrupole can also be directly driven via application of the symmetric E-field gradient $\diamondsuit E_{xy}$, in which case also an electric dipole moment p_x is induced. Thus, the polarizability tensor directly evidences the suspected hybridization of an x-oriented electric dipole with the Q_{xy} quadrupole moment. Furthermore our results point at an accompanying magnetic response that was not invoked in previously reported discussions on PIT in dolmens.

As regards microscopic analysis of their origin, out of these three contributions the p_x and Q_{xy} were already assigned in literature to the fundamental dipole mode of the top rod, respectively the antisymmetrically oscillating dimer. This assignment

Figure 7.4: a) Magnitude and phase of the polarizability of the isolated dolmen's top particle for electric dipoles created by electric fields in the x direction, b) magnitude and phase of the polarizability of the dolmen's arms for magnetic dipoles in z created by magnetic fields in the z direction, quadrupoles in the xy plane created by $\Diamond E_{xy}$ gradients as well as magnetic dipoles created by $\Diamond E_{xy}$ and quadrupoles in the xy plane created by magnetic fields in the z direction. Finally c) and d) show the magnitude and phase of the polarizability vs. wavelength of the electric dipole in the x axis, the magnetic dipole in z as well as the quadrupole in the xy plane for an electric field oriented in the x axis.

can be further underpinned by examining separately the superpolarizabilities of the isolated particles that compose the dolmen, i.e the *x*-oriented rod on one hand, and the dimer on the other hand. As shown in Fig. 7.4a the isolated top particle has a strong electric dipole polarizability $\alpha_{p_x}^{E_x} = 14.4 \times 10^{-3}$ μm^3 that is resonant at 687 nm with a width of 89 nm. The top particle alone is responsible for essentially the complete *x*-oriented electric polarizability of the entire dolmen. The isolated dimer in contrast (Fig. 7.4b) shows a resonance that carries both the expected quadrupolar $\alpha_{Q_{xy}}^{\Diamond E_{xy}}$ that PIT literature has focused on, and the magnetic dipole $\alpha_{m_z}^{H_z}$ that was hitherto disregarded in PIT literature but emphasized in literature on metamaterial applications for cut

wire pairs [50]. These moments are associated with the same asymmetric current distribution mode of the bare dimer, centered at 665 nm with a width of 50 nm. Clearly, the magnetic dipole and electric quadrupole belong to the same resonance, and share cross polarizabilities. This feature is generally found for antennas constructed by two separated electric dipoles such as in cut-wire pairs [50, 51]. Meyrath *et al.* [52] in a critical appraisal of the law of electromagnetic induction have argued that in absence of closed conduction loops and given the non-electrostatic nature of the system, a strict separation cannot be made between magnetic and electric responses. We note that the induced moments can through Eq. (7.1), be separated clearly either mathematically on basis of projection on vector spherical harmonics, or in an experimental observable such as the far field angular radiation pattern that differs markedly for magnetic dipoles and electric quadrupoles [53]. The ambiguity that Meyrath *et al.* [52] point out, however is evident in the fact that the asymmetric resonance cannot be uniquely assigned either to a response to magnetic field H_z or to a response to nonuniformities in electric field. Indeed, the asymmetric mode of the cut-wire pair is simply driven by $\partial_x E_y$, which is contained equally in the curl of E (*i.e.*, in $H_z = \partial_x E_y - \partial_y E_x$) and in the symmetric gradient (*i.e.* in $\lozenge E_{xy} = \frac{1}{2}[\partial_x E_y + \partial_y E_x]$).

Returning to the superpolarizability for the entire dimer, we consider the frequency dependence of select components in Fig. 7.4c to trace the emergence of PIT. For $\alpha_{p_x}^{E_x}$, the dipolar polarizability of the rod gains a dispersive Fano resonance at 665 nm, demonstrating that hybridization occurs. As complementary information, Fig. 7.4d demonstrates that the resonances of the strong cross polarizabilities $\alpha_{m_z}^{E_x}$ and $\alpha_{Q_{xy}}^{E_x}$ likewise are a product of the hybridization of the composing elements, where the quadrupole contribution broadens as a consequence of coupling to the bright dipolar resonance of the rod. Thus the simple superpolarizability retrieval presented here provides important underpinning for the physical picture proposed in literature. Rather than resorting to quasi-electrostatics, or visually inspecting snapshots of simulated charge distributions, the superpolarizability tensor quantitatively reports which multi-pole moments are involved.

As a further insight that is provided by the superpolarizability analysis, we find that it allows to quantify the common assumption that the dimer resonance with its combined electric quadrupole and magnetic dipole moment is a *dark* resonance. As we see in the plotted amplitudes of α^S, the magnetic and quadrupolar moments induced through the incident electric field scatter comparable amounts, and the total power radiated by the asymmetric mode is within a factor 3 from that radiated by the induced electric dipole. To summarize, while the term 'dark' adequately describes the lack of direct coupling between an incident x-polarized plane wave incident along z and the asymmetric mode, the radiation pattern of a dolmen actually contains significant contribution from the asymmetric mode, in apparent contradiction to the terminology 'dark' resonance.

A third observation is that the Fano lineshape is ultimately determined not only by the amplitude but also by the phase of the cross-polarizability, as motivated from a coupled oscillator model by Zhang *et al.* [36]. In principle the superpolarizability tensor provides a direct method to read off, and microscopically understand, the phase. Finally

we note that as in any optical Fano system, a challenge is to ultimately identify the true normal, *i.e.*, *uncoupled* eigenmodes, as was recently reported for the Fano resonance in plasmonic heptamers [28], and investigated by Gallinet *et al.* [35]. We propose that such an analysis can be realized by examining poles of the superpolarizability as one sweeps frequency into the complex frequency plane [20, 54, 55].

7.4 Nanopyramids α^S-tensor

As a second application of the super polarizability tensor retrieval we use the method on aluminum nanopyramid antennas, like the ones shown in Fig. 7.5. This study is motivated by recent extinction and photoluminescence experiments performed at Phillips Research by S.R.K. Rodriguez et al. [56] on such truncated pyramids. The nanopyramids are fabricated using soft imprint lithography at Philips, for an envisioned application in LED remote phosphor technology. White light LEDs are most efficiently made by using a blue pump LED in combination with a phosphorescent or fluorescent material that efficiently converts blue light into longer wavelength visible photons. Therefore, intense research efforts are directed to incorporating plasmonic structures in ultrathin fluorescent layers to enhance absorption of blue light, and to accelerate or redirect emission of visible light. Beyond the use of small metal nanoparticles that simply provide an electric dipole moment, emission might be advantageously redirected into preferred directions by using scatterers with high order moments. In particular, we were inspired by the Kerker paradox for scattering which states that for scatterers with a special ϵ and μ the scattering appears to have zero forward scattering, yet nonzero extinction. This apparent paradox that occurs for very small spheres when $\epsilon = (4 - \mu)/(2\mu + 1)$ gained new interest in the framework of cloaking and invisibility [57, 58]. Alú et. al. [59] showed that these spheres indeed have very low, yet nonzero forward scattering, thereby complying with the optical theorem. The almost zero forward scattering results from destructive interference in the forward direction of the radiation of the generated electric dipole and magnetic dipole moment. On this basis one might ask if particles like nanopyramids could attain asymmetric emission of the phosphorescent or fluorescent light stemming from the interference of the different multipolar components of the nanopyramid antennas, which would increase the total efficiency in LED lighting. We will present an analysis consisting of the following ingredients: superpolarizability retrieval and geometric optimization of nanopyramid shaped antennas to reach a generalized Kerker condition, calculations to verify this scenario provides asymmetric emission, and finally a summary of experimental results.

Pyramids α^s retrieval and geometrical optimization

To start we find α^s (Fig. 7.6a) for a typical fabricated aluminum nanopyramid, with a geometry presented in Fig. 7.6b where t =84 nm, h =150 nm and b =144 nm. Fig. 7.6a shows α^s (in units of μm^3), where we see that the ANPs possess a strong
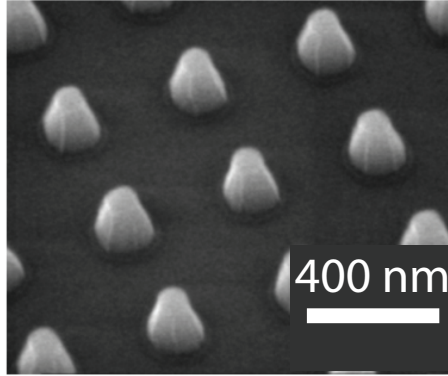
Figure 7.5: Scanning electron micrograph of an aluminum nanopyramid array. Courtesy of S.R.K. Rodriguez and Mark Verschuuren

magneto-electric cross-coupling polarizability $\alpha_{\mathbf{m}}^{\mathbf{E}}$ and $\alpha_{\mathbf{p}}^{\mathbf{H}}$. Comparing this to the electric polarizability, we find $|\alpha_{\mathbf{p}}^{\mathbf{E}}|/|\alpha_{\mathbf{m}}^{\mathbf{E}}|=13$. This resembles split ring resonators at infrared frequencies as we show in chapter 6.2, but now realized at visible frequencies, thanks to the high plasma frequency of the aluminum. Fig. 7.6a further shows that x or y polarized plane waves, without a strong gradient, directly induce quadrupoles in the xz and yz planes. The magnetic dipoles along x and y and the quadrupoles in the yz and xz planes, respectively, are intimately related through the rotational symmetry of the structure. This superpolarizability shows us that the nanopyramid antennas possess strong multipolar modes. The next question that comes to mind is if the modification of parameters in this antenna, e.g. material or shape could alter the strength of the multipoles independently so that we can create antennas with controlled combinations of electric, magnetic and quadrupolar moments.

By looking at the different components of α^s as a function of the nanopyramid geometry we analyze their dependence on the height and tapering of the pyramids. The geometries used for this analysis are presented in Fig. 7.7. The calculated volumes for the first row of pyramids, where the size of the top face is varied, from left to right are: $1.47x10^{-3}$ μm^3, $1.7x10^{-3}$ μm^3, $1.97x10^{-3}$ μm^3, $2.29x10^{-3}$ μm^3, $2.64x10^{-3}$ μm^3, $3.03x10^{-3}$ μm^3. The calculated volumes for the second row of pyramids, where the height of the pyramid is varied, from left to right are: $0.793x10^{-3}$ μm^3, $1.19x10^{-3}$ μm^3, $1.58x10^{-3}$ μm^3, $1.97x10^{-3}$ μm^3, $2.37x10^{-3}$ μm^3. The light grey pyramid presented in Fig. 7.7 is the model of the pyramid used for the experiments that will be shown below. The reported top size of the fabricated pyramid is 70 nm which is the same size as the one of the light grey model without the chamfer used to avoid unreal sharp edges.

To compare in a fair way structures with different geometries, we divide α^s by the volume of the corresponding structure. We consider x-polarized illumination, for which the most significant elements of α^s are indicated by the legend in Fig. 7.8. In this figure α^s is evaluated at the electric dipolar resonance wavelength for each structure, i.e.
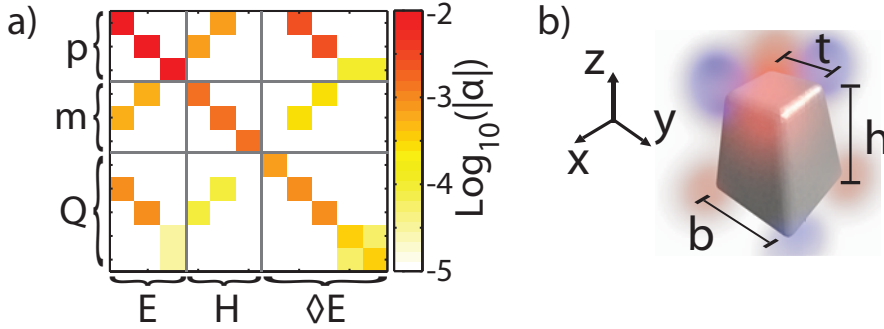
Figure 7.6: a) Superpolarizability tensor α^s of an aluminum pyramid with t = 84 nm, h = 150 nm and b = 144 nm, at the electric dipolar resonance wavelength. b) Schematic of the structure.
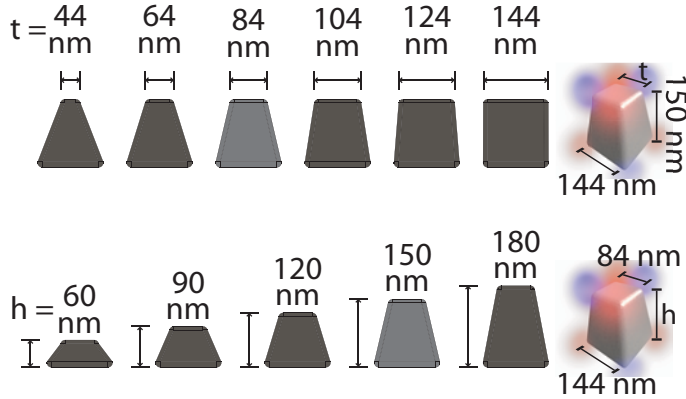
Figure 7.7: Geometries of the pyramids used for the simulations. The top line shows the array of pyramids with variations in their top size. The bottom line shows the array of pyramids with variations to their height.

600 nm, 620 nm, 660 nm 680 nm, 720 nm and 740 nm for the pyramids with top size shown in Fig. 7.7, first row, in order from left to right. We begin by fixing b = 144 nm and h = 150 nm, at the same time we vary t as shown in the top part of Fig. 7.8a. Fig. 7.8a shows that the magnetoelectric (α_{my}^{Ex}) and quadrupolar (α_{Qxz}^{Ex}) response are weak without tapering, but increase monotonically by 3 orders of magnitude for increased tapering. We continue our parametric investigation of the influence of the geometry on α^s by fixing t=84 nm, b=144 nm, while varying h, as shown in Fig. 7.8b. The magnetic (α_{my}^{Hy}), magnetoelectric (α_{my}^{Ex}), and quadrupolar ($\alpha_{Qxz}^{\Diamond Exz}$) response increase monotonically while the electric dipole (α_{px}^{Ex}) response decreases. Figure 7.8 indicates a possible route to follow regarding the design of pyramidal antennas. As shown by the

117

figure magnetoelectric and quadrupolar moments increase monotonically with tapering and height. This enables us to approach the generalized near-field Kerker condition as described in Ref. [60], without needing to use magnetic materials with exotic optical $\mu \neq 1$. In turn, radiation patterns with a pronounced forward to backward asymmetry are expected. Note that the magnetoelectric enhancement saturates for increased h. Therefore, unnecessarily high structures must be avoided to minimize Ohmic losses without degrading the magnetoelectric response.
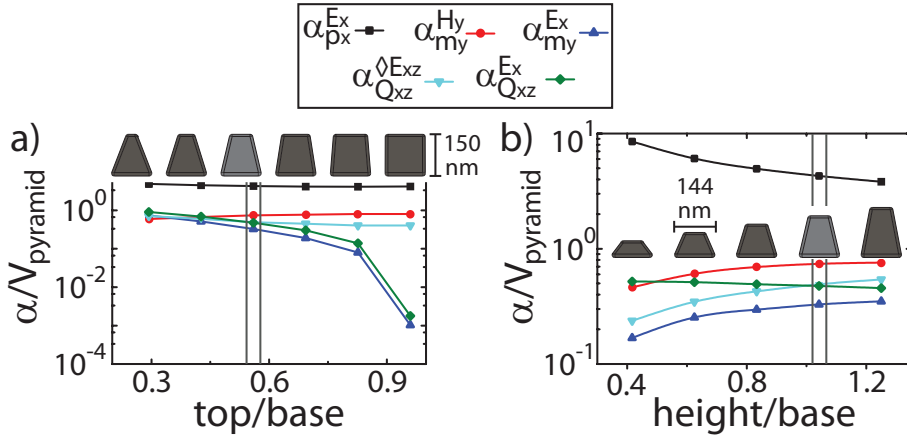

Figure 7.8: a) and b) display the most significant elements of α^s as function of the tapering and height of the pyramids, respectively.

Calculations of emission directivity

We resort to our home-written SIE program to calculate the radiation patterns of nanopyramids excited with a localized source. The radiation patterns allow us to prove that a reasonable choice of height and tapering provides nanopyramidal structures with a pronounced forward to backward asymmetry in radiation. First we show in Fig. 7.9a the scattering far field pattern of our pyramidal antenna (light grey antenna in Fig. 7.7), the radiation is calculated 100 μm from the center of the antenna i.e. ~166 wavelengths away. This scattering is created when the antenna is driven by a single dipolar emitter positioned in the vicinity of the pyramid 25 nm from the pyramid (red curve) and -25 nm from the pyramid (black curve), at a wavelength of 660 nm. In the left panel of Fig. 7.9a we present the total emitted plus scattered power created by a planarly oriented dipolar source while on the right panel we present the results for a vertically aligned dipolar source (As shown in the insets). The unbalanced emission in both cases indicates that selectively positioning emitters provides directional emission.

Fig. 7.9b shows the modified radiative local density of states where we only integrate the radiated power in the top half sphere ρ_{top} and the bottom half sphere
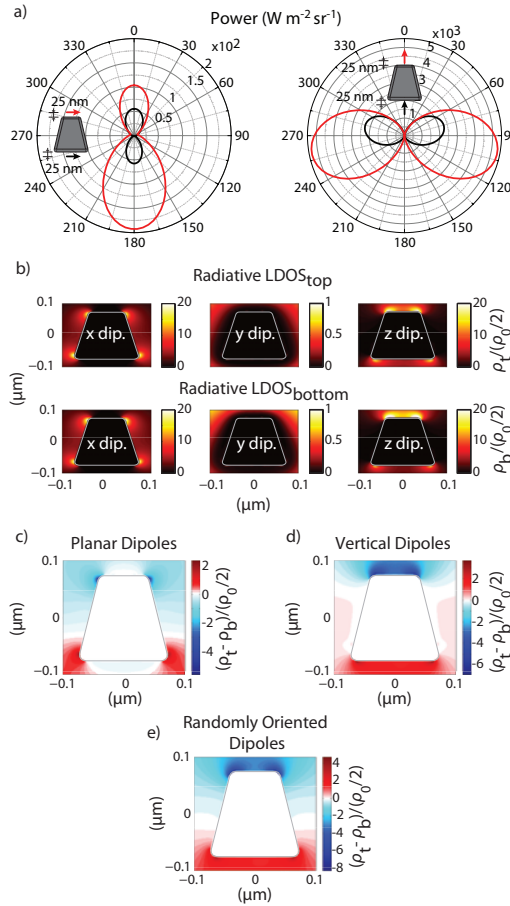
Figure 7.9: a) Radiation pattern for an electric dipole positioned above (red line) or below (black line) the pyramid, and oriented parallel (left panel) or perpendicular (right panel) to the top and bottom facets of the pyramid. The dipoles are located 25 nm from the top and bottom facets of the pyramid, as shown in the insets. b) Top and bottom directed radiative local density of optical states (LDOS), ρ_t and ρ_b respectively, for x, y and z oriented dipoles near the pyramid, normalized to the free-space LDOS ρ_0. c) d) and e) top-bottom difference in LDOS enhancement, $(\rho_t - \rho_b)/\rho_0$, with respect to the free-space LDOS ρ_0. This graph shows that a horizontal dipole radiates more efficiently towards the bottom if positioned on top of the pyramid or towards top if positioned under the pyramid.

ρ_{bottom} for the three different Cartesian orientations of dipoles positioned around the pyramid. Here ρ_0 is the free space radiative LDOS.

In Fig. 7.9c, d and e we plot the top-bottom difference in LDOS, $(\rho_t - \rho_b)/\rho_0$, with respect to the free-space LDOS ρ_0, In this figure we observe that for both in-plane

and out-of-plane dipoles radiation is enhanced towards the bottom when the dipole is positioned on the top region of the pyramid. Conversely the radiation is enhanced towards the top when the dipole is position on the bottom region of the pyramid. Fig. 7.9e shows that the effect is the same when all dipole orientations are considered.

Measurements

In order to test the theory, we compare it to measurements of photoluminescence enhancement of an array of pyramids embedded in a polymer matrix (polystyrene) doped with 1% fluorescent dye (Lumogen F305). The pyramids have the dimensions described for the light grey structure in Fig. 7.7. The polymer is spin cast on top of an array with a pitch of 400 nm. Since the pyramids are fabricated on top of a glass substrate the coating procedure ensures that we are positioning the dye molecules only on the top region of the pyramid. Fig. 7.10a shows an extinction measurement performed by S.R.K. Rodriguez on the array where the broad peak at 660 nm indicates the position of the localized plasmon resonance of the individual pyramids and the narrow blue shifted peak at 580 nm is associated to the delocalized surface lattice resonance. This resonance is created by the array where a grating condition is met. At this frequency the scattering from all the antennas in the array interferes constructively in the plane of the array creating a delocalized mode which is extended throughout the array of particles. Fig. 7.10b shows the photoluminescence enhancement measurements performed by acquiring the dye fluorescence directed towards the bottom of the pyramids (red line) and towards the top of the pyramids (black line). At the wavelengths of the pyramidal localized plasmon resonance we clearly see that the light is preferentially sent towards the bottom of the pyramid since the PLE in the red curve is about 4/3 times higher than the black curve. This complies well with the theory exposed above. Surprisingly the PLE is higher towards the top of the pyramids for the wavelengths centered around the surface lattice plasmon resonance. This last effect could be modeled by introducing the α^s in a multiple scattering point dipole-quadrupole theory which so far we have not developed but which based on the knowledge of this chapter could be straightforwardly implemented. In full wave calculations performed with COMSOL, which take into account the arrays and the presence of the substrate, indeed the reversed asymmetry for the surface lattice plasmon resonance is also found.

7.5   Conclusions

To summarize, we have presented a straightforward method to retrieve dipolar but also quadrupolar polarizabilities α^Q for arbitrary scatterers in order to provide substantiation for hybridization intuition, and even input for quantitative hybridization reasoning for plasmonic antenna structures. A key simplification is to handle quadrupolar terms through the $\diamond$ operator to avoid redundancy and ease visualization. As a first example we have analyzed the plasmonic dolmen structure, providing a quantitative underpinning for reported hybridization intuition in terms of electric dipole-to-quadrupole
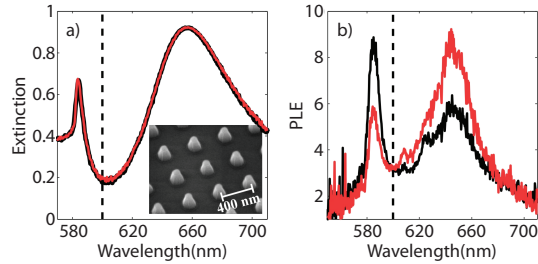
Figure 7.10: a) Measured extinction, and (b) photoluminescence enhancement (PLE) towards the top (black line) and bottom (red line) of the pyramids. The inset in (a) displays a SEM of the fabricated structures before the dye doped layer was spin coated. The dashed line in b) indicates the Rayleigh anomaly.

coupling. In addition to quantifying the strength of the induced moments, the retrieval also evidenced a commonly disregarded but equally important magnetic dipole moment. As a second example we have used the method for analyzing aluminum nanopyramid antennas. The analysis gave us the understanding of what are the most important multipoles involved in the scattering processes and how these multipoles interfere and produce an interesting near field asymmetrical effect, which can be used for enhancement of LED illumination or solar cells light capturing. In our view, these examples clearly show the very large potential of superpolarizability retrieval for the quantitative understanding of many complex plasmon and dielectric antenna phenomena.

References

[1] L. Novotny and N. van Hulst, *Antennas for light*, Nat. Photon. **5**, 83 (2011).

[2] J. A. Schuller, E. S. Barnard, W. Cai, Y. C. Jun, J. S. White, and M. L. Brongersma, *Plasmonics for extreme light concentration and manipulation*, Nat. Mater. **9**, 193 (2010).

[3] M. Agio and A. Alú, editors, *Optical Antennas*, Cambridge University Press, 2013.

[4] S. Pillai, K. R. Catchpole, T. Trupke, and M. A. Green, *Surface plasmon enhanced silicon solar cells*, Journal of Applied Physics **101**, 093105 (2007).

[5] H. A. Atwater and A. Polman, *Plasmonics for improved photovoltaic devices*, Nat Mater **9**, 205 (2010).

[6] G. Lozano, D. J. Louwers, S. R. Rodriguez, S. Murai, O. T. Jansen, M. A. Verschuuren, and J. Gomez Rivas, *Plasmonics for solid-state lighting: enhanced excitation and directional emission of highly efficient light sources*, Light Sci Appl **2**, e66 (2013).

[7] V. Giannini, A. I. Fernáandez-Domínguez, S. C. Heck, and S. A. Maier, *Plasmonic nanoantennas: Fundamentals and their use in controlling the radiative properties of nanoemitters*, Chem. Rev. **111**, 3888 (2011).

[8] P. Anger, P. Bharadwaj, and L. Novotny, *Enhancement and quenching of single-molecule fluorescence*, Phys. Rev. Lett. **96**, 113002 (2006).

[9] S. Kühn, U. Håkanson, L. Rogobete, and V. Sandoghdar, *Enhancement of single-molecule fluorescence using a gold nanoparticle as an optical nanoantenna*, Phys. Rev. Lett. **97**, 017402 (2006).

[10] A. F. Koenderink, *Plasmon nanoparticle array waveguides for single photon and single plasmon sources*, Nano Lett. **9**, 4228 (2009).

[11] A. G. Curto, G. Volpe, T. H. Taminiau, M. P. Kreuzer, R. Quidant, and N. F. van Hulst, *Unidirectional emission of a quantum dot coupled to a nanoantenna*, Science **329**, 930 (2010).

[12] A. Kinkhabwala, Z. Yu, S. Fan, Y. Avlasevich, K. Mullen, and M. E., *Large single-molecule fluorescence enhancements produced by a bowtie nanoantenna*, Nat Photon **3**, 654 (2009).

[13] D. Punj, M. Mivelle, S. B. Moparthi, T. S. van Zanten, H. Rigneault, N. F. van Hulst, M. F. Garcia-Parajo, and J. Wenger, *A plasmonic /'antenna-in-box/' platform for enhanced single-molecule analysis at micromolar concentrations*, Nat Nano **8**, 512 (2013).

[14] J. N. Anker, W. P. Hall, O. Lyandres, N. C. Shah, J. Zhao, and R. P. Van Duyne, *Biosensing with plasmonic nanosensors*, Nat Mater **7**, 442 (2008).

[15] C. Escobedo, A. G. Brolo, R. Gordon, and D. Sinton, *Optofluidic concentration: Plasmonic nanostructure as concentrator and sensor*, Nano Letters **12**, 1592 (2012).

[16] J. Ferreira, M. J. L. Santos, M. M. Rahman, A. G. Brolo, R. Gordon, D. Sinton, and E. M. Girotto, *Attomolar protein detection using in-hole surface plasmon resonance*, J. Am. Chem. Soc. **131**, 436 (2009).

[17] N. Yu, P. Genevet, M. A. Kats, F. Aieta, J.-P. Tetienne, F. Capasso, and Z. Gaburro, *Light propagation with phase discontinuities: Generalized laws of reflection and refraction*, Science **334**, 333 (2011).

[18] X. Ni, N. K. Emani, A. V. Kildishev, A. Boltasseva, and V. M. Shalaev, *Broadband light bending with plasmonic nanoantennas*, Science **335**, 427 (2012).

[19] E. Prodan, C. Radloff, N. J. Halas, and P. Nordlander, *A hybridization model for the plasmon response of complex nanostructures*, Science **302**, 419 (2003).

[20] W. H. Weber and G. W. Ford, *Propagation of optical excitations by dipolar interactions in metal nanoparticle chains*, Phys. Rev. B **70**, 125429 (2004).

[21] F. J. García de Abajo, *Colloquium: Light scattering by particle and hole arrays*, Rev. Mod. Phys. **79**, 1267 (2007).

[22] F. Bernal Arango, A. Kwadrin, and A. F. Koenderink, *Plasmonic antennas hybridized with dielectric waveguides*, ACS Nano **6**, 10156 (2012).

[23] B. Luk'yanchuk, N. I. Zheludev, S. A. Maier, N. J. Halas, P. Nordlander, H. Giessen, and C. T. Chong, *The fano resonance in plasmonic nanostructures and metamaterials*, Nat Mater **9**, 707 (2010).

[24] N. Liu, L. Langguth, T. Weiss, J. Kastel, M. Fleischhauer, T. Pfau, and H. Giessen, *Plasmonic analogue of electromagnetically induced transparency at the drude damping limit*, Nat Mater **8**, 758 (2009).

[25] F. Hao, Y. Sonnefraud, P. V. Dorpe, S. A. Maier, N. J. Halas, and P. Nordlander, *Symmetry breaking in plasmonic nanocavities: Subradiant lspr sensing and a tunable fano resonance*, Nano Letters **8**, 3983 (2008), PMID: 18831572.

[26] N. Verellen, Y. Sonnefraud, H. Sobhani, F. Hao, V. V. Moshchalkov, P. V. Dorpe, P. Nordlander, and S. A. Maier, *Fano resonances in individual coherent plasmonic nanocavities*, Nano Letters **9**, 1663 (2009).

[27] N. A. Mirin, K. Bao, and P. Nordlander, *Fano resonances in plasmonic nanoparticle aggregates*, J. Phys. Chem. A **113**, 4028 (2009).

[28] M. Frimmer, T. Coenen, and A. F. Koenderink, *Signature of a fano resonance in a plasmonic metamolecule's local density of optical states*, Phys. Rev. Lett. **108**, 077404 (2012).

[29] S. Y. Park and D. Stroud, *Surface-plasmon dispersion relations in chains of metallic nanoparticles: An exact quasistatic calculation*, Phys. Rev. B **69**, 125418 (2004).

[30] A. Belov, S. I. Maslovski, K. R. Simovski, and S. A. Tretyakov, *A condition imposed on the electromagnetic polarizability of a bianisotropic lossless scatterer*, Tech. Phys. Lett. **29**, 718 (2003).

[31] I. Sersic, C. Tuambilangana, T. Kampfrath, and A. F. Koenderink, *Magnetoelectric point scattering theory for metamaterial scatterers*, Phys. Rev. B **83**, 245102 (2011).

[32] F. Bernal Arango and A. F. Koenderink, *Polarizability tensor retrieval for magnetic and plasmonic antenna design*, New. J. Phys. **15**, 073023 (2013).

[33] E. Plum, X. . X. Liu, V. A. Fedotov, Y. Chen, D. P. Tsai, and N. I. Zheludev, *Metamaterials: Optical activity without chirality*, Phys. Rev. Lett. **102**, 113902 (2009).

[34] I. Sersic, M. A. van de Haar, F. Bernal Arango, and A. F. Koenderink, *Ubiquity of optical activity in planar metamaterial scatterers*, Phys. Rev. Lett. **108**, 223903 (2012).

[35] B. Gallinet and O. J. F. Martin, *Relation between near–field and far–field properties of plasmonic fano resonances*, Opt. Express **19**, 22167 (2011).

[36] S. Zhang, D. A. Genov, Y. Wang, M. Liu, and X. Zhang, *Plasmon-induced transparency in*

metamaterials, Phys. Rev. Lett. **101**, 047401 (2008).

[37] N. Liu, T. Weiss, M. Mesch, L. Langguth, U. Eigenthaler, M. Hirscher, C. Sonnichsen, and H. Giessen, *Planar metamaterial analogue of electromagnetically induced transparency for plasmonic sensing*, Nano Lett. **10**, 1103 (2010).

[38] N. Liu, M. Hentschel, T. Weiss, A. P. Alivisatos, and H. Giessen, *Three-dimensional plasmon rulers*, Science **332**, 1407 (2011).

[39] Z. Ye, S. Zhang, Y. Wang, Y.-S. Park, T. Zentgraf, G. Bartal, X. Yin, and X. Zhang, *Mapping the near-field dynamics in plasmon-induced transparency*, Phys. Rev. B **86**, 155148 (2012).

[40] J. D. Jackson, *Classical Electrodynamics*, Wiley, New York, third edition, 1999.

[41] S. Mühlig, C. Menzel, C. Rockstuhl, and F. Lederer, *Multipole analysis of meta-atoms*, Metamaterials **5**, 64 (2011).

[42] A. M. Kern and O. J. F. Martin, *Surface integral formulation for 3d simulations of plasmonic and high permittivity nanostructures*, J. Opt. Soc. Am. A **26**, 732 (2009).

[43] C. T. Tai, *Dyadic Green's Functions in Electromagnetic Theory*, IEEE Press, New York, second edition, 1993.

[44] M. J. Mohlenkamp, *A fast transform for spherical harmonics*, J. Fourier Anal. Appl. **5**, 159 (1999).

[45] R. A. Satten, *Effects of atomic quadrupole moments upon the index of refraction*, J. Chem. Phys. **26**, 766 (1957).

[46] A. Alù and N. Engheta, *Guided propagation along quadrupolar chains of plasmonic nanoparticles*, Phys. Rev. B **79**, 235412 (2009).

[47] A. B. Evlyukhin, C. Reinhardt, U. Zywietz, and B. N. Chichkov, *Collective resonances in metal nanoparticle arrays with dipole-quadrupole interactions*, Phys. Rev. B **85**, 245411 (2012).

[48] E. D. Palik, *Handbook of Optical Constants of Solids*, Academic Press, Boston, 1985.

[49] A. Serdyukov, I. Semchenko, S. Tretyakov, and A. Sihvola, *Electromagnetics of Bi-anisotropic Materials: Theory and Applications*, Electrocomponent science monographs, Gordon and Breach Science, Amsterdam, The Netherlands, 1 edition, 2001.

[50] G. Dolling, C. Enkrich, M. Wegener, J. F. Zhou, C. M. Soukoulis, and S. Linden, *Cut-wire pairs and plate pairs as magnetic atoms for optical metamaterials*, Opt. Lett. **30**, 3198 (2005).

[51] V. D. Lam, J. B. Kim, S. J. Lee, Y. P. Lee, and J. Y. Rhee, *Dependence of the magnetic-resonance frequency on the cut-wire width ofcut-wire pair medium*, Opt. Express **15**, 16651 (2007).

[52] T. P. Meyrath, T. Zentgraf, C. Rockstuhl, and H. Giessen, *Electromagnetic induction in metamaterials*, Appl. Phys. B **93**, 107 (2008).

[53] T. H. Taminiau, S. Karaveli, N. F. van Hulst, and R. Zia, *Quantifying the magnetic nature of light emission*, Nat Commun **3**, 979 (2012).

[54] A. F. Koenderink and A. Polman, *Complex response and polariton-like dispersion splitting in periodic metal nanoparticle chains*, Phys. Rev. B **74**, 033402 (2006).

[55] X. Zheng, V. Volskiy, V. Valev, G. Vandenbosch, and V. Moshchalkov, *Line position and quality factor of plasmonic resonances beyond the quasi-static limit: A full-wave eigenmode analysis route*, J. Sel. Top. Quant. Electron. **19**, 4600908 (2013).

[56] S. Rodriguez, F. Bernal Arango, T. P. Steinbusch, M. Verschuuren, A. Koenderink, and J. Gómez Rivas, *Breaking the symmetry of forward-backward light emission with localized and collective resonances in magnetoelectric nanopyramid arrays*, submitted PRL (2014).

[57] R. V. Mehta, R. Patel, R. Desai, R. V. Upadhyay, and K. Parekh, *Experimental evidence of*

zero forward scattering by magnetic spheres, Phys. Rev. Lett. **96**, 127402 (2006).

[58] B. García-Cámara, F. Moreno, F. González, and J. M. Saiz, *Comment on "experimental evidence of zero forward scattering by magnetic spheres"*, Phys. Rev. Lett. **98**, 179701 (2007).

[59] A. Alù and N. Engheta, *How does zero forward-scattering in magnetodielectric nanoparticles comply with the optical theorem?*, J. Nanophot. **4**, 041590 (2010).

[60] B. Rolly, B. Stout, and N. Bonod, *Boosting the directivity of optical antennas with magnetic and electric dipolar resonant particles*, Opt. Express **20**, 20376 (2012).

8

Correcting the Super Polarizability for Antennas in Scattering Environments

In this chapter we extend our method of retrieving the super polarizability of antennas to deal with scatterers placed in non trivial surroundings. We show how to implement radiative corrections to the dipole-quadrupole model, when scatterers are placed near a surface, sphere, or stratified medium, similar to the known correction of dipole polarizabilities by the local density of optical states. We demonstrate how this model allows to interpret near field excitation data of plasmon structures taken on antennas deposited on a high-index substrate that present highly directional emission.

8.1   Introduction

In nano-optics one frequently relies on first developing intuition for the functioning of antennas or Fano-resonant structures when they are in isolation, to then explore the functioning of these structures in more complex geometries. Examples are the placement of antennas in arrays, or the placement of antennas on dielectric interfaces or stratified media. Regarding the latter example, the applications based on antennas placed on substrates are abundant. For instance, plasmon antennas are used on dielectric interfaces such as glass cover slips in microscopy experiments [1–4] and sensing applications, or on high index semiconductors, for example in LEDs (III-V substrates), and solar cell applications[5, 6]. Nevertheless, it is well known that the presence of a scattering environment could drastically change the response of the antennas. Therefore, the question arises of how to take this into account for when magneto electric dipolar and quadrupolar responding antennas are placed in such an environment. We solve this

issue by incorporating back-action effects that modify a scatterer when it is moved into a nontrivial photonic environment, such as the commonly encountered layered medium in LED and solar applications. This leads to a correction equivalent to the powerful "radiation damping corrections" for the dipole model. This radiation damping correction is fundamental to build an energy conserving multiple scattering theory [7–10]. We apply this insight to predict the response of large plasmon scatterers placed on top of a silicon substrate as encountered in recent cathodoluminescence experiments [11]. In particular, we predict strongly directive antenna action for locally excited large scatterers as consequence of the fact that the nearby interface enhances the magnetic and quadrupolar response.

8.2 Back-action correction for hybridization with environments
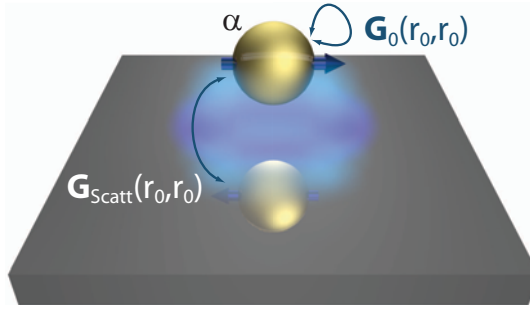
Figure 8.1: Sketch of the self driving on an electrically polarizable particle produced by the reflection of fields created by an interface.

Here we ask if an extracted superpolarizability for a complex antenna in isolation can be used as input for a predictive model where the antenna is placed in a complicated environment. In the dipole approximation the environment can be taken into account in the electric dipole polarizability by including induced self interactions produced by the environment, as depicted in Fig. 8.1. In this example an electric dipole

$$\mathbf{p} = \alpha \cdot \mathbf{E}_{\text{total}}(\mathbf{r}_0) = \alpha \cdot (\mathbf{E}_{\text{in}}(\mathbf{r}_0) + \mathbf{E}_{\text{scatt}}(\mathbf{r}_0)), \tag{8.1}$$

is driven in a scatterer with polarizability α by an electric field $\mathbf{E}_{\text{total}}$ at the position of the scatterer $\mathbf{r}_0$. The total electric field is a sum of the incident electric field $\mathbf{E}_{\text{in}}$ plus the scattered electric field $\mathbf{E}_{\text{scatt}}$. In the case of an environment with a substrate the scattered electric field would be the reflected field by the substrate. The scattered electric field created by the dipole, due to the substrate is given by

$$\mathbf{E}_{\text{scatt}}(\mathbf{r}_0) = \omega^2 \mu \mu_0 (\overline{\mathbf{G}}_{\text{scatt}}(\mathbf{r}_0, \mathbf{r}_0)) \cdot \mathbf{p} \tag{8.2}$$

where $\overline{\mathbf{G}}_{\text{scatt}}$ is the scattering part of the Green's function for the electric field. By introducing Eq. (8.2) in Eq. (8.1) we obtain:

$$\mathbf{p} - \alpha \omega^2 \mu \mu_0 \overline{\mathbf{G}}_{\text{scatt}}(\mathbf{r}_0, \mathbf{r}_0) \cdot \mathbf{p} = \alpha \cdot \mathbf{E}_{\text{in}}(\mathbf{r}_0). \tag{8.3}$$

Therefore we can define a corrected polarizability in the following manner:

$$\alpha_{\text{corr}} = (\overline{\mathbf{I}} - \alpha \omega^2 \mu \mu_0 \overline{\mathbf{G}}_{\text{scatt}}(\mathbf{r}_0, \mathbf{r}_0))^{-1} \cdot \alpha \tag{8.4}$$

or using the matrix identity $(\overline{\mathbf{A}} \cdot \overline{\mathbf{B}})^{-1} = \overline{\mathbf{B}}^{-1} \cdot \overline{\mathbf{A}}^{-1}$ we can rewrite it as:

$$\alpha_{\text{corr}}^{-1} = (\alpha^{-1} - \omega^2 \mu \mu_0 (\overline{\mathbf{G}}_{\text{scatt}}(\mathbf{r}_0, \mathbf{r}_0)). \tag{8.5}$$

The corrected polarizability is equal to the original polarizability of the particle plus a self interaction term that is essentially the scattered Green function of the embedding medium [12–15]. This term naturally includes radiation damping and a reactive shift in the polarizability due to the environment. This correction is of large use, as it allows us to quantitatively predict the response of arbitrary antenna geometries in complex backgrounds using as input single building blocks for which the free space polarizability is already tabulated. Here we derive a similar correction for the superpolarizability. In

$$\begin{pmatrix} \mathbf{p} \\ \mathbf{m} \\ \mathbf{Q} \end{pmatrix} = \overline{\alpha}^{\mathbf{S}} \begin{pmatrix} \mathbf{E} \\ \mathbf{H} \\ \lozenge \mathbf{E} \end{pmatrix} \tag{8.6}$$

one should take into account that the driving field $(\mathbf{E}, \mathbf{H}, \lozenge \mathbf{E})$ should not just be the incident field, but also the field that comes back via interaction with the background to the scatterer, as quantified by the *scattered* part of the Green's function of the background system. Thus the *total* field reads

$$\begin{pmatrix} \mathbf{E} \\ \mathbf{H} \\ \lozenge \mathbf{E} \end{pmatrix} = \begin{pmatrix} \mathbf{E}_0 \\ \mathbf{H}_0 \\ \lozenge \mathbf{E}_0 \end{pmatrix} +$$

$$\begin{pmatrix} a_1 \overline{\mathbf{G}}_E \cdot \mathbf{p} + a_2 \nabla \times \overline{\mathbf{G}}_H \cdot \mathbf{m} + a_3 (\lozenge' \overline{\mathbf{G}}_E^T)^T \cdot \mathbf{Q} \\ \frac{a_1}{i\omega\mu\mu_0} \nabla \times \overline{\mathbf{G}}_E \cdot \mathbf{p} + a_4 \overline{\mathbf{G}}_H \cdot \mathbf{m} + \frac{a_3}{i\omega\mu\mu_0} \nabla \times (\lozenge' \overline{\mathbf{G}}_E^T)^T \cdot \mathbf{Q} \\ a_1 \lozenge \overline{\mathbf{G}}_E \cdot \mathbf{p} + a_2 \lozenge (\nabla \times \overline{\mathbf{G}}_H) \cdot \mathbf{m} + a_3 \lozenge (\lozenge' \overline{\mathbf{G}}_E^T)^T \cdot \mathbf{Q} \end{pmatrix} \tag{8.7}$$

where in the SI unit system $a_1 = \omega^2 \mu \mu_0$, $a_2 = i\omega$, $a_3 = a_1/6$, $a_4 = \omega^2 \varepsilon \varepsilon_0$. This result combines the magnetoelectric Green dyadic [16] with the electric field radiated by a quadrupole[17, 18] $\mathbf{Q}$ that is given by $\mathbf{E}(\mathbf{r}) = (1/6)\omega^2 \mu_0 \mu (\lozenge' \overline{\mathbf{G}}_E^T (\mathbf{r}, \mathbf{r}'))^T \cdot \mathbf{Q}$. Equation (8.6) is of the form $\mathscr{P} = \overline{\alpha}^{\mathbf{S}} [\mathscr{E}_0 + \mathscr{G} \mathscr{P}]$, where $\mathscr{P}$ is the generalized induced moment, $\mathscr{E}_0$ is the driving field, and $\mathscr{G}$ is a generalized field propagator which includes the Green's function, the curl of the Green's function as well as its symmetric gradients. Hence the corrected polarizability defined through $\mathscr{P} = \overline{\alpha}^{\mathbf{S}}_{\text{corrected}} \mathscr{E}_0$ must be of the

familiar form $\overline{\alpha}_{\mathbf{corrected}}^{\mathbf{S}}{}^{-1} = \overline{\alpha}^{\mathbf{S}^{-1}} - \mathcal{G}$. Explicitly, we define the corrected $\overline{\alpha}_{\mathbf{corrected}}^{\mathbf{S}}$ tensor as

$$\overline{\alpha}_{\mathbf{corrected}}^{\mathbf{S}}{}^{-1} = \overline{\alpha}^{\mathbf{S}^{-1}} - ...$$
$$\begin{pmatrix} a_1 \overline{\mathbf{G}}_E & a_2 \nabla \times \overline{\mathbf{G}}_H & a_3 (\hat{\Diamond}' \overline{\mathbf{G}}_E^T)^T \\ \frac{a1}{i\omega\mu\mu_0} \nabla \times \overline{\mathbf{G}}_E & a_4 \overline{\mathbf{G}}_H & \frac{a_3}{i\omega\mu\mu_0} \nabla \times (\hat{\Diamond}' \overline{\mathbf{G}}_E^T)^T \\ a_1 \hat{\Diamond} \overline{\mathbf{G}}_E & a_2 \hat{\Diamond} (\nabla \times \overline{\mathbf{G}}_H) & a_3 \hat{\Diamond} (\hat{\Diamond}' \overline{\mathbf{G}}_E^T)^T \end{pmatrix} \quad (8.8)$$

where the actual inversion again requires first casting to the 11x11 form as outlined in section 7.2, and also it requires to use the operator $\hat{\Diamond}$ which is defined as $\hat{\Diamond}\mathbf{E} = \{(\partial_x E_y + \partial_y E_x)/2, (\partial_x E_z + \partial_z E_x)/2, (\partial_y E_z + \partial_z E_y)/2, (\partial_x E_x - \partial_z E_z), (\partial_y E_y - \partial_z E_z)\}$. In absence of quadrupolar contributions, this correction reduces to the magnetoelectric radiation damping correction derived for metamaterials by Belov [9] and Seršic [16], which in itself is a generalization of the Sipe-Kranendonk formalism [10]. Note that owing to the required matrix inverse, a nontrivial environment such as a nearby surface can *induce* magnetoelectric cross coupling [19], as well as mixing of dipolar and quadrupolar excitations. As a final comment, it is very important to emphasize that here we only use the scattered part of the Green's functions, unlike Ref. [9] and [16]. The retrieved superpolarizabilities already include the self-polarization due to free space and the only additional correction needed is for the polarization created by the reflections and scattering of the new environment which are included in the scattered part of the Green's function.

8.3 Single particle on a Si substrate as directional antenna

We apply the correction of the superpolarizability tensor due to a silicon substrate to a simple experiment recently performed in cathodoluminescence, on Au disks on a Si substrate [11] of height 80 nm and varying diameter up to 180 nm. We retrieve the superpolarizability for the biggest particle with height 80 nm and 180 nm diameter in a vacuum environment, and subsequently we correct α^S with the back-action correction (evaluated at mid-height, *i.e.*, 40 nm above the silicon substrate).

Figure 8.2b and c summarizes as color plots the α^S, before and after the correction, taking as wavelength 565 nm, and again scaling the superpolarizability tensor elements (Methods, section 7.2) such that equal value means equal scattered power. As for the dolmen (section 7.3), here we present a logarithmic color plot to facilitate quick identification of relevant entries; the appendix C provides numerical values. In absence of the substrate, the particle response is dominated by a strong electric polarizability along the three principal particle axes. Here x and y are strictly degenerate by symmetry, while the polarizability along z is somewhat lower with a ratio of 0.34 owing to the smaller height. Evidently, the isolated disk has a significant magnetic dipole response and quadrupolar response owing to the big disk size. The particle symmetry,

however, implies absence of bianisotropy. Clearly once the disk is brought to the substrate, the substrate induces cross coupling between different elements, namely bianisotropy linking electric and magnetic dipoles (p_x and m_y), and coupling of dipolar and quadrupolar responses.
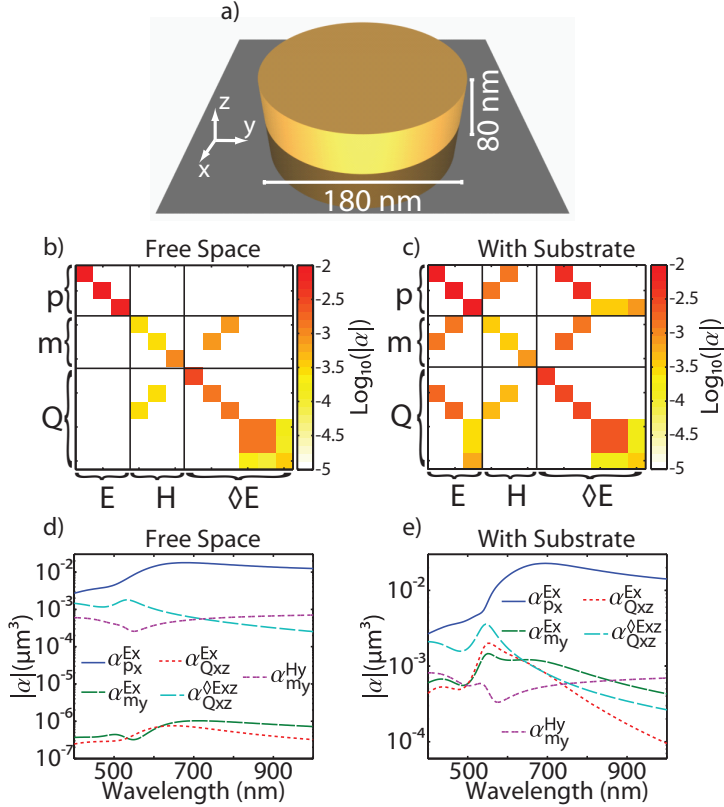

Figure 8.2: a) Magnitude of the elements of the superpolarizability tensor for a gold cylinder with 180 nm diameter and 80 nm height at a wavelength of 565 nm. b) Magnitude of the elements of the superpolarizability tensor corrected for the presence of a silicon substrate. c, d) Magnitude of the different elements of the α^S-tensor vs. wavelength, for the free space case and the α^S tensor corrected for the backaction due to the presence of a silicon substrate.

To gain more insight, we highlight the polarizability tensor elements that are relevant in a typical normal incidence scattering experiment, i.e, when impinging along the 'z' direction with an 'x' polarized plane wave. The most important elements in the super polarizability tensor that play a role, *i.e.*, $\alpha_{p_x}^{E_x}$, $\alpha_{m_y}^{E_x}$, $\alpha_{m_y}^{H_y}$, and $\alpha_{Q_{xz}}^{E_x}$ are plotted as function of wavelength in Fig. 8.2d (see methods in Sec. 7.2). For the particle in free space, the strongest contribution to the scattering is simply the purely electric dipolar

response $\alpha_{p_x}^{E_x}$, with a maximum of 1.8×10^{-2} μm^3 at a wavelength of 680 nm. The next important terms, *i.e.*, the magnetic dipole response $\alpha_{m_y}^{H_y}$ and electric quadrupole $\alpha_{Q_{xz}}^{\Diamond E_{xz}}$ are 10 to 100 times smaller, while the off-diagonal cross polarizability is another factor of 100 to 1000 smaller still.

Once the scatterer is placed on the substrate, the back action correction modifies this ordering. Fig. 8.2e reveals that the electric polarizability is enhanced and shifted in resonance due to its interaction with the silicon substrate. Remarkably, the crosspolarizability $\alpha_{m_y}^{E_x}$ and hyperpolarizability $\alpha_{Q_{xz}}^{E_x}$ are enhanced by 3 to 4 orders of magnitude, thus allowing electric fields to much more efficiently excite magnetic dipoles and quadrupoles. The physics is that if initially an electric dipole is induced in the scatterer, its image dipole has sufficient gradient for driving quadrupoles and the magnetic dipole. For the corrected case we present the values of the different elements of α^S in appendix C. On basis of recent experiments and theoretical proposals, it is
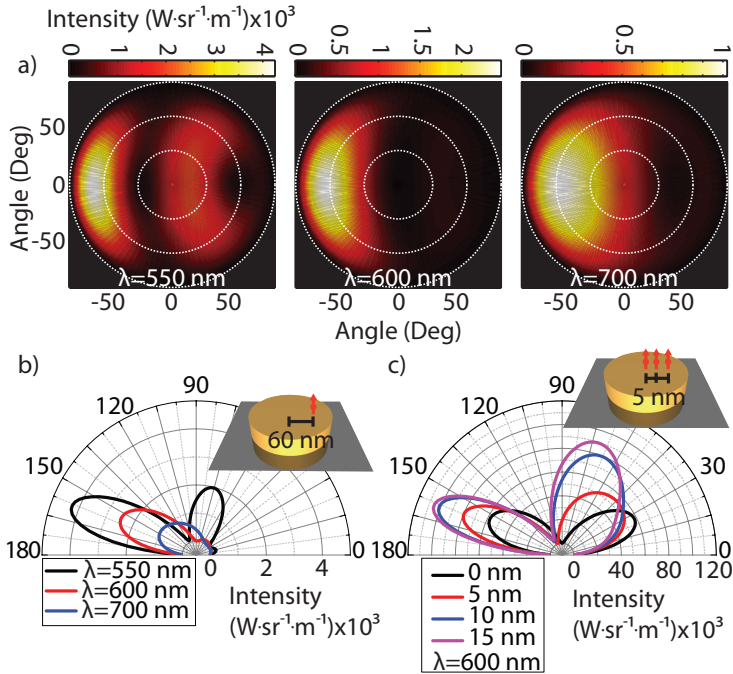
Figure 8.3: a) Emission patterns for a gold cylinder antenna excited with a dipolar emitter locater 40 nm above the point dipole-quadrupole and 60 nm off axis. The three graphs present 3 different wavelengths 550, 600 and 700 nm. The three white circles display the angles for 30, 60 and 90 degrees. b) Cross cuts of the $|E|^2$ emission patterns of figure a). c) Polar plots of the radiated intensity by the cylindrical antennas when excited with a electrical dipolar emitter located at different positions from the center of the antenna.

expected that if one actually manages to excite magnetic dipole moments and electric quadrupoles as strongly as the fundamental electric dipole term, one can engineer complicated and directional radiation patterns [4, 20–22]. Here we predict that if the Au antenna on silicon that we analyzed is excited with a localized source, as in cathodoluminescence, strongly directional radiation patterns indeed emerge. We predict these radiation patterns simply from two ingredients: the free-space superpolarizability, and the known interface Green's function [8], *i.e.*, without any recourse to a full wave solution beyond extraction of the superpolarizability of the disk in free space. To obtain a prediction, we simply take as driving field the field (*i.e.*, $\mathbf{E}, \mathbf{H}$ and $\lozenge\mathbf{E}$) of an electric dipole emitter as given by the known interface Green function. Next, we calculate the induced moments by multiplication of the driving field with the substrate-corrected superpolarizability tensor. Finally we find the far field radiation pattern by coherent addition of the known far fields of the induced moments, for which asymptotic expansions are likewise textbook material [8].

In Fig. 8.3a we show the total field intensity squared ($|E|^2$) for the cylindrical Au antenna excited with a dipolar emitter with strength p_0, located 60 nm off axis, from the center of the cylinder, and 40 nm above the center of the multipolar scatterer antenna. Fig. 8.3a shows results for three driving wavelengths, namely 550 nm, 600 nm and 700 nm, which are the resonant wavelengths of the quadrupoles, in-plane electric dipole and out of plane electric dipole respectively. These figures together with the cross-cuts shown in Fig. 8.3b show how we can achieve a very strong directional emission with only one single particle. The strong directionality results from coherent superposition of the electric dipole, magnetic dipole, and electric quadrupole terms that are excited in such a ratio as to yield comparable far field flux. For instance, in the first panel of Fig. 8.3a the antenna acquires an electric dipole of $|p_x|=1.69p_0$, $|p_z|=1.56p_0$ and a magnetic dipole of $|m_y|=1.17p_0$ while the dominating acquired quadrupoles have a magnitude of $|Q_{xx}|=3.86p_0$, $|Q_{yy}|=3.61p_0$, and $|Q_{xz}|=2.09p_0$ demonstrating how a localized dipolar source can excite quadrupolar moments in single elements antennas whose radiating power exceed the radiated power from the dipolar moments.

Finally, we sweep the position of the dipole over the antenna, starting from the center moving in steps of only 5 nm. We find (Fig.8.3c) that the angular emission changes drastically with the position of the emitter with respect to the antenna. For instance, viewing emission under a 70° angle relative to the substrate, it is possible to acquire a signal that changes up to 15% between two given points *per nm* of lateral position shift of the excitation source. This effect could allow using simple gold antennas on a substrate as sensitive position detectors of fluorescent molecules with resolutions better than those of STORM [23] and PALM [24] microscopy. This ultra-high sensitivity to position of a source relative to an antenna is similar in concept to a recent proposal to use a notched high index dielectric sphere with an overlapping electric and magnetic resonance [21]. However, from the practical side, fabricating an Au cylinder on a Si substrate is far simpler than preparing notched high index Mie spheres.

Measurements

To complement the theoretical discussion we present experimental results of directionality measurements performed by Toon Coenen of cylindrical gold antennas excited with a localized source. To measure these antennas we use a tightly focused 30 keV electron beam as local excitation source to drive the cylindrical Au nanoantennas. The electromagnetic field created by electron beam provides a broadband and very localized source (~10 nm). This source allows one to do in a single experiment very fine spatially resolved measurements over a broad spectral range and to determine the scattering properties of very small nano antennas.
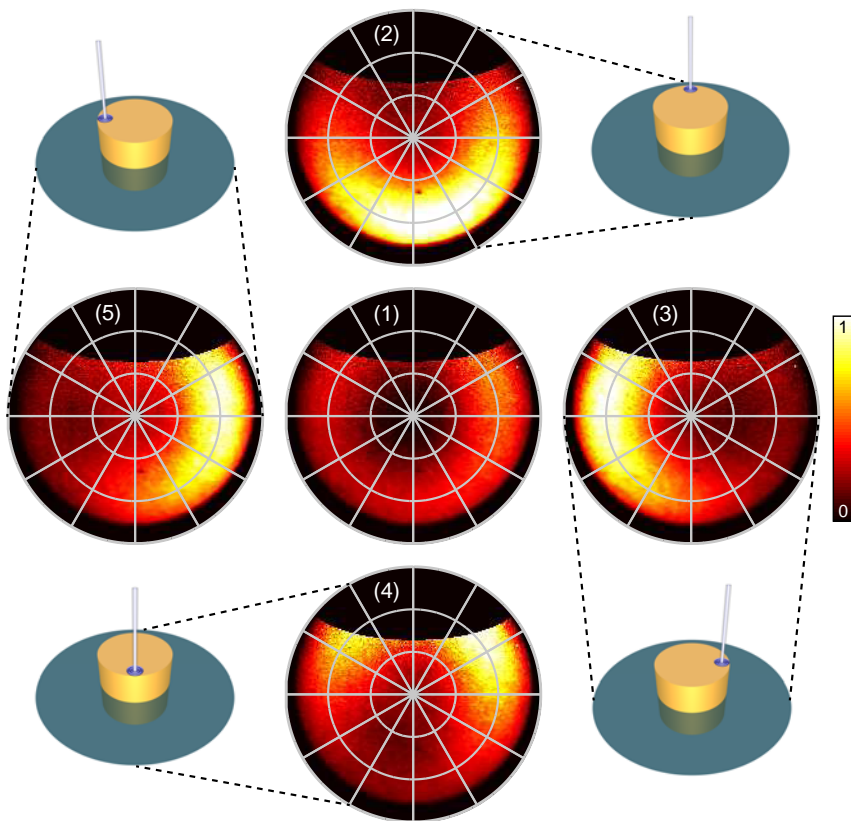
Figure 8.4: Experimental normalized angular CL emission patterns collected from a pillbox shaped particle with a diameter of 180 nm and a height of 80 nm. The patterns are shown at $\lambda = 600$ nm for excitations at the center of the particle, shown in fig (a), and for excitations near the edge of the particle for four angles: $0°$ (b), $90°$ (c), $180°$ (d) and $270°$ (e). The excitation positions are indicated by the cartoons next to the radiation patters. The patterns have been normalized to the maximum intensity value for all five patterns to show the relative brightness for different excitation positions.

Cylindrical gold nanoparticles like the ones discussed in Sec. 8.3 were fabricated with diameters ranging from 50-180 nm in 5 nm steps and a height of 80 nm on a crystalline silicon substrate using electron beam lithography, thermal evaporation and a lift-off procedure. For these measurements light is collected by a half parabolic mirror which is placed between the sample and the electron microscope pole piece. This mirror directs the light either to a grating spectrometer, or to a 2D CCD camera. Therefore at each excitation position one either can collect a spectrum in the visible/nearinfrared spectral region, or an image with the information of the scattering directivity. For all the measurements a beam current of 0.8 nA was used.

To measure the far-field angular emission patterns the beam coming from the parabolic mirror was projected onto the CCD camera, to obtain the angular emission distribution. This technique has already been used and is explained in detail in Ref. [25]. Angular patterns are collected for free-space wavelengths (λ) from 400 to 750 nm using 40 nm band pass filters for all disk diameters. We will further discuss only the 180 nm disk. To optimize the signal-to-noise ratio, 120 s integration times were used for λ =400, 450, 700 and 750 nm and 60 s for λ =500-650 nm.

Fig. 8.4 shows the angular pattern for a λ =180 nm particle at λ =600 nm for excitation on four orthogonal edge positions of the nanodisk as depicted in the insets. The pattern clearly shows that the radiation patterns present strong angular asymmetries and that the particle radiates away from the excitation point when excited at the edges. If the nanodisk is excited in the center the emission intensity is lower and as expected based on symmetrical consideration the the emission is azimuthally symmetric.

We continue by studying the angular emission distribution for different wavelengths. Fig. 8.5 shows normalized angular patterns for λ =400-600 nm for the particle disk for edge excitation on the left side. The pattern for λ =400 nm shows a strong radiation lobe directed to the zenith. The relative contribution of this lobe strongly decreases for longer wavelength while the sideward lobe becomes dominant. At λ =600 nm the forward scattering ratio is maximum and most of the radiation is emitted into one strong crescent-shaped lobe pointing away from the excitation position as the one shown in Fig. 8.4.

In order to unravel the multipolar composition of complex scattering phenomena several groups have opted to fit emission patterns to superpositions of multipole radiation patterns [4, 22, 26]. By using the knowledge obtained in Sec. 8.3 we can discriminate based on symmetry considerations of the excitation field and the superpolarizability tensor which are the main multipolar contributions to the scattering process. More specifically, and although the field obtained with the e-beam is not trivial to calculate, based on symmetry consideration we know that this excitation possess an electric field in the z and x directions $\mathbf{E} = \mathbf{E}_x + \mathbf{E}_z$, a magnetic field in the y direction $\mathbf{H} = \mathbf{H}_y$ and a gradient of the electric field along the 'xz' plane as well as one on the 'xy' plane which is 45° rotated $\Diamond\mathbf{E} = \Diamond\mathbf{E}_{xz} + \Diamond\mathbf{E}_{xx} + \Diamond\mathbf{E}_{yy}$. The presence of all these fields can also be inferred by finding what are the fields created by a 'z' oriented electrical dipole, which share the same symmetries as the electron beam excitation. These fields when multiplied by the superpolarizability tensor indicate which are the multipolar moments involved in the scattering process i.e. p_z, p_x, m_y, Q_{xz} and a symmetrical

combination of $Q_{xx} + Q_{yy}$ (which gives us a quadrupole in plane as Q_{xy} but rotated 45°). We single out these components to then fit the data. The results of the fitting procedure are presented in Fig. 8.5b. It is evident that the correspondence is very good. Therefore we can be confident that the superpolarizability tensor pinpoints in an elegant and straightforward way which are the only elements needed to understand the scattering process.

We believe that the reason why these radiation patterns differ from the ones presented in Fig. 8.3 is that we do not have an accurate description of the magnitude and relative contributions of the electric and magnetic fields for the electron beam induced field, which is different from an excitation generated by an electric dipole. For completeness in Fig. 8.5c we present the radiation patterns of the multipole moments involved in the scattering process. The measurements together with the
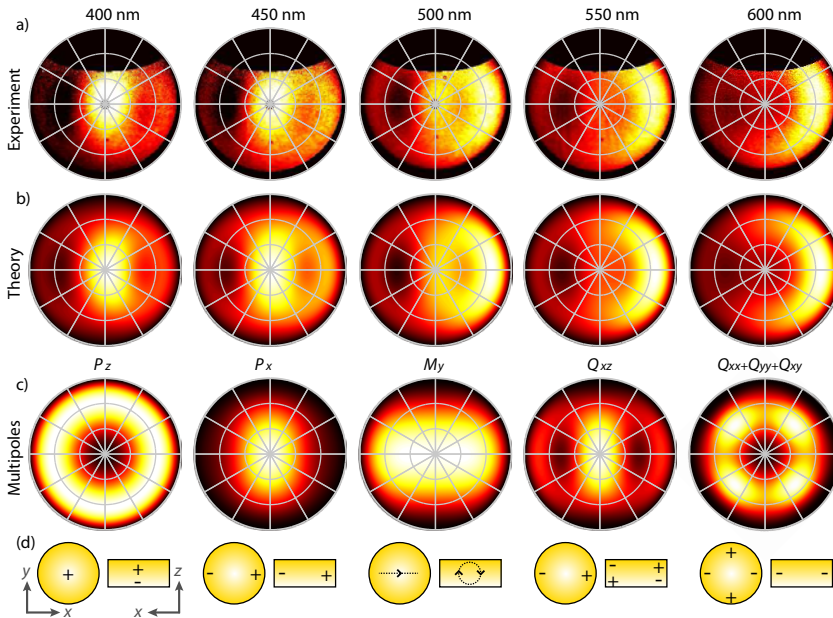
Figure 8.5: Figure a) shows the measured experimental CL radiation patterns, while figure b) shows the numerically fitted theoretical patterns for a D=180nm Au disk excited on the 'left' side for λ=400-600 nm. These patterns are a result of the coherent interference of five multipole components. Figure c) shows the theoretical radiation patterns for the individual multipolar components that compose the resonances in the cylinder. These radiation patterns are calculated for λ =500nm when the multipoles are placed 40 nm above a silicon substrate. As a last panel in d) we show the corresponding charge distribution of the multipoles used. Two perspectives are used for showing the charge distributions. First, we show a top view of the disk on the left and second we show a cross section of the disk in the 'xz' plane, presented on the right.

theory demonstrate that the knowledge of the superpolarizability tensor for a given

structure offers a deeper insight to the complex scattering processes happening in antennas. In the case of the cylindrical antenna we show how a careful balance between the multipoles involved in scattering can give rise to an interesting "lighthouse" effect. This effect, where we can define the direction of emission by nanometric tuning of the excitation can be useful for novel types of sensors and to control directionality of LEDS and lasers.

8.4 Conclusions

To summarize, we have shown how to predict the scattering properties of a building block in a complex environment on basis of on one hand the free space building block superpolarizability and on the other hand the environment Green function. As an example we use an Au cylinder big enough to support dipolar and quadrupolar resonances placed on top of a silicon substrate. We have shown that this particle is capable of sustaining very directional scattering when driven by a localized source. This directionality is shown to be fostered by the strong interaction of the dipolar and quadrupolar resonances. The type of study presented in this chapter and performed on the Au cylinder will have a large impact on the quantitative modeling of plasmon and dielectric antennas in typical applications for solar cells, LEDs and sensors, where antennas always function in a complicated dielectric environment. Importantly, we emphasize that the complex environment can induce or enhance particular multipolar moments, yielding new methods to control directionality of scattering and emission.

References

[1] P. Anger, P. Bharadwaj, and L. Novotny, *Enhancement and quenching of single-molecule fluorescence*, Phys. Rev. Lett. **96**, 113002 (2006).

[2] S. Kühn, U. Håkanson, L. Rogobete, and V. Sandoghdar, *Enhancement of single-molecule fluorescence using a gold nanoparticle as an optical nanoantenna*, Phys. Rev. Lett. **97**, 017402 (2006).

[3] A. G. Curto, G. Volpe, T. H. Taminiau, M. P. Kreuzer, R. Quidant, and N. F. van Hulst, *Unidirectional emission of a quantum dot coupled to a nanoantenna*, Science **329**, 930 (2010).

[4] A. G. Curto, T. H. Taminiau, G. Volpe, M. P. Kreuzer, R. Quidant, and N. F. van Hulst, *Multipolar radiation of quantum emitters with nanowire optical antennas*, Nat Commun **4**, 1750:1 (2013).

[5] S. Pillai, K. R. Catchpole, T. Trupke, and M. A. Green, *Surface plasmon enhanced silicon solar cells*, Journal of Applied Physics **101**, 093105 (2007).

[6] H. A. Atwater and A. Polman, *Plasmonics for improved photovoltaic devices*, Nat Mater **9**, 205 (2010).

[7] F. J. García de Abajo, *Colloquium: Light scattering by particle and hole arrays*, Rev. Mod. Phys. **79**, 1267 (2007).

[8] L. Novotny and B. Hecht, *Principles of Nano-optics*, Cambridge University Press, Cambridge, 2006.

[9] A. Belov, S. I. Maslovski, K. R. Simovski, and S. A. Tretyakov, *A condition imposed on the electromagnetic polarizability of a bianisotropic lossless scatterer*, Tech. Phys. Lett. **29**, 718 (2003).

[10] J. E. Sipe and J. V. Kranendonk, *Macroscopic electromagnetic theory of resonant dielectrics*, Phys. Rev. A **9**, 1806 (1974).

[11] T. Coenen, F. Bernal Arango, A. Femius Koenderink, and A. Polman, *Directional emission from a single plasmonic scatterer*, Nat Commun **5**, (2014).

[12] B. C. Buchler, T. Kalkbrenner, C. Hettich, and V. Sandoghdar, *Measuring the quantum efficiency of the optical emission of single radiating dipoles using a scanning mirror*, Phys. Rev. Lett. **95**, 063003 (2005).

[13] F. Bernal Arango, A. Kwadrin, and A. F. Koenderink, *Plasmonic antennas hybridized with dielectric waveguides*, ACS Nano **6**, 10156 (2012).

[14] M. Frimmer and A. F. Koenderink, *Superemitters in hybrid photonic systems: A simple lumping rule for the local density of optical states and its breakdown at the unitary limit*, Phys. Rev. B **86**, 235428 (2012).

[15] M. Frimmer, T. Coenen, and A. F. Koenderink, *Signature of a fano resonance in a plasmonic metamolecule's local density of optical states*, Phys. Rev. Lett. **108**, 077404 (2012).

[16] I. Sersic, C. Tuambilangana, T. Kampfrath, and A. F. Koenderink, *Magnetoelectric point scattering theory for metamaterial scatterers*, Phys. Rev. B **83**, 245102 (2011).

[17] V. V. Klimov and M. Ducloy, *Quadrupole transitions near an interface: General theory and application to an atom inside a planar cavity*, Phys. Rev. A **72**, 043809 (2005).

[18] M. Ribaric and L. Sustersic, *Expansion in terms of moments of time-dependent, moving charges and currents*, SIAM J. Appl. Math. **55**, 593 (1995).

[19] A. Kwadrin and A. F. Koenderink, *Probing the electrodynamic local density of states with magneto-electric point scatterers*, Phys. Rev. B **86**, 125123 (2013).

[20] B. Rolly, B. Stout, and N. Bonod, *Boosting the directivity of optical antennas with magnetic and electric dipolar resonant particles*, Opt. Express **20**, 20376 (2012).

[21] A. Krasnok, D. Filonov, A. Slobozhanyuk, C. Simovski, P. Belov, and Y. Kivshar, *Superdirective dielectric nanoantennas with effect of light steering*, arXiv:1307.4601v1 , 8 (2013).

[22] I. M. Hancu, A. G. Curto, M. Castro-López, M. Kuttge, and N. F. van Hulst, *Multipolar interference for directed light emission*, Nano Letters **14**, 166 (2014).

[23] M. J. Rust, M. Bates, and X. Zhuang, *Sub-diffraction-limit imaging by stochastic optical reconstruction microscopy (storm)*, Nat Meth **3**, 793 (2006).

[24] E. Betzig, G. H. Patterson, R. Sougrat, O. W. Lindwasser, S. Olenych, J. S. Bonifacino, M. W. Davidson, J. Lippincott-Schwartz, and H. F. Hess, *Imaging intracellular fluorescent proteins at nanometer resolution*, Science **313**, 1642 (2006).

[25] T. Coenen, E. J. R. Vesseur, and A. Polman, *Angle-resolved cathodoluminescence spectroscopy*, Applied Physics Letters **99**, (2011).

[26] T. H. Taminiau, S. Karaveli, N. F. van Hulst, and R. Zia, *Quantifying the magnetic nature of light emission*, Nat Commun **3**, 979 (2012).

9

Applications

This chapter discusses possible applications inspired by this thesis. In particular, a large part of this thesis was devoted to waveguide-integrated plasmonic antennas to combine the local field enhancement of plasmon antennas with lossless propagation in integrated optics. As demonstrated in chapter 2 and 3 the system composed by antennas on waveguides allows us to measure scattering out of plane from antennas with a very low background signal. Because of this dark field character one can measure scattering spectra of single nano-rod antennas with a very low integration time on a common silicon detector. Also by measuring the transmission through the waveguide we could determine how the antenna scattering affects the waveguide transmission spectrally. Both characteristics depend on the scattering resonance of the antenna and therefore can be controlled by the antenna design. A depiction of these properties is shown in Fig. 9.1. This figure also shows that resonances of the antennas create strong confinement in small volumes of high electromagnetic fields (hot-spots). The properties of low-background efficient detection by out of plane detectors, and the possibility of completely waveguide-integrated excitation and detection of plasmon resonances spur a varied number of possible applications.

9.1 Chemical and biological detection fluidic environment

By functionalizing gold antennas on waveguides and integrating the system in a fluidic environment one can envision the detection out of plane as well as through waveguides of chemical and biological samples in very small volumes and very low concentrations. During our work for this thesis we developed PDMS fluidic cells that can be pressed
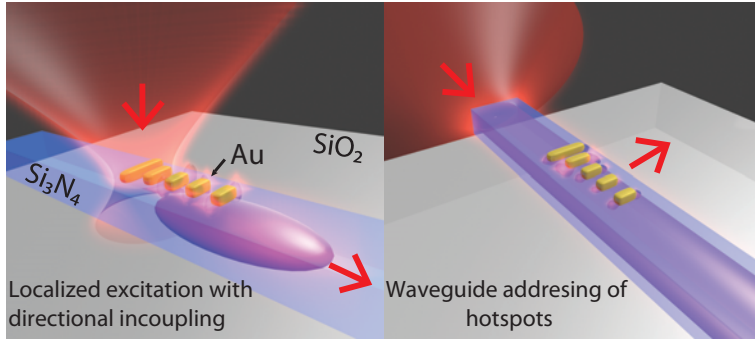
Figure 9.1: Sketch of some of the possible capabilities attained with phased array antennas on waveguides.

on top of the waveguide so that the effect of different fluids as well as solutes dissolved in the fluid could be measured, for instance by monitoring transmission through the waveguide. Also fluidic cells integrated with on chip waveguides are commercially available from LIONIX BV for "lab-on-chip" applications. These cells provide the means to bring liquid carrying analytes close to the antennas on waveguides. The presence of a chemical or biological sample that is brought in close proximity to the antenna can be detected in different ways. One method is based on fluorescence of the analyte. In this case the analyte can be optically pumped though the waveguide or with an excitation beam perpendicular to the substrate and the signal could be measured through the waveguide. This signal is therefore seen as an increase in intensity on a spectrally filtered photodetector integrated on or with the waveguide. A difficult challenge to overcome when performing both the addressing and the readout through the waveguide in a completely integrated fashion, is that fluorescence from the waveguide material itself can obscure the analyte signal. In our investigations we observed that when measuring transmission through LPCVD deposited Si_3N_4 waveguides with milliwatts of CW laser illumination this effect was not important. Nevertheless when measuring with a pulsed laser with $\lambda = 640$ nm, 80 picosecond pulse length and an average power in the milliwatts regime and repetition rates of tens of MHz then fluorescence from the waveguide became apparent. The second method is based on the fact that the scattering properties of a nano-antenna change as function of refractive index changes in the medium surrounding the antenna, particularly in the volume of enhanced near-field. Analytes with a different refractive index (or polarizability per volume) than the solvent would thereby cause a fluctuating optical signal as they diffuse into, and out of, the antenna near field. This change in n in the antenna near field causes two different effects that could be measured. On the one hand in a phased array antenna a Δn would change the directionality of the scattered light out of the guided mode. Thus, this signal can be measured through an intensity change on a photodetector. On the other hand this signal could be seen in transmission both by measuring the spectra through the waveguide and by a change in intensity of a

monochromatic source spectrally positioned at a flank of the spectral feature created by the presence of the antenna. This method may provide a measurement device capable of measuring the presence of *single* molecules as demonstrated in Ref. [1] but with the advantage of being based on an integrated on-chip platform.

## 9.2 Antennas and single emitters

A concept that is taking increasingly more importance in the field of quantum information is the quantum internet [2]. The idea is to connect objects or systems that behave quantum mechanically. Connections between these objects should, in a reversible way, be able to convert quantum states from one system to the quantum states of another system. These quantum interconnections would allow the distribution and teleportation of quantum states among the different nodes of the network and have a multi-node entanglement across the network. A candidate for such an interconnect is based on the coupling of single photons and single degrees of freedom in matter, such as electron spin, or electronic excitation in atoms, molecules, or quantum dots. One of the problems of this idealized system is that photons interact weakly with matter as already explained in chapter 1 of this thesis. In order to overcome this issue, many efforts are directed towards photonic crystal waveguides and coupled photonic crystal cavities in III-V semiconductors [3, 4], while for use of other emitters plasmonic nanowires have been proposed [5–7]. As alternative to the highly lossy transport of light in nanowires, we propose to exploit plasmonic antennas on waveguides. This system, on the one hand, would increase the interaction between photons and matter due to the strong field confinement of the antennas in the vicinity of strategically positioned atoms, NV-centers, molecules or quantum dots. On the other hand by using waveguides for this network photons could be transported losslessly between nodes. We have theoretically shown in chapter 3 that by positioning single atoms, NV-centers, molecules or quantum dots in the vicinity of an antenna on a waveguide it is possible to couple the emitted light from the single quantum emitter into the waveguide and direct it towards an integrated detector. The directional coupling to the waveguide was experimentally demonstrated in chapter 3 of this thesis. Also, the theory with which we understand and design these antennas was used to understand the response of Yagi-Uda antennas due to a very localized excitation similar to the one produced by a single emitter (chapter 4). Thus, we believe phased array antennas as well as quadrupolar antennas in combination with waveguides could find an application in the efficient coupling of single photons into integrated optical chips. One of the main problems for this idea is that with gold antennas the emission incoupling into the waveguide was theoretically predicted to be around 60% which is far from ideal for scalability of the system and which therefore would be far from the read-out efficiencies of 84% achieved for cavity systems (Ref. [8]). Nevertheless we believe that arrays of quadrupolar antennas may increase this coupling due to the strong near field gradients and better matching to the waveguide modes. Furthermore, hybrid structures of plasmon antennas coupled to moderate Q-cavities could alleviate the drawbacks of plasmonics while removing

the scaling problems that ultra high Q resonators suffer due to their sensitivity to fluctuations in environment and fabrication.

9.3 On-chip integrated Coulomb-blockade photon sources

Hot electrons are electrons in a material with energy in excess of the Fermi energy [9]. These electrons can be created or injected into a material in different ways, for instance by the absorption of a photon or by tunneling electron transport. Hot electrons are drawing attention lately in the field of plasmonics, for instance for their use in plasmon based detectors [10], but also for the generation of photon sources by injection of hot electrons into metal antennas [11]. We propose to use hot electrons to create a single photon source introducing single hot electrons into the metallic feed element of a Yagi-Uda antenna by using an intermediate step employing small (<5 nm) metallic islands between electrical contacts and the feed element of the antenna. Due to the Coulomb charging effect one could envision that only a single electron at a time tunnels, resulting in the possibility of single photon generation, where single photons would be expected to appear, matched to the antenna resonance. Alternative to the hot electron generation process, one could imagine immobilizing a single quantum dot or molecule in the gap [12–14]. Due to the directionality of this antenna we would also attain control over the emission direction of these photons. See Fig. 9.2 for a sketch of the concept.
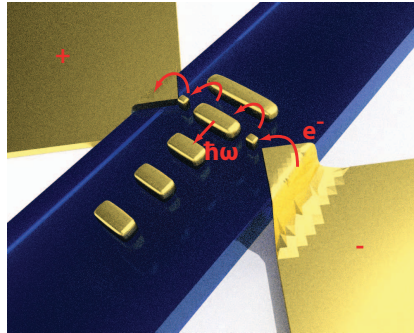
Figure 9.2: Artist impression of an on-chip integrated Coulomb-blockade photon source based on a Yagi-Uda antenna.

Some of the main problems that should be resolved to assess the feasibility of this approach are firstly to assess if multi-photon emission probabilities are indeed low, and secondly if deterioration of devices due to electrical driving can be avoided. To avoid that multiple photons are produced one can enhance the radiative LDOS by the use of a proper designed antenna for wavelengths close in energy to the energy of the hot electrons. To avoid deterioration due to electrical driving one could imagine

working in a vacuum environment or by embedding the system in a properly chosen high-k dielectric medium. This technology would need to compete with single photon production of 10^3 photons/second/nm achieved with NV center based commercially available single photon sources e.g. [http://qcvictoria.com/] or 10^6 photons/s/nm achieved with spontaneous parametric down conversion [15].

9.4 Design of antennas with asymmetrical scattering capabilities

Finally we review possible applications of one of the main results of this thesis, namely the asymmetries in terms of the differential scattering cross section and its polarization dependence that arise due to magnetic, magnetoelectric, and quadrupolar effects. Usually plasmonic antennas like for instance rod antennas, due to their small size, are seen as objects that scatter light equally whether they are excited in the forward or backward direction along a certain orientation. That is, these antennas usually scatter light symmetrically under a spatial inversion in the direction of excitation. This symmetrical scattering can be understood from the point of view that scatterers considerably smaller than the wavelength can be well described as electrical dipolar scatterers. Therefore, the only driving input for the scattering process is the electric field (**E**). This input does not change (up to a phase factor) upon an inversion between forward or backward excitation direction. In contrast, in this thesis we found examples of antennas for which an asymmetrical forward-backward scattering was present due to the appearance of higher order modes like magnetic dipolar and electric quadrupolar modes. For these modes, as explained in chapter 7, the excitation is also given by the magnetic field (**H**) and the symmetric electric field gradient ($\Diamond$**E**). With **E**, **H** and $\Diamond$**E** as driving for the scattering process it is easy to see that the scattering can not be symmetric under inversion, since even for a plane wave excitation **E**, **H** and $\Diamond$**E** must change relative phase and sign under such an inversion. This can be condensed in the following statement: if the superpolarizability tensor contains cross coupled terms there will be an asymmetry in the forward-backward excitation scattering, which also implies that for every axis with a broken geometrical symmetry a cross coupled term will be obtained.

Applications of these asymmetries fall apart in two classes: control over polarization degrees of freedom, and control over the spatial distribution of scattered light. As regards the first, in Chapter 6, we discussed the fact that magneto-electric scatterers, such as split rings, show a strongly handed response to incident light. In other words, the coherence relation between the electric and magnetic dipole moment that can be simultaneously induced in a split ring ensure a large difference in extinction depending on handedness of the incident light, at least for particular incidence directions, and viceversa a strong handedness of scattered light for particular scattered wave vectors. Moreover, we demonstrated that this effect can be significantly boosted by placing scatterers in arrays, in such a way that the scattering patterns narrows around the wave vectors for which reradiated light is strongly handed. An interesting possibility is to use

such antennas to create directional emitters that radiate handed light. More precisely such antenna proposed in Chapter 6 is shown to radiate the emission of a source close by the antenna in the forward direction with right handed elliptical polarization, while it will radiate in the backward direction left handed elliptically polarized light. This type of correlation between direction and spin angular momentum has been already investigated in e.g. the photon spin Hall effect introduced by Bernevig et al. [16] as well as in the work of le Feber et al. [17]. The coupling between photon angular momentum and photon pathway could be used as an implementation of flying q-bits. Also, this type of antenna might be used for an on-chip enantioselective discrimination of chiral molecules like the ones found in pharmaceutical complexes [18, 19].

Regarding the second class of antennas, with which we can control the spatial distribution of scattered light, we return to the nano-pyramid antennas discussed in Chapter 7. These structures possess a strong asymmetric scattering created by the interference of the electric dipolar and the magnetic dipolar and electric quadrupolar modes sustained in these structures. Specifically when these structures are illuminated, with light at a wavelength centered around 660 nm, from the top with linearly polarized light, high field intensity zones are created on the bottom of the antenna, while when illuminated from the bottom such local hot spots are created on the top of the antenna. We propose together with Said R.K Rodriguez that this vertical asymmetry in scattering and in field confinement close to the antenna is based on the interference between the dipolar and quadrupolar modes which creates this special scattering asymmetry. By understanding the basic elements of this type of scattering one could optimize in a single or in a multi-element structure this interference effect. Having a strongly asymmetric scattering object could be used for lighting applications using LEDs. In particular, for white light generation there is a large demand for efficient conversion of blue LED light into other colors by a phosphorescent layer. Asymmetric scattering structures could aid both the absorption and the emission process. Moreover, for particular lighting applications in, e.g., automotive or projection devices, directional emission could be useful. Also, near-field asymmetric scattering might be used for enhancing solar cell absorption. This enhancement is possible since near field excitation could be concentrated only where required, for instance at the active layer of the solar cells.

References

[1] P. Zijlstra, P. M. R. Paulo, and M. Orrit, *Optical detection of single non-absorbing molecules using the surface plasmon resonance of a gold nanorod*, Nat Nano **7**, 379 (2012).

[2] H. J. Kimble, *The quantum internet*, Nature **453**, 1023 (2008).

[3] T. Lund-Hansen, S. Stobbe, B. Julsgaard, H. Thyrrestrup, T. Sünner, M. Kamp, A. Forchel, and P. Lodahl, *Experimental realization of highly efficient broadband coupling of single quantum dots to a photonic crystal waveguide*, Phys. Rev. Lett. **101**, 113903 (2008).

[4] P. Lodahl, A. Floris van Driel, I. S. Nikolaev, A. Irman, K. Overgaag, D. Vanmaekelbergh, and W. L. Vos, *Controlling the dynamics of spontaneous emission from quantum dots by photonic crystals*, Nature **430**, 654 (2004).

[5] D. E. Chang, A. S. Sørensen, P. R. Hemmer, and M. D. Lukin, *Quantum optics with surface plasmons*, Phys. Rev. Lett. **97**, 053002 (2006).

[6] A. V. Akimov, A. Mukherjee, C. L. Yu, D. E. Chang, A. S. Zibrov, P. R. Hemmer, H. Park, and M. D. Lukin, *Generation of single optical plasmons in metallic nanowires coupled to quantum dots*, Nature **450**, 402 (2007).

[7] A. L. Falk, F. H. L. Koppens, C. L. Yu, K. Kang, N. de Leon Snapp, A. V. Akimov, M.-H. Jo, M. D. Lukin, and H. Park, *Near-field electrical detection of optical plasmons and single-plasmon sources*, Nat. Phys. **5**, 475 (2009).

[8] J. Simon, H. Tanji, J. K. Thompson, and V. Vuletić, *Interfacing collective atomic excitations and single photons*, Phys. Rev. Lett. **98**, 183601 (2007).

[9] A. D. Semenov, G. N. Gol'tsman, and R. Sobolewski, *Hot-electron effect in superconductors and its applications for radiation sensors*, Superconductor Science and Technology **15**, R1 (2002).

[10] M. W. Knight, H. Sobhani, P. Nordlander, and N. J. Halas, *Photodetection with active optical antennas*, Science **332**, 702 (2011).

[11] C. Clavero, *Plasmon-induced hot-electron generation at nanoparticle/metal-oxide interfaces for photovoltaic and photocatalytic devices*, Nat Photon **8**, 95 (2014).

[12] A. G. Curto, G. Volpe, T. H. Taminiau, M. P. Kreuzer, R. Quidant, and N. F. van Hulst, *Unidirectional emission of a quantum dot coupled to a nanoantenna*, Science **329**, 930 (2010).

[13] C. Toninelli, Y. Delley, T. Stöferle, A. Renn, S. Götzinger, and V. Sandoghdar, *A scanning microcavity for in situ control of single-molecule emission*, Applied Physics Letters **97**, (2010).

[14] F. T. Rabouw, M. Frimmer, A. Mohtashami, and A. F. Koenderink, *Nanoscale lithographic positioning of fluorescing quantum dot nanocrystals on planar samples*, Optical Materials **35**, 1342 (2013).

[15] E. Pomarico, B. Sanguinetti, T. Guerreiro, R. Thew, and H. Zbinden, *Mhz rate and efficient synchronous heralding of single photons at telecom wavelengths*, Opt. Express **20**, 23846 (2012).

[16] B. A. Bernevig, X. Yu, and S.-C. Zhang, *Maxwell equation for coupled spin-charge wave propagation*, Phys. Rev. Lett. **95**, 076602 (2005).

[17] B. le Feber, N. Rotenberg, and L. Kuipers, *A scalable interface between solid-state and flying qubits: observations of near-unity dipole helicity to photon pathway coupling*, arXiv **1406.7741v1** (2014).

[18] Y. Tang and A. E. Cohen, *Optical chirality and its interaction with matter*, Phys. Rev. Let **104**, 163901 (2010).

[19] Z. Fan and A. O. Govorov, *Plasmonic circular dichroism of chiral metal nanoparticle assemblies*, Nano Letters **10**, 2580 (2010).

A

Quadrupolar Fields and 12×12 α^S-Tensor

Here we show that given the choice of casting the rank 2 quadrupole tensor in a vector, and reducing redundancy due to the tensor symmetry, the $\diamond$ operator is completely determined. Starting from the symmetric traceless quadrupole tensor Q, the field emitted by a quadrupole in Einstein notation is

$$E_i(\mathbf{r}) = \frac{\omega^2 \mu\mu_0}{3!} Q_{jk} \nabla'_k \mathbf{G}_{ji}(\mathbf{r}, \mathbf{r}'), \tag{A.1}$$

with ω the optical frequency, $\mu\mu_0$ the permeability of the surrounding medium and G the 3×3 electric Green dyadic. That the tensor Q_{ij} is symmetric allows a regrouping of terms (where we abbreviate $\partial_{x'}\mathbf{G}_{ij}(\mathbf{r}, \mathbf{r}')$ as $G_{ijx'}$)

$$\mathbf{E} = \frac{\omega^2 \mu\mu_0}{3!} \cdot$$
$$\begin{pmatrix} Q_{12}(G_{11y'}+G_{12x'})+Q_{13}(G_{11z'}+G_{13x'})+Q_{23}(G_{12z'}+G_{13y'})+Q_{11}G_{11x'}+Q_{22}G_{12y}+Q_{33}G_{13z'} \\ Q_{12}(G_{21y'}+G_{22x'})+Q_{13}(G_{21z'}+G_{23x'})+Q_{23}(G_{22z'}+G_{23y'})+Q_{11}G_{21x'}+Q_{22}G_{22y}+Q_{33}G_{23z'} \\ Q_{12}(G_{31y'}+G_{32x'})+Q_{13}(G_{31z'}+G_{33x'})+Q_{23}(G_{32z'}+G_{33y'})+Q_{11}G_{31x'}+Q_{22}G_{32y}+Q_{33}G_{33z'} \end{pmatrix} \tag{A.2}$$

which can be identified as

$$\mathbf{E} = \frac{\omega^2 \mu\mu_0}{3!} (\diamond' \overline{\mathbf{G}}^\top(\mathbf{r}, \mathbf{r}'))^\top \cdot \mathbf{Q}. \tag{A.3}$$

Thereby defining $\mathbf{Q}$ as a 6-vector as in Eq. 7.5 fixes the definition of $\diamond$. Mutatis mutandi the same reasoning holds if in Eq. (A.2) one eliminates Q_{zz} on basis of the traceless nature of the tensor Q, in which case inserting the definition of $\hat{\mathbf{Q}}$ fixes $\hat{\diamond}$.

B

Dolmen α^S-Tensor Elements

Here we report on Fig.B.1,B.2 and B.3 the amplitude and phase of the superpolarizability tensor elements versus wavelength of a silver Dolmen structure. These figures are shown to complement our report on Sec. 7.3 about the elements of $|\alpha^S|$, which were shown for one wavelength and on a logarithmic color scale.
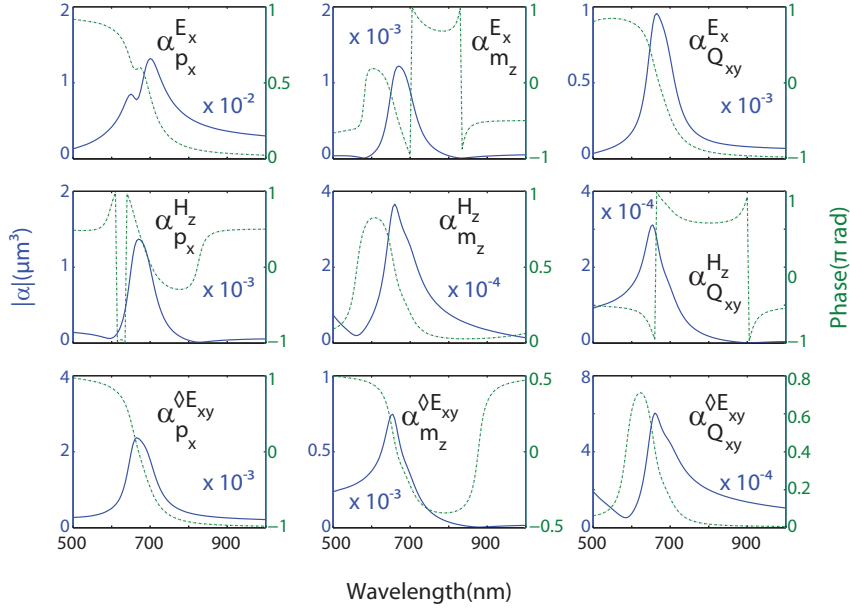
Figure B.1: Elements related to p_x, m_z and $Q_{x,y}$ of the α^S-tensor of a silver dolmen structure. These elements span the subspace relevant for PIT in the dolmen system. Solid curves show amplitude while dashed curves show phase.
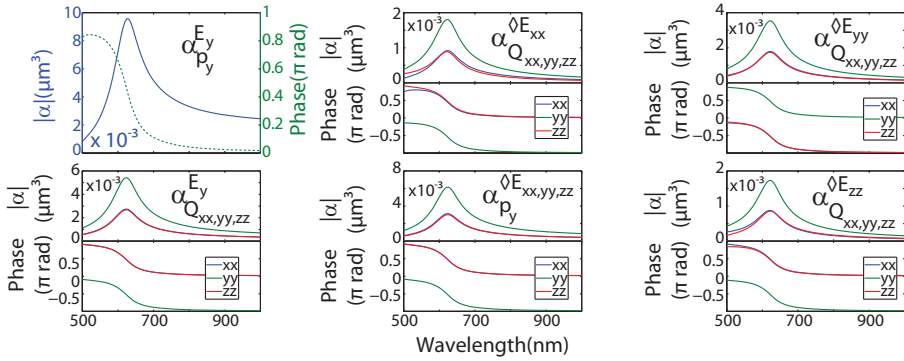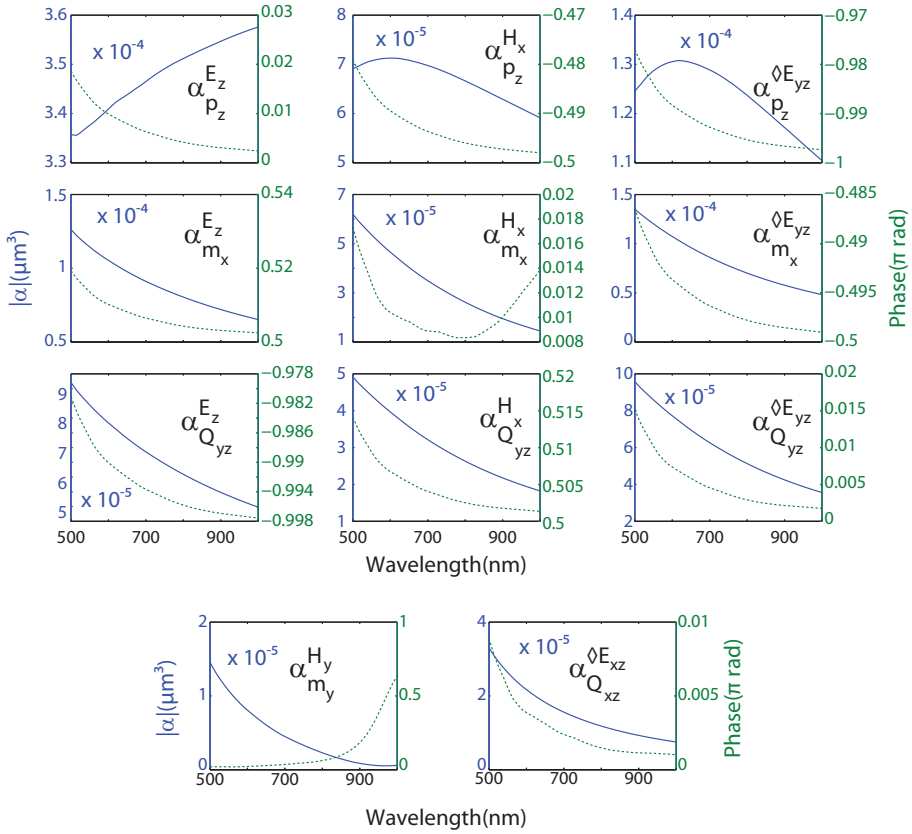

Figure B.2: Elements related to p_y and $Q_{xx,yy,zz}$ of the α^S-tensor of a silver dolmen structure. These elements correspond to excitation of the symmetric dimer resonant mode, which has a strong electric dipole character, as well as carrying a linear y-oriented quadrupole moment.

Figure B.3: Summary of weaker elements of the α^S-tensor of the silver dolmen structure, generally corresponding to out-of-plane charge separation. Solid curves show amplitude while dashed curves show phase.

C

Gold Disk α^S-Tensor Elements

To complement our report in Sec. 8.3 of elements of $|\alpha^S|$ at one wavelength and as a logarithmic color scale for the Au nanodisk on a Si substrate, here we report the superpolarizability tensor element amplitude and phase versus wavelength in Fig.C.1.

Figure C.1: Elements of the α^S-tensor of a gold cylinder with 180 nm diameter and 80 nm height.

Summary

Currently our society faces two large challenges: a challenge in information technology where a growing number of people request access to increasingly large internet bandwidths, and a challenge in energy, i.e., to sustainably provide for the world energy consumption without dependence on fossil fuels. For both these problems possible solutions are sought in the efficient manipulation and control of light. For information technology, light has the large advantage that signals can be multiplexed by encoding information in different wavelengths, allowing a single fiber to carry up to Terabytes/s of information. As regards energy, if we would be able to harvest just 0.02% of the solar energy incident on the entire earth yearly, this would completely fulfill our energy demands. Both challenges require exquisite control over how light propagates, and over how light interacts with matter through emission, absorption and scattering. This control has been vastly improved in the last decade by recently developed new design ideas and fabrication possibilities for nanophotonic structures. In order to contribute to science in this specific direction, in this thesis, we explore ways in which we can more intuitively understand and design complex nanophotonic structures that are composed of metal scatterers embedded in dielectric structures. Metal scatterers are currently studied very intensively in the field of "plasmonics". Especially structures made of noble metals can act as very strong "antennas" that strongly scatter and confine light. In this work we specifically target the question how antennas can be integrated with dielectric structures such as waveguides which can losslessly carry information as light, which, could be the next step of the revolution in information technology started by optical fibers.

Chapter 2 reports on scattering experiments on single rod plasmonic nano antennas fabricated on top of a single mode Si_3N_4 ridge waveguide. This study was carried out to assess how strongly light propagating in guided modes interact with plasmon antennas, with the ultimate goal to provide an on-chip plasmon building block for interconversion between guided modes and strongly localized fields that could, for instance, interact with active materials. We found that when placed on a single mode dielectric waveguide, the response of plasmonic rod antennas can be simplified to that of electric dipolar scatterers placed on a multilayer system. When driven on resonance these small antennas scatter out of the waveguide up to 20% of the light from the guided mode, showing the strong interaction of plasmonic antennas with the waveguide mode. To gain control over the scattering process we use this building block as a base for more complex antennas. Therefore, we continue this research in chapter 3 by studying the system of a multi-element phased array plasmonic antenna plus dielectric waveguide.

In this chapter we characterize the scattering processes created by a phased array antenna positioned on a waveguide. We find that phased array antennas on a waveguide couple very strongly to the guided mode. We also find that interference, occurring due to the scattering from the different elements of the antenna, endow the system with directional scattering both out of the waveguide mode and into the waveguide mode. To complement the study performed in chapter 3, regarding the incoupling of light from point sources, we continue with chapter 4 by studying phased array antennas under localized excitation. For this purpose we used a cathodoluminescence measurement set-up to generate nanometric position controlled point sources on Yagi-Uda antennas. By using point dipole theory and a statistical analysis we explain the features appearing in the acquired spatial excitability maps. We conclude that Yagi-Uda antennas are highly robust when it comes to providing directivity, but exquisitely sensitive to disorder as regards to the enhancement in radiative power provided by the antenna.

In chapter 5 we change focus and work on developing analytical theory tools that allow us to understand and design optical nano antennas. In this chapter we present a numerical tool with which the polarizability tensor of any optical antenna with an arbitrary geometry can be retrieved. This tool is based on either an expansion of the scattered fields in vector spherical harmonics (VSH) or on the integration of the effective surface currents driven on the scatterers. We compare both routines and we find that the VSH tool is more accurate than the effective currents approach, although the latter allows for the retrieval of the polarizability tensor for scatterers on surfaces and in close proximity to other scatterers. In chapter 6 we use the retrieval tool to explain the behaviour of one of the most iconic optical antennas, the split ring resonator. We find that the split ring has a strong magneto optical coupling that amounts to 27% of the electric polarizability. We proceed to use the multipolar expansion of this magneto electric antenna to design a novel split ring based multi-element antenna with very interesting characteristics as a directive radiation source of elliptically polarized light from a localized point source. The ellipticity of the radiated light can be increased by using magnetoelectric scatterers with a stronger cross coupling that the obtained with the split ring.

In chapter 7 we expand the point dipole model to include electric quadrupolar moments. We use this extended theory to analyze the behavior of two types of antennas. The first of these is the socalled "dolmen" antenna that was reported in literature to support a very strongly quadrupolar mode. In particular, we quantify the claim made in earlier reports that narrow features in the dolmen extinction spectrum known as "Fano interference" or "plasmon-induced transparency" (PIT) are attributable to a quadrupolar response. We find that in fact the PIT is not only due to the quadrupolar mode but that a commonly disregarded magnetic dipole term is also present and contributes as much as the quadrupolar one in the interference process. The second of these antennas concerns nanopyramids made out of aluminium. Through optimization of their simultaneous electric dipole, magnetic dipole, and electric quadrupole response these nanopyramids are shown to be suitable for vertical asymmetric field confinement that could be used for enhancing LED illumination and solar cells. Finally, in chapter 8 we show how to use the extended point quadrupole-dipole theory in the presence of a substrate. We

explain measurements of nano cylinders with strong quadrupolar moments, measured in a cathodoluminescence setup, which are capable of strongly directing light by the interference of its different multipolar moments. These "nano lighthouses" have the characteristic that they are capable of strongly directing scattered light although the antenna is composed of one single element.

Samenvatting

Momenteel staat onze samenleving voor twee grote uitdagingen: een uitdaging in informatietechnologie , waar een toenemende groep gebruikers toegang wil hebben tot steeds meer bandbreedte, en een uitdaging in onze energie voorziening, waar het doel is om duurzaam te voorzien in de wereldwijde energie consumptie zonder afhankelijk te zijn van fossiele brandstoffen. Voor beide problemen worden mogelijke oplossingen gezocht in de efficiente manipulatie en controle over licht. Voor informatietechnologie heeft licht het grote voordeel dat signalen gemultiplexed kunnen worden door het coderen van informatie in verschillende golflengtes, waardoor er door 1 enkele fiber Terrabytes aan data per seconde gestuurd kan worden. Wat betreft het energie probleem is het zo dat als we in staat zijn om 0.02% van alle zonne-energie die jaarlijks op de aarde valt op te slaan we volledig voldoen aan onze energie behoefte. Beide uitdagingen vereisen nauwkeurige controle over hoe licht interageert met materie door middel van emissie, absorptie en verstrooiing. In de afgelopen tien jaar is deze controle sterk verbeterd door recent ontwikkelde ontwerp ideeen en fabricage mogelijkheden voor nanofotonische structuren. Om in deze richting bij te dragen aan de wetenschap exploreren we manieren waarop we meer intuitief complexe nanofotonische structuren samengesteld uit metalen verstrooiers in dielectrische media kunnen begrijpen en ontwerpen. Metalen verstrooiers worden momenteel intensief bestudeerd op het gebied van "Plasmonics". In het bijzonder kunnen structuren gemaakt van nobele metalen goede 'antennes' zijn die het licht sterk verstrooien en licht kunnen opsluiten. In dit proefschrift richten we ons specifiek op de vraag hoe we zulke antennes kunnen integreren met dielektrische structuren zoals golfgeleiders die zonder verliezen licht kunnen transporteren.

We beginnen dit proefschrift met hoofdstuk 2 waar we verstrooiingsexperimenten beschrijven op enkele plasmonische nano-antennas die gefabriceerd zijn op golfgeleiders die bestaan uit een siliciumnitride strip op een kwartssubstraat, en die slechts een enkele optische mode geleiden. Het doel van dit experiment is om uit te zoeken hoe sterk de interactie is tussen het licht dat zich voortplant in de golfgeleider en de plasmon antennes met als uiteindelijke doel het verkrijgen van een plasmonische bouwsteen om reciproke conversie mogelijk te maken tussen golfgeleider modes en de sterk gelokaliseerde velden die een interactie kunnen hebben met bijvoorbeeld actieve materialen. Het blijkt dat we de respons van de plasmonische nanostaafjes op de enkele mode golfgeleider kunnen vereenvoudigen tot die van elektrische dipool verstrooiers op een systeem van multilagen. Wanneer de nano-antennes geexciteerd worden op hun resonantie dan verstrooien ze tot 20% van het licht van de golfgeleider mode,

wat demonstreert dat er een sterke interactie is tussen de plasmonische antenne en de golfgeleider mode. Om controle te krijgen over het verstrooiingsproces gebruiken we deze bouwsteen als basis voor meer complexe antennes. In hoofdstuk 3 bouwen we verder op de resultaten uit hoofdstuk 2, en bestuderen zogenaamde "gefaseerde antenne arrays", bestaande uit een aantal plasmonische nanostaafjes op nanoschaal afstand van elkaar gegroepeerd op een golfgeleider. In dit hoofdstuk karakteriseren we het verstrooiingsproces dat ontstaat door de gefaseerde array antennes op een waveguide. Het blijkt dat, net als de enkele antennes ook deze gefaseerde array antennes sterk koppelen aan de golfgeleider mode. Daarnaast zien we dat de interferentie door de verstrooiing van verschillende elementen van de antenne ervoor zorgt dat het systeem directioneel verstrooit. Dit geldt voor zowel verstrooing uit de waveguide mode als verstrooiing in de waveguide mode. De studie van hoofdstuk 3 inzake het inkoppelen van licht van puntbronnen complementeren we met experimenten beschreven in hoofdstuk 4, waar we gefaseerde array antennes bestuderen met lokale excitatie. Hiervoor hebben we een kathodeluminescentie meetopstelling gebruikt waarmee we nanometrisch precies gepositioneerde puntbronnen kunnen genereren op de Yagi-Uda antennes. Door puntdipool theorie te gebruiken en een statistische analyse toe te passen kunnen we kenmerken verklaren die te zien zijn in de verkregen positieafhankelijke exciteerbaarheidskaarten. We concluderen hieruit dat Yagi-Uda antennes zeer robuust zijn wat betreft van directionele verstrooiing, maar uitzonderlijk gevoelig zijn voor wanorde wat betreft de vergroting van stralingsvermogen van de antenne.

In hoofdstuk 5 verplaats het aandachtsgebied van het proefschrift zich naar het ontwikkelen van een analytische theorie die ons in staat stelt optische nano-antennes te begrijpen en te ontwerpen. In dit hoofdstuk presenteren we een numeriek model waarmee we de polariseerbaarheidstensor van optische antennes met een willekeurige geometrie kunnen verkrijgen. We hebben twee manieren om de polarizeerbaarheidstensor te vinden. Ofwel de verstrooide velden worden weergegeven als een expansie in vector bolfuncties (VSH), ofwel er worden effectieve oppervlakte stromen geïntegreerd die aangedreven worden op het oppervlak van de verstrooiers. We vergelijken beide routines en zien dat de VSH methode nauwkeuriger is dan de effectieve stroom routine. In hoofdstuk 6 passen we deze methode om de polariseerbaarheidstensor te verkrijgen toe op één van de meest iconische optische antennes: de 'Split Ring Resonator' (SRR). We laten zien dat de SRR een sterke magneto-optische koppeling heeft die 27% is van de elektrische polariseerbaarheid. We gebruiken de multipool expansie van deze magneto-electrische antenne om een nieuwe multi-element antenne te ontwerpen gebaseerd op de SRR, die interessante kenmerken heeft. Zo blijkt het een directionele stralingsbron van elliptisch gepolariseerd licht te zijn. De ellipticiteit van het uitgestraalde licht kan vergroot worden door magnetoelectrische verstrooiers te gebruiken met nog sterkere magneto-optische koppeling dan de SRR.

In hoofdstuk 7 breiden we het puntdipool model uit door ook electrische quadrupool momenten mee te nemen. We gebruiken deze uitgebreide theorie om het gedrag van twee soorten antennes te analyseren. De eerste is de zogenaamde 'dolmen' antenna waarvan al is aangetoond dat deze een sterke quadrupool mode heeft. We kwantificeren

de bewering gemaakt in eerdere artikelen dat spectraal smalle kenmerken die zichtbaar zijn in het extinctie spectrum, bekend als zogenaamde 'Fano interferentie' of 'plasmon-geinduceerde transparantie' (PIT) toe te schrijven zijn aan een quadrupolaire respons. We laten zien dat PIT niet alleen aan de quadrupolaire mode is toe te schrijven, maar dat ook de magnetische dipolaire mode bijdraagt - een mode die vaak buiten beschouwing wordt gelaten. Deze mode draagt net zo veel bij aan het interferentie proces als de quadrupool mode. Het tweede type antenne dat we analyseren is de aluminium nanopyramide. Door gelijktijdig te optimaliseren voor de elektrische en magnetische dipool en de elektrische quadrupool laten we zien dat deze nanopyramides geschikt zijn om het veld asymmetrisch op te sluiten.. Dit heeft mogelijke toepassingen in het verbeteren van LED verlichting en voor zonnecellen. Tot slot laten we in hoofdstuk 8 zien hoe we de uitgebreide puntquadrupool-dipool theorie kunnen gebruiken wanneer er ook een substraat aanwezig is. Grote, platte nanocylinders van goud blijken sterke quadrupolaire momenten te hebben als ze op een silicium substraat liggen. Door de interferentie van de verschillende multipolaire elementen hebben deze 'nano-vuurtorens' het bijzondere kenmerk dat ze verstrooid licht sterk één kant op sturen hoewel de antenne zelf maar uit één element bestaat. Wij passen onze theorie toe op kathodeluminescentiemetingen gedaan aan deze nanocylinders en verklaren de metingen.

List of publications

This thesis is based on the following publications:

- *Plasmonic Antennas Hybridized with Dielectric Waveguides*, Felipe Bernal Arango, Andrej Kwadrin, A. Femius Koenderink, ACS nano **6**(11), 10156-10167 (2012). **(Chapter 2)** and **(Chapter 3)**

- *Localized Excitation of Antennas on Waveguides*, Felipe Bernal Arango, Rutger Thijssen, Benjamin Brenny, Toon Coenen, Albert Polman, and A. Femius Koenderink, in preparation. **(Chapter 4)**

- *Polarizability Tensor Retrieval for Magnetic and Plasmonic Antenna Design*, Felipe Bernal Arango, A. Femius Koenderink, New J. Phys. **15** 073023 (2013). **(Chapter 5)** and **(Chapter 6)**

- *Ubiquity of Optical Activity in Planar Metamaterial Scatterers*, Ivana Seršic, Marie Anne van de Haar, Felipe Bernal Arango and A. Femius Koenderink, Phys. Rev. Lett. **108**, 223903 (2012). **(Chapter 6)**

- *Underpinning Hybridization Intuition for Complex Nanoantennas by Magneto-electric Quadrupolar Polarizability Retrieval*, Felipe Bernal Arango, Toon Coenen, A. Femius Koenderink, ACS Photonics **1** 444-453 (2014). **(Chapter 7)** and **(Chapter 8)**

- *Breaking the symmetry of forward-backward light emission with localized and collective resonances in magnetoelectric nanopyramid arrays*, Said R.K Rodriguez, Felipe Bernal Arango, Tom P. Steinbusch, Marc A. Verschuuren, A.Femius Koenderink and Jaime Gómez Rivas submitted PRL **(Chapter 7)**

- *Directional Emission from a Single Plasmonic Scatterer*, Toon Coenen, Felipe Bernal Arango, A. Femius Koenderink, Albert Polman, Nature Comm. 10.1038/ncomms4250 (2014) **(Chapter 8)**

Other publications by the author:

- *Optical Forces and Trapping Potentials of a Dual-Waveguide Trap Based on Multimode Solid-Core Waveguides*, Matheus M. van Leest, Felipe Bernal Arango, Jaap Caro, J. Europ. Opt. Soc. Rap. Public. **6** 11022 (2011)

- *Optofluidic tuning of photonic crystal band edge lasers*, Felipe Bernal Arango, Mads Brokner Christiansen, Morten Gersborg-Hansen, and Anders Kristensen, Appl. Phys. Lett. **91**, 223503 (2007)

Patents:

- *Optical Trap, Chip, Sensor System and Method for Manufacturing an Optical Trap*, Matheus Maria Van Leest, Felipe Bernal Arango, Jaap Caro, WO Patent 2,012,033,409

Acknowledgements

I would like to keep this register of gratitude short, not because I do not have many people to thank but precisely because of the contrary. In fact, to be fair to all, I would need to write an account documenting the innumerable times that I have been helped during and before this period of my life. All these instances have contributed to who I am and to what I have done to a degree that we can simply not comprehend. Due to our interconnectedness, for all you have done for me and for this work, thank you!

Very briefly, I would like to thank Wikipedia, a representation of you, me and all human knowledge, without which this thesis would have taken much longer to produce. Also, I would like to explicitly thank a group of people, not because of their direct contributions, but rather because of how much they have inspired me:

Thanks Femius for showing me how the motivation of performing a good work should be faithfully kept until the end. Your continuous joyous effort, your strength and delight in doing things properly has kept me going even in moments of doubt and fatigue. I have learned a lot from you.

Thanks Anne for inspiring me with your kindness and compassion, which has taken you as far as the middle of the desert to empower girls with your knowledge.

Thanks Alejo for your joy, compassion and hard work that took you the remote jungle where nobody wanted to go, to show that beauty can be found and help can be provided when a proper motivation is present.

Thanks Juan for showing me how patience, concentration and hard work may one day illuminate (as in LEDs) the poorest places in the world.

Thanks Ma for showing me how loving kindness and affection can motivate you to listen and heal the most troubled of the people anywhere and anytime, and for introducing me to this other side of life.

Thanks Papo for your tireless work, your unforgettable lessons and your immense wisdom which brought us here and allowed us to rejoice with your piece of the Nobel Peace Prize.

Finally, and as I said before, thank you...

OPTICAL ANTENNAS ON SUBSTRATES AND WAVEGUIDES

Felipe Bernal Arango

2014